QUANTUM PHASE TRANSITIONS AND QUANTUM TRANSPORT IN LOW-DIMENSIONAL TOPOLOGICAL SYSTEMS

by
BARIŞ PEKERTEN

Submitted to the Graduate School of Engineering and Natural Sciences
in partial fulfillment of
the requirements for the degree of
Doctor of Philosophy

Sabancı University
June 2017

QUANTUM PHASE TRANSITIONS AND QUANTUM TRANSPORT IN LOW-DIMENSIONAL TOPOLOGICAL SYSTEMS

APPROVED BY

Assoc. Prof. İnanç Adagideli .....
(Thesis Supervisor)

Assoc. Prof. Emrah Kalemci .....

Assoc. Prof. İbrahim Burç Mısırlıoğlu .....

Assoc. Prof. Özgür Esat Müstecaplıoğlu .....

Assoc. Prof. Levent Subaşı .....

DATE OF APPROVAL .....

ABSTRACT

QUANTUM PHASE TRANSITIONS AND QUANTUM TRANSPORT IN LOW-DIMENSIONAL TOPOLOGICAL SYSTEMS

Barış Pekerten

Ph.D. Thesis, June 2017

Thesis Supervisor: Assoc. Prof. İnanç Adagideli

Keywords: Mesoscopic and nanoscale systems, topological insulators and superconductors, random matrices, spintronics, quantum thermodynamics

In this thesis, we focus on quantum phase transitions that change the topological index of topological insulators and superconductors, which are states of matter featuring topologically protected edge states and insulating bulk, and on transport of charge and spin in topological insulator nanostructures. We consider topological phases in disordered quasi-1D topological superconductors. The Majorana edge states on topologically nontrivial nanowires were previously found to be protected from disorder as long as the localization length is larger than the coherence length, after which the wire transitions to a trivial state. We find that changing disorder can push the system back into a topological state in multichanneled nanowires, creating previously unreported fragmentation of the topological phase diagram. We next discuss arbitrarily-shaped and/or disordered topological superconductors and their ground state fermion parity. As external parameters are varied, even and odd parity ground states cross, causing quantum phase transitions. We find that the statistics of parity-crossings are universal and described by normal-state properties and determine the shape dependence of the parity crossings. Finally, we consider edge state quantum transport in quantum spin Hall insulators in the presence of nuclear spins. We find that a properly initialized nuclear spin bath can be used as a non-energetic resource to induce charge current in the device, providing power an external load using heat from electrical reservoirs. Resetting the spin-resource requires dissipation of heat in agreement with the Landauer's principle. Our calculations show that the equivalent energy/power density stored in the device exceeds existing supercapacitors.

ÖZET

DÜŞÜK BOYUTLU TOPOLOJİK SİSTEMLERDE KUANTUM FAZ GEÇİŞLERİ VE KUANTUM TAŞINIM

Barış Pekerten

Doktora Tezi, Haziran 2017

Tez Danışmanı: Doç. Dr. İnanç Adagideli

Anahtar kelimeler: Meso ve nanoölçekli sistemler, topolojik yalıtkan ve üstüniletkenler, rastlantısal matrisler, spintronik, kuantum termodinamiği

Bu tezde, maddenin topolojik olarak korunumlu kenar durumları ve yalıtkan yığın içeren bir hali olan topolojik yalıtkan ve üstüniletkenlerin topolojik indisini değiştiren kuantum faz geçişlerine ve topolojik yalıtkan nanoyapılarda yük ve spin taşınımına odaklanıyoruz. Öncelikle düzensiz, bir boyutlumsu topolojik üstüniletkenlerde topolojik evreleri ele aldık. Daha önceden topolojik açıdan sıradışı evreli bir nanokablodaki Majorana durumlarının yerelleşme mesafesinin eşevrelilik mesafesini aştığı sürece düzensizliğe karşı korunumlu olduğu bulunmuştu; bu düzensizlik seviyesinden sonra kablo, sıradan evreye geçer. Biz ise bundan daha da fazla düzensizliğin çok kanallı nanokabloları topolojik evreye geri zorladığını ve topolojik evre çizgesini daha önce gösterilmemiş bir şekilde parçaladığını gösterdik. Devamında gelişigüzel şekilli ve/veya düzensiz topolojik üstüniletkenleri ve taban hal fermiyon eşliğini tartıştık. Harici değişkenler değiştirildikçe tek ve çift pariteli taban durumları kesişir ve kuantum evre geçişine sebep olur. Biz bu parite kesişim istatistiğinin evrensel oduğunu ve bu istatistiğin normal durum özellikleriyle belirlendiğini gösterdik. Ayrıca parite kesişimlerinin şekil bağımlılığını da ifade ettik. Son olarak çekirdek spinleri varlığında kuantum spin Hall yalıtkanının kenar durumunun taşınım özelliklerini ele aldık. Uygun şekilde hazırlanan bir çekirdek spin banyosunun enerjisiz kaynak olarak kullanılıp sistemde bir yük akımı tetiklemek için kullanılabileceğini ve bu akımın elektrik rezervuarlarının ısısını kullanıp harici bir dirençten güç açığa çıkarabileceğini gösterdik. Spin kaynağını sıfırlamanın Landauer prensipine uygun olarak ısı yayılımı gerektirdiğini gösterdik. Hesaplarımız, sistemde depolanan eşdeğer enerji/güç yoğunluğunun halihazırdaki süperkapasitörlerin yoğunluğunu aştığını göstermektedir.

ACKNOWLEDGEMENTS

The author of this thesis would like to declare his deep love for and indebtedness to his family, who have been supportive of him throughout thick and thin. The process of obtaining this Ph.D. was no different: There was the thick, and there was the thin; and there his family was, as always.

The author would also like to convey his heartfelt gratitude to his supervisor, Dr. İnanç Adagideli, for the many years he patiently taught and guided the author. The author would also like to communicate his thanks to his co-authors for an excellent research environment.

The author would like to express gratitude to The Science Academy (Bilim Akademisi) Turkey and to Feza Gürsey Center for Physics and Mathematics for the use of their facilities. The author also gratefully acknowledges financial support from the Erdal İnönü chair, from Scientific and Research Council of Turkey (TUBITAK) through their Scientist Support Program (BİDEB) scholarships, from Lockheed Martin Corporation Research Grant and from COST Action MP1209.

Contents

List of Figures and Tables

Chapter 1

INTRODUCTION

In this thesis, we explore the effects of disorder and scattering in low dimensional topological materials. In particular, we focus on the interplay of the topological properties and the transport properties of one or two dimensional topological insulators and superconductors. [1–3]. The main results of this thesis is reported in Chapters 3, 4 and 5.

This thesis is organized as follows: We begin Chapter 2 by reviewing topological properties of the electronic structure of materials in general. We next survey the general properties of the topologically nontrivial systems relevant to this thesis, namely Majorana states, 1D and 2D topological superconductors and quantum spin Hall systems. We also provide a brief introduction to the classification scheme of topological materials, i.e. "the tenfold way". We conclude our survey by reviewing the link between the transport properties and the topological properties of the topological materials relevant to the main results of this thesis.

In Chapter 3, we consider a quasi-1D disordered multichannel s-wave topological superconductor. Such systems are experimentally relevant in producing and detecting bound Majorana states. We show that for disordered nanowires, the closing and opening of a *transport* gap can also cause topological transitions, even in the presence of finite density of states [1]. We derive analytical expressions for the boundaries of such topological transitions within experimentally relevant parameter regimes. We show that new topological regions show up in the low magnetic field limit, requiring full description of all spin bands. We perform numerical simulations using a tight-binding (TB) approach and find very good agreement with our analytical formulae.

In Chapter 4, we study the statistics of the level-crossings between even and odd fermion parity levels at the Fermi energy as a function of external parameters (such as the magnetic field B or the chemical potential μ) in disordered or chaotic ballistic topological superconductor nanostructures [2]. Such crossings precursor the presence of a Majorana state in these systems in the long wire limit. We obtain formulae for the average parity crossing density. Next, we show that the fluctuations in these systems also follow uni-

versal statistics. We discuss the shape dependence of the statistics of the parity crossing spacing. We also find that the parity crossing points are described by the normal-state properties of the system.

In Chapter 5, we propose and discuss a method for heat harvesting in a device [3]. Our proposed engine uses the spin-polarized edge currents of a quantum spin Hall device as the working fluid and a coupled (nuclear) spin bath as the Maxwell's Demon (MD) memory. We show that an initial state of polarized nuclear spins (blank memory) drives an electrical current, thus acting as a memory resource of a MD that converts heat from the environment into electrical work. We also show how a charging-discharging cycle can be achieved and derive formulae for the work and power extraction in each phase of the cycle. We discuss the application of our proposed device as a battery or a supercapacitor.

Finally, in Chapter 6, we briefly outline our results.

Chapter 2

OVERVIEW

In this chapter, we give a background survey of the topological phase and topological insulators in one or two dimensions, as well as a brief outline of earlier results and arguments relevant to this thesis. We first review the concept of topological protection of the edge states in section 2.1. We then briefly go over several types of topological insulators and superconductors that are relevant to the rest of this thesis in section 2.2. We finally review the generalized classification of topological materials in arbitrary dimensions, also known as "the tenfold way", in section 2.3. For completeness, we briefly survey the integer quantum Hall effect in Appendix A.

2.1. Topological Properties of Matter

After the initial surge in the 1980's following the discovery of the quantum Hall effect (QHE) [4–7], the interest in the field of topological insulators has been renewed in the past decade. In the past, three Nobel prizes in physics were awarded for advances in the understanding of topological insulators and topological insulator materials [4, 6, 8–14]. Many reviews and textbooks on the topic of topological insulators have been published in the intervening years. (For a relatively recent selection as of the time of writing this thesis, see, for example, [15–26, 34].)

The concept of the topological phases of the electronic structure of matter relies on the Gauss-Bonnet theorem (or the Chern-Gauss-Bonnet theorem for generalization to $d > 3$ dimensions in the relevant parameter space) [7, 22, 23, 27]. The theorem relates the geometric properties and the topological properties of a surface. In particular, it states that the integral of the Gaussian curvature $\mathbf{\Omega}$ of a closed surface Σ integrated over the surface plus the geodesic curvature k_g of the boundary $\partial\Sigma$ integrated over the boundary is related to that surface's Euler characteristic:

$$2\pi\chi = \oint_{\Sigma} \mathbf{\Omega}.d\mathbf{S} + \oint_{\partial\Sigma} k_g.ds \tag{2.1}$$

The Euler characteristic χ of a surface is $\chi = V - E + F$, where v, E and F are the vertices, edges and faces of the surface. This definition is exact for polyhedra, but it may be taken as a limit for smooth surfaces of many polyhedra as the number of faces increase, yielding $\chi = 2$. It is also related to the *genus* g of a closed surface via $\chi = 2(1 - g)$. (Loosely defined, the genus is the number of handles of the surface; a sphere has $g = 0$ whereas a doughnut has $g = 1$). In the following paragraphs, we provide the definition of Gaussian curvature as it relates to our topic. We follow the convention of many reviews on topological insulators and simply ignore the boundary term in Eq. 2.1 as we usually do not deal with surfaces having boundaries.

The left hand side (LHS) of Eq. 2.1 is an integer (times 2π) and a topological invariant of a given surface, i.e. a smooth deformation (a homotopy) cannot change this characteristic value. The right hand side (RHS) is generally a complicated integral of the curl of a connection, or a flux through a surface, hence naïvely, one would not in general expect it to be an integer.

The topological nature of the materials that are the subject matter of this thesis stems from the Gauss-Bonnet theorem (Chern-Gauss-Bonnet theorem for $d > 3$ dimensions). The Gauss-Bonnet theorem is applied to a certain vector field (the details of which will be discussed below) derived from the Hamiltonian of the system and defined on the Brillouin zone of the materials in question. Then, this vector field is mapped to the Bloch sphere, as explained in subsection 2.1.3. It is the topology of this mapping to which the theorem is applied. We consider a bulk material for which the characteristic of the mapping is different than 2, which is the characteristic of the aforementioned map of the vacuum. We consider materials that are bulk insulators, and adiabatic changes to the parameters of the Hamiltonian that do not close the bulk insulating gap. (Superconductors, being quasiparticle insulators, are not exempt from this discussion.) Such changes in the material can cause small changes in the properties of the ground state such as its eigenenergy, but it cannot change the Euler characteristic of the map we considered above: The Euler characteristic is an integer, hence it cannot change by a small amount. This is the basis for *topological protection*.

We next discuss a simple, non-rigorous argument, called the *bulk-boundary correspondence*, on the existence of gapless edge states and their topological protection. The characteristic of the mapping we imagined (but have not yet detailed) of the vacuum is described by a sphere with a genus $\chi = 2$. We consider the material for which the characteristic of the mapping in the bulk is different than 2. In this hand-waving argument, we locally define a topological index. As we approach the boundary of the system, the Hamiltonian gradually changes. However, the characteristic cannot change in small

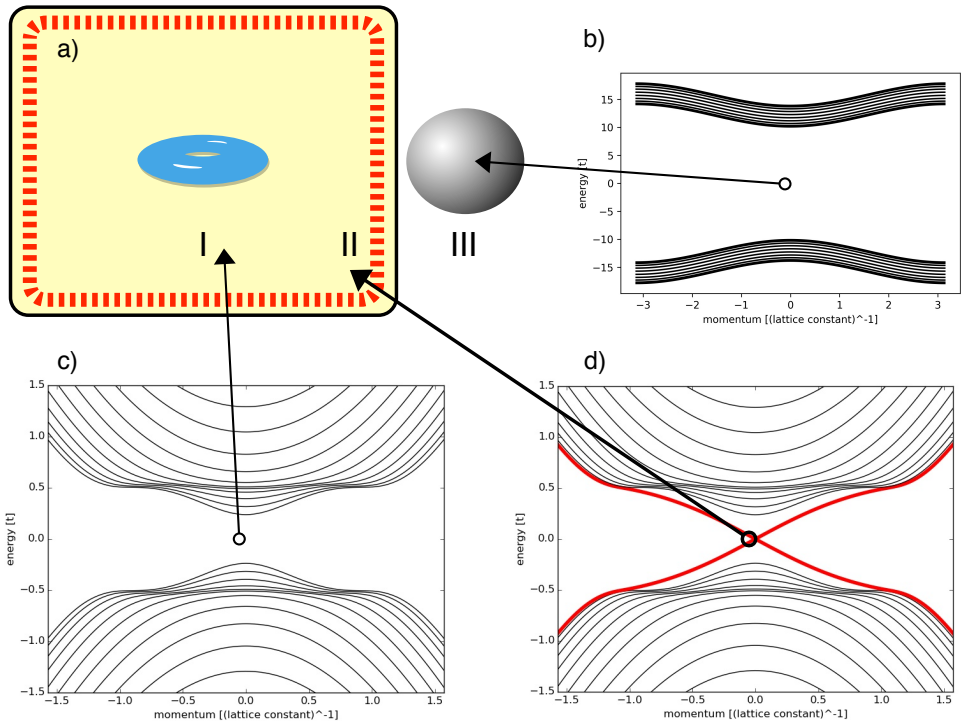

Figure 2.1: A schematic picture of a topological insulator in two dimensions. The yellow shaded structure in (a) is the topologically nontrivial material, with the torus representing the topology of the mapping between its Hamiltonian and an appropriate Bloch sphere over the Brillouin zone. The similar mapping from vacuum has a trivial topological shape of a sphere. The band structure of the discretized system in the tight binding model is given for the bulk in (c), for the edges in (d) and for the surroundings in (b). The bulk boundary correspondence forces the gap to be closed and a gapless edge state to be formed (the red band in (d)).

amounts from its bulk value to its vacuum value—it is an integer. So, a drastic change has to happen as the material transitions from the insulating bulk to the insulating vacuum. This drastic change takes the form of the closing of the bulk insulating gap and reopening it, resulting in a topologically protected *edge state*. The fundamental difference between the topological edge states and other edge states such as the *whispering gallery modes* (see, for example, References [28, 29]) is the presence of topological protection of such edge states (see Figure 2.1).

We now detail the concepts that were very briefly introduced in the previous paragraphs. We first describe in detail the RHS of Eq. 2.1. We introduce the concepts of *Berry phase* and *Berry connection* and define Gaussian curvature in terms of the Berry connection within the concept of topological band theory. We then introduce *Chern numbers*. We conclude by discussing concrete examples.

2.1.1. Berry Phase and Berry Curvature

In this subsection, we briefly review the Berry phase (or *the geometric phase*) [30]. In topological insulators, the Berry phase is the phase gained by an eigenfunction of the

Hamiltonian as some parameter of the Hamiltonian is adiabatically changed. If this change happens over time, the Berry phase is given by the total phase gain minus the dynamical phase, derived from the (adiabatic) time evolution of the system [7, 30]. (For a detailed introduction, we refer the reader to [15, 16, 22, 23, 34].)

Berry considers a Hamiltonian with n parameters that depend on time, represented by the n dimensional vector $\xi(t)$. He further considers an adiabatic change of said Hamiltonian through changing its parameters in time, obeying the Schrödinger equation:

$$H(\xi(t))\left|\psi(\xi(t),t)\right\rangle = i\hbar\partial_t\left|\psi(\xi(t),t)\right\rangle, \tag{2.2}$$

with eigenstates and eigenenergies at any instant given by $|n\xi(t)\rangle$ and $E_n(\xi(t))$. For simplicity, the spectrum is assumed discrete. Berry considers the overall phase change on a wavefunction, initially prepared in an eigenstate, as a function of time as the parameters ξ adiabatically change:

$$\left|\psi(\xi(t),t)\right\rangle = \exp\left(-\frac{i}{\hbar}\int_0^t dt' E_n(\xi(t'))\right) e^{i\gamma_n t}\left|n(\xi(t))\right\rangle. \tag{2.3}$$

Distinguishing the dynamical phase (the first factor in the above equation) from the *geometric phase* (which is now called the Berry phase) and substituting this into the Schrödinger equation, Berry obtains:

$$\partial_t\gamma_n(t) = i\left\langle n(\xi(t))\right|\nabla_\xi n(\xi(t))\rangle\cdot\partial_t\xi(t). \tag{2.4}$$

Berry then considers the path in the parameter space to be a closed curve C which the system traverses in time T, finding the *geometrical phase change* as

$$\begin{aligned}\gamma_n(C) &= i\oint_C \mathcal{A}(\xi)\cdot d\xi \\ &= i\oint_C \langle n(\xi)|\nabla_\xi n(\xi)\rangle\cdot d\xi.\end{aligned} \tag{2.5}$$

where

$$\mathcal{A}(\xi) = \langle n(\xi)|\nabla_\xi n(\xi)\rangle \tag{2.6}$$

is the *Berry connection*. With the assumption that $\langle\psi(\xi(t),t)|\psi(\xi(t),t)\rangle = 1$ for all ξ, we note that $\nabla_\xi\langle n(\xi)|n(\xi)\rangle = 0 \Rightarrow \langle n(\xi)|\nabla_\xi|n(\xi)\rangle^* = -\langle n(\xi)|\nabla_\xi|n(\xi)\rangle$, proving that $\mathcal{A}(\xi)$ is purely imaginary and hence the Berry phase is real. Hence, we write:

$$\gamma_C = -\mathrm{Im}\oint_C \langle n(\xi)|\nabla_\xi|n(\xi)\rangle. \tag{2.7}$$

Equations 2.5 and 2.7 suggest in a hand-waving manner that the Berry phase is a gauge-

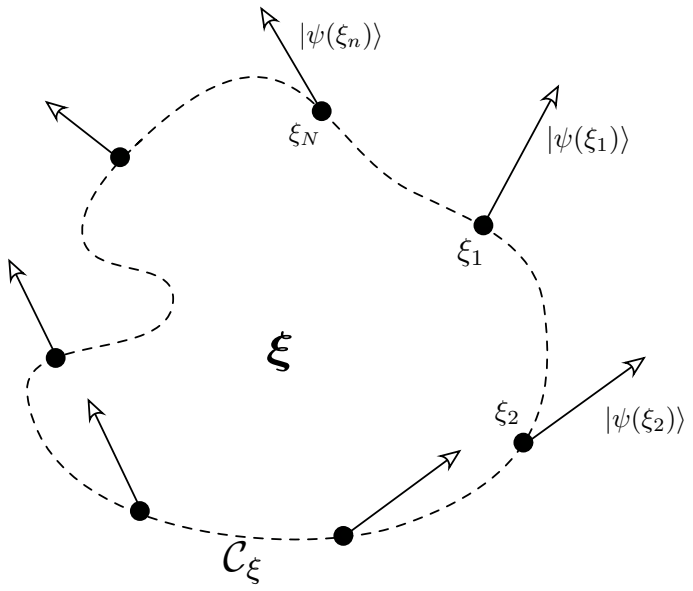

Figure 2.2: A schematic picture of a wavefunction $|\psi(\xi)\rangle$, represented by the arrows, that depends on some parameter vector $\boldsymbol{\xi}$. We are interested in what happens to the phase of $|\psi(\xi)\rangle$ as the parameter is changed on a closed curve $\mathcal{C}_\xi$.

independent quantity: Considering the integral as a Riemann sum of successive points ξ_i on the curve $\mathcal{C}$ and discretizing ∇_ξ as a difference operator, we would have terms like $\cdots + \langle n(\xi_i)|n(\xi_{i+1})\rangle + \langle n(\xi_{i+1})|n(\xi_{i+2})\rangle + \cdots$ in the aforementioned Riemann sum (see Figure 2.2). A local arbitrary gauge applied to the eigenket $|n(\xi_{i+1})\rangle$, for example, would drop out of this sum. In subsection 2.1.2, we give a manifestly gauge-independent formulation for the Berry phase, thus proving its gauge independence.

We note that a a gauge transformation on all $|\psi_0(\xi)\rangle \to e^{i\zeta(\xi)}|\psi_0(\xi)\rangle$, where $\zeta(\xi)$ is a smooth real function on $\mathcal{C}$, can only change the Berry phase by an integer multiple of 2π: The connection transforms as $\mathcal{A}(\xi) \to \mathcal{A}(\xi) - \nabla_\xi\zeta(\xi)$, leading to a change of $\Delta\mathcal{A} = \zeta(\xi(t=T)) - \zeta(\xi(t=0))$ of the connection. On a closed path, as the Berry phase is gauge independent, $\zeta(\xi(t=T)) - \zeta(\xi(t=0)) = 2\pi n$ with $n \in \mathbb{Z}$. (This is consistent with the Berry phase being gauge-independent: Unless the Berry phase happens to be an integer factor of 2π (which it is not in general), it cannot be "gauged away" by an arbitrary gauge transformation.)

In the following three cases, the Berry phase γ_C is nonzero: $\nabla \times \mathcal{A}$ is non-vanishing on a surface Σ in which $\mathcal{C} = \partial\Sigma$, or the curve C is on a surface which is not simply connected, or $\mathcal{A}$ is not singly defined. (Here, we assumed ξ is three-dimensional; we briefly mention the generalization to n-dimensions below.) We focus on the former case and write, using Stokes' theorem,

$$\gamma = \oint_{\partial\Sigma} \mathcal{A}(\xi) d\xi$$

$$= \int_{\Sigma} \mathbf{\Omega}(\xi).d\mathbf{S}, \tag{2.8}$$

where $\mathbf{\Omega}(\xi) \equiv \nabla_\xi \mathcal{A}(\xi) = i \langle \nabla_\xi \psi_0(\xi)| \times |\nabla_\xi \psi_0(\xi)\rangle$ is the *Berry curvature*. We note that the Berry phase described in Eq. 2.8 using Berry curvature remains meaningful on even closed surfaces (such as a torus or sphere) in which the boundary is an empty set; in this setting, $\mathbf{\Omega}$ is sometimes called the Berry flux density.

We finally mention that the Berry curvature has a simple generalization to n dimensions as the antisymmetric tensor $\Omega_{\alpha\beta} = -2\text{Im} \langle \partial_\alpha \psi_0(\xi)| \times |\partial_\beta \psi_0(\xi)\rangle$ where α, β are indices for the dimensions of ξ. To recover the definition of $\mathbf{\Omega}$ in Eq. 2.8, we note that $\mathbf{\Omega}_i = \epsilon_{ijk}\Omega_{jk}$ in three dimensions. Sometimes, $\mathbf{\Omega}$, or its multidimensional generalization $\mathbf{V}_\alpha = \epsilon_{\alpha\beta\gamma}\Omega_{\beta\gamma}$, is called the *Berry field*, and the name Berry curvature is reserved for $\Omega_{\alpha\beta}$. With this generalization, the Berry phase is written as the integral over the 2-form

$$\gamma = \frac{1}{2} \int_{\Sigma} d\xi^\alpha \wedge d\xi^\beta \, \Omega_{\alpha\beta}(\xi). \tag{2.9}$$

2.1.2. Gauge-Independent Formulation of the Berry Phase

We now derive a formulation of the Berry phase that is manifestly gauge independent [23, 30]. We start with the definition of the Berry curvature expressed in Eq. 2.8:

$$\begin{aligned}
\mathbf{\Omega}(\xi) &= \nabla_\xi \mathcal{A}(\xi) \\
&= i \langle \nabla_\xi n(\xi)| \times |\nabla_\xi n(\xi)\rangle \\
&= i\epsilon_{ijk} \langle \partial_{\xi_j} n(\xi)| \mathbb{1} |\partial_{\xi_k} n(\xi)\rangle \\
&= i\epsilon_{ijk} \langle \partial_{\xi_j} n(\xi)|n(\xi)\rangle \langle n(\xi)|\partial_{\xi_k} n(\xi)\rangle \\
&\quad + i\epsilon_{ijk} \sum_{m \neq n} \langle \partial_{\xi_j} n(\xi)|m(\xi)\rangle \langle m(\xi)|\partial_{\xi_k} n(\xi)\rangle \,.
\end{aligned} \tag{2.10}$$

In the first term above, $\langle \partial_{\xi_j} n(\xi)|n(\xi)\rangle$ is purely imaginary and hence the first term is real. We therefore ignore it, as it does not contribute to the Berry phase (see Eq. 2.7). We also use the following identity

$$\begin{aligned}
\langle m(\xi)| \, \nabla_\xi \, (H(\xi) \, |n(\xi)\rangle) &= E_n(\xi) \langle m(\xi)|\nabla_\xi n(\xi)\rangle + (\nabla_x i E_m(\xi)) \langle m(\xi)|n(\xi)\rangle \\
&= E_n(\xi) \langle m(\xi)|\nabla_\xi n(\xi)\rangle \\
&= \langle m(\xi)|(\nabla_\xi H(\xi))|n(\xi)\rangle + E_m(\xi) \langle m(\xi)|\nabla_\xi n(\xi)\rangle \,,
\end{aligned} \tag{2.11}$$

where $m \neq n$, i.e. $\langle m(\xi)|n\xi)\rangle = 0$. We thus have

$$\langle m(\xi)|\nabla_\xi n(\xi)\rangle = \frac{\langle m(\xi)|(\nabla_\xi H(\xi))|n(\xi)\rangle}{E_n - E_m}$$

$$\langle \nabla_\xi n(\xi) | m(\xi) \rangle = \frac{\langle n(\xi) | (\nabla_\xi H(\xi)) | m(\xi) \rangle}{E_n - E_m}. \tag{2.12}$$

We finally obtain

$$\gamma = \int_\Sigma d\mathbf{S}\, \mathrm{Im} \sum_{m \neq n} \frac{\langle m(\xi) | (\nabla_\xi H(\xi)) | n(\xi) \rangle \times \langle n(\xi) | (\nabla_\xi H(\xi)) | m(\xi) \rangle}{(E_n - E_m)^2}, \tag{2.13}$$

which is manifestly gauge independent.

2.1.3. Degeneracies, Winding Number and Chern Number

We now follow the References [23, 30] and relate the Berry phase and Berry curvature to the times a certain mapping of the Hamiltonian travels around a degeneracy point as the parameters of the Hamiltonian are smoothly changed. Consider the case of the curve $\mathcal{C}$ in the ξ-space passing through a degeneracy point ξ^* at which point $E_n(\xi^*) = E_0(\xi^*)$ for some $n \neq 0$. This makes the denominator in Eq. 2.15 zero. We now focus on the Berry curvature for points near such a degeneracy point.

We assume that at $\xi = \xi^*$, we have $E_n(\xi^*) = E_m(\xi^*)$ for some m in Eq. 2.15. Without loss of generality, we set $E_n(\xi^*) = 0$ and choose the origin at ξ^*. Near this point, the sum in Eq. 2.13 is dominated by a single term with a small denominator, so only two levels are relevant in the expression of the Berry phase. We limit ourselves to these two levels which we now call $|+\rangle$ and $|-\rangle$, with $E_+ \geq E_-$. We expand the effective two level Hamiltonian to linear order in $\xi - \xi^*$, yielding $H(\xi) \sim H(\xi^*) + (\xi - \xi^*) \cdot \nabla_\xi H(\xi^*)$. We obtain, for $|n\rangle \to |+\rangle$,

$$\mathbf{\Omega}_+(\xi) = \mathrm{Im} \frac{\langle +(\xi) | (\nabla_\xi H(\xi^*)) | -(\xi) \rangle \times \langle -(\xi) | (\nabla_\xi H(\xi^*)) | +(\xi) \rangle}{(E_+ - E_-)^2}. \tag{2.14}$$

The most generic two-level Hamiltonian for a crystal is

$$H = \epsilon(\mathbf{k})\sigma_0 + \frac{1}{2}\mathbf{d}(\mathbf{k}) \cdot \boldsymbol{\sigma} \tag{2.15}$$

Here, $\mathbf{k}$ is a vector in the Brillouin zone taking on the role of the parameter ξ, and $\mathbf{d}(\mathbf{k})$ is a 3D vector, whose details are given by the effective two-level Hamiltonian in question. For simplicity, from now on, we will consider the case of $\mathbf{d}(\mathbf{k}) = \mathbf{k}$. (We note that this Hamiltonian is encountered in many systems, such as graphene, Bogoliubov quasiparticles, spin-1/2 particles in a magnetic field, spin-orbit coupled systems, the Haldane model, quantum spin Hall effect, and many others.) As the ϵ term only changes the eigenvalues and not the eigenvectors, it cannot affect the Berry connection or the Berry curvature; hence we ignore it in our calculation. We also write $\mathbf{d}(\mathbf{k})$ as $\mathbf{d}(\mathbf{k}) = |\mathbf{d}(\mathbf{k})|(\sin\theta\cos\phi, \sin\theta\sin\phi, \cos\theta)$ in terms of the spherical coordinates

$(|\mathbf{d}(\mathbf{k})|, \theta, \phi)$ in the space where $\mathbf{d}$ is defined. While this parametrization of $\mathbf{d}(\mathbf{k})$ is well defined everywhere except at the degeneracy point, the corresponding eigenstates expressed in this parametrization are not. (We note that at the degeneracy, i.e. at $|\mathbf{d}| = 0$, the direction of the $\mathbf{d}$ vector and thhe polar coordinate parametrization of $\mathbf{d}$ is not well defined; it depends on from where one approaches the degeneracy.) These eigenstates, corresponding to eigenenergies $\mp 1/2|d|$, are:

$$\begin{aligned} |-, \mathbf{k}\rangle &= \left(\sin\theta/2\, e^{-i\phi}, -\cos\theta/2\right)^T, \\ |+, \mathbf{k}\rangle &= \left(\cos\theta/2\, e^{-i\phi}, \sin\theta/2\right)^T. \end{aligned} \tag{2.16}$$

In the above parametrization, $|-, \mathbf{k}\rangle$ is not well defined at the southern pole. A gauge transformation can only move the problematic pole on the sphere, hence the singularity cannot be avoided.

Going back to Eq. 2.14, we see that $\nabla_{\mathbf{k}} H = \boldsymbol{\sigma}/2$. After some algebra, we obtain

$$\boldsymbol{\Omega}_+(\mathbf{d}) = \frac{\mathbf{d}}{2|d|^3}. \tag{2.17}$$

The $\boldsymbol{\Omega}$ obtained here is similar to the field of a Dirac monopole. The Berry phase, given by a line integral around a closed curve C close to this monopole (i.e. degeneracy point), is $\gamma_\pm(C) = \mp\tilde{\Omega}/2$ with $\tilde{\Omega}$ being the solid angle subtended by the curve from the vantage point of the degeneracy.

We now relate the Berry phase to the winding number. In order to do that, we consider a system with $d_z = 0$. Then, the vector is in the equator plane. If the vector $\mathbf{d}$ winds around this degeneracy n times in counterclockwise direction and m times in the other, we get $\gamma_\pm(C) = \mp(n-m)\tilde{\Omega}/2$, where $\mp(n-m)$ is called *the winding number*. The phase factor $e^{i\gamma_\pm}$ does not depend on which surface one chooses the curve to be on, as this phase factor can change by an integer number of complete solid angles (by 4π every time the surface crosses the degeneracy). For completely real Hamiltonians, $\gamma_\pm(C) = \pi$ if the curve encircles the degeneracy for a single winding and $\gamma_\pm(C) = 0$ if it does not.

We next briefly outline the connection between the Berry phase, a geometrical property, to the Chern number, a topological invariant [7, 19, 30]. We motivate the result using systems that are relevant to this thesis. (A general proof, and the proof behind the identification of the Chern number with the Euler characteristic as shown in Eq. 2.1 remains beyond the scope of this work.)

We consider the unit sphere S^2 with $|\mathbf{d}(\mathbf{k})| = 1$ as our surface Σ for the demonstration of the argument. (We note again that in crystalline systems, the surface Σ in consideration

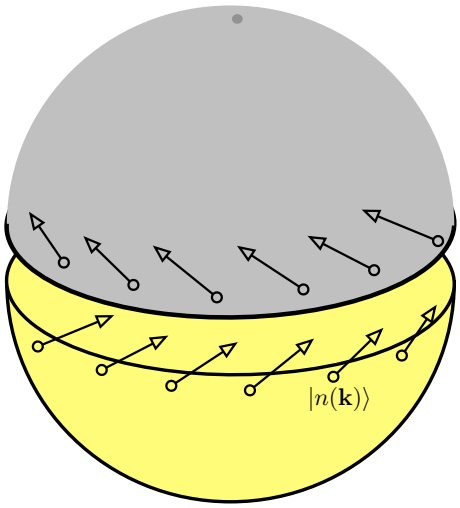

Figure 2.3: A sphere in the $\mathbf{d}(\mathbf{k})$-space, separated into two hemispheres. At each point on this sphere, the eigenkets $|n\rangle$ are defined. One of the hemispheres contains a point on which the curl of the $|n\rangle$ "vector" is not well defined. Within each hemisphere, $|n\rangle$ is smooth along the boundary, but as one goes across a boundary, a discontinuity presents itself in the phase of $|n\rangle$.

is the Brillouin zone.) When the Berry phase is nontrivial over a simply connected and closed surface, i.e. when the Berry curvature can be written as the nonzero curl of the Berry connection, the connection $\mathcal{A}(\mathbf{k})$ cannot be single-valued over S^2 [7, 23, 27, 30]. In the case of the sphere for Σ, one requires at least two different pieces of the surface of the sphere with their own definitions of $\theta = \pi$ point, as each piece will have a point where $\mathcal{A}(\xi)$ is not single-valued. For concreteness, we set said pieces to be the north and south hemispheres. We then have

$$\int_{S^2} \mathbf{\Omega} d\mathbf{S} = \int_{S^2_+} \mathbf{\Omega} d\mathbf{S} + \int_{S^2_-} \mathbf{\Omega} d\mathbf{S} \tag{2.18}$$

with $S^2_\pm$ corresponding to the north (south) hemispheres (see Figure 2.3). As the normal directions have opposite $\hat{z}$-directions, we also have, using Stokes' theorem,

$$\int_{S^2_\pm} \mathbf{\Omega} d\mathbf{S} = \pm \oint_{\partial S^2} \mathcal{A}(\xi) d\xi \tag{2.19}$$

with ∂S^2 being the equator circle. We therefore have the total Berry phase (times 2π) equal to the divergence of the integrals of the Berry connection over the equator circle, one in the northern hemisphere patch and one in the southern hemisphere patch. However, the wavefunction is defined over all of the sphere, which means the Berry connection itself can only differ by a gauge as one approaches the equator from both sides. The Berry phase itself over the equator, i.e. the integral of the connections, is gauge independent modulo 2π. This means calculating it over the same path with different gauge choices can result

only in a difference of $2\pi n$ with $n \in \mathbb{Z}$. This concludes the argument that

$$\frac{1}{2\pi}\int_{S^2} \mathbf{\Omega} d\mathbf{S} = n \tag{2.20}$$

is an integer. This integer n is called the *Chern number*. The Chern number is a topological invariant of the Hamiltonian and the parameter space in question.

2.2. Topological Insulators and Superconductors

In this section, we expose the topological structure underlying the quantum spin Hall effect (QSHE). We use the quantum spin Hall insulator as a main component for an implementation for the Maxwell's demon information engine in chapter 5 of this thesis. We also describe the underlying topological reason for the presence of Majorana fermions and Majorana states and topological superconductors in 1D or 2D, which are the subjects of chapters 3 and 4. We also consider the quantum Hall effect and its topological foundations in Appendix A.

2.2.1. The Haldane Model

In this section, we very briefly introduce the Haldane model [13] (see Figure 2.4). It has been devised by Haldane as a means to break time reversal symmetry locally without applying a magnetic field, essentially creating a quantum Hall insulator without a macroscopic magnetic field [15, 23, 34]. The model comprises of a 2D honeycomb lattice, with opposite on-site energies $\pm\Delta$ for the two sites in the unit cell, a nearest neighbor hopping t_1 and a next-nearest neighbor hopping $t_2 e^{\pm i\phi}$, with $t_{1,2} \in \mathbb{R}$. In the limit where the flux parameter ϕ vanishes, the model describes a two-atom hexagonal lattice such as boron nitride; in the limit where $\Delta = 0$, it reduces to a model for graphene. The effective one-particle Bloch Hamiltonian projected to the near-zero energy bands has the form:

$$H(\mathbf{k}) = \hbar v_F \mathbf{k} \cdot \boldsymbol{\sigma} + m(\mathbf{k})\sigma_z \tag{2.21}$$

where $\mathbf{k}$ is in the two-dimensional Brillouin zone of the honeycomb lattice. In the case of nonzero constant mass, this is simply a massive Dirac Hamiltonian. Even in the presence of weakly broken inversion symmetry, yielding a small but nonzero mass, the mass at $\mathbf{K}$ and $\mathbf{K}'$ points must be equal due to the time reversal symmetry. This massive Dirac Hamiltonian describes an ordinary insulator. However, in the case of nonzero $|\Delta|$ and with Δ alternating its sign with the symmetry of the lattice as described above, the inversion symmetry requires the masses at $\mathbf{K}$ and $\mathbf{K}'$ points to be equal in magnitude but opposite in sign.

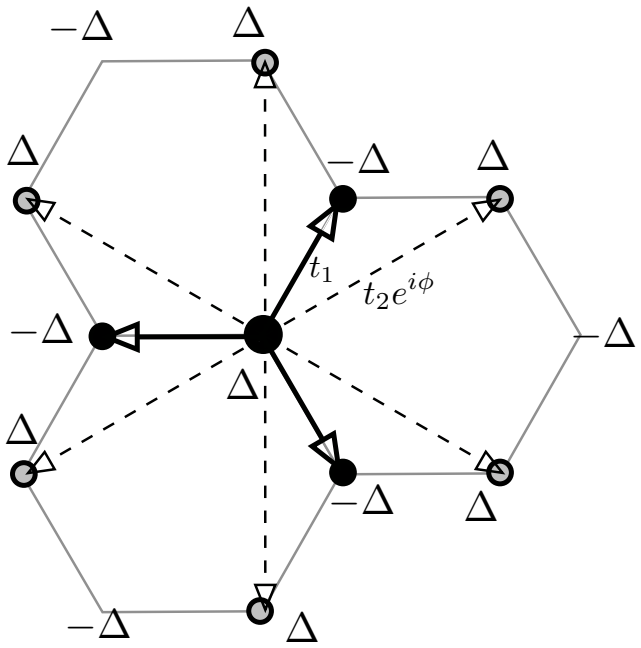

Figure 2.4: The Haldane model, with a staggered onsite energy $\pm\Delta$, nearest neighbor t_1 and next-nearest neighbor $t_2e^{i\phi}$ hopping on a honeycomb lattice.

We apply the results of subsection 2.1.3 to this Hamiltonian. The degeneracy, as before, is at the $\mathbf{k} = 0, m = 0$ point. When $m = 0$, the vector $\mathbf{d}(\mathbf{k})$ of Eq. 2.15 is given by $\mathbf{d}(\mathbf{k}) = (2\hbar v_F k_x, 2\hbar v_F k_y, 2m(k_x, k_y))$. For simplicity, we rescale our energy units so that $|\mathbf{d}| = 1$. At $m = 0$, the vector is in the equator in the Bloch sphere. The Chern number takes the form

$$n = \frac{1}{4\pi} \int d^2k (\partial_{k_x}\mathbf{d} \times \partial_{k_y}\mathbf{d}).\mathbf{d}, \tag{2.22}$$

which counts the times $\mathbf{d}$ winds around the $|\mathbf{d}| = 0$ point in the Bloch sphere as we integrate the system over the Brillouin zone, as discussed before. However, for a mass term slightly positive and then taken to zero, the Hamiltonian winds counterclockwise and for the opposite case, clockwise. In the case of $m \neq 0$, d_x and d_y can be zero without hitting the degeneracy point. This happens at the $(k_x, k_y) = (0, 0)$ point in the Brillouin zone. As k_x and k_y are taken to zero, the vector $\mathbf{d}$ points to the north or the south pole, depending on the sign of the mass term. We thus see that which pole $\mathbf{d}$ points to at the $(k_x, k_y) = (0, 0)$ point and which direction $\mathbf{d}$ winds around the degeneracy point when k is varied over the Brillouin zone as the mass is taken to zero are related.Therefore, in the integral over the Brillouin zone in Eq. 2.22, counting how many times the vector visits the north or south pole gives us the Chern number modulo 4π. Hence, each Dirac point contributes, $\pm e^2/2h$ to the Hall conductance (see Eq. A.10) with the sign given by the sign of the mass. In the case where both Dirac points have the same mass, these add up to zero. In the case where they have opposite mass, which corresponds to the quantum Hall

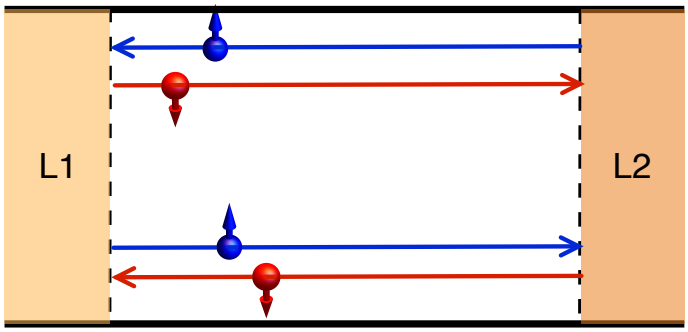

Figure 2.5: A quantum spin Hall insulator in 2D, with external attached leads L1 and L2. In this subsection, we usually consider closed systems, but we consider open systems with leads later. At each edge, a spin-polarized current flows: On the bottom edge, spin-down electrons move left and spin up electrons move right. The opposite is true for the top edge.

state, the total Chern number is 1, yielding a Hall conductance of e^2/h.

2.2.2. $\mathbb{Z}_2$ Topological Insulators

In this subsection, we briefly overview the theory of topological insulators in one or two dimensions that have a $\mathbb{Z}_2$ topological invariant, such as the quantum spin Hall insulators (see, for example, References [15, 22, 23, 34] for a detailed introduction).

The Hall conductivity is odd under time reversal (TR) $\mathcal{T}$: The direction of the magnetic field changes, and the sign of Hall voltage changes. Also, the direction of the edge current flow also changes under time reversal. This means that the topologically nontrivial states described above can only occur if the time reversal symmetry is broken. There is a different class of topological insulators, which we explore in this subsection (see Figure 2.5), in which the time reversal symmetry is not broken. However, time reversal symmetry implies that for each edge state traveling in one direction, another must also be present that is traveling in the other direction. These states must be topologically protected, hence scattering from one state to the other must somehow be forbidden. We thus would need another quantum number that distinguishes these states. In practice, this extra quantum number is the spin of the electrons. At a given edge lying in the left-right direction, spin-up electrons always travel (say) to the right and spin down electrons to the left. In literature, these edge states are sometimes called *helical* edge states as opposed to the chiral edge states of the quantum Hall insulator. The TKNN invariants for such Hamiltonians are identically zero, as the Chern number corresponding to the "clockwise Hall insulator" (edge states having a group velocity in clockwise direction) is exactly the opposite of that of the "counterclockwise Hall insulator" (edge states having a group velocity in counterclockwise direction), resulting in zero net Hall conductance.

Consider a Bloch Hamiltonian that is invariant under $\mathcal{T}$. We then have

$$\theta\mathcal{H}(\mathbf{k})\theta^{-1} = \mathcal{H}(-\mathbf{k}) \tag{2.23}$$

We now define an equivalence relation on the set of Hamiltonians satisfying the above condition, such that two Hamiltonians are considered to be equivalent if they can be adiabatically deformed into each other without closing the bulk band gap. There are two such equivalence classes, represented by a topological invariant $\nu = 1$ or $\nu = 0$ (or $\nu = \pm 1$, depending on the definition); hence the name $\mathbb{Z}_2$ topological insulator [31]. One way to observe that there are only two equivalence classes is to consider the band structure of such a system within the insulating bandgap (see Figure 2.6). We only need to consider half of the Brillouin zone (say, $0 \leq k \leq \pi/a$ for a 1D system, where a is the lattice constant) as TRS ensures that one half is the mirror symmetric of the other. In the bulk of the system, between the conduction and valence bands, there is a band gap. Within that gap, depending on the properties of the Hamiltonian, there can be edge states. If there are such states, they are present for every possible value of k. We also note that, at the Kramers degenerate points ($k = 0$ and $k = \pi/a$) for the simple example in Figure 2.6, an even number of such states should intersect; for simplicity, we assume they intersect pairwise. If the pair emerging from one point at $k = 0$ intersect at the same point at $k = \pi/a$, then these can be moved adiabatically out of the insulating bandgap by pushing them up or down. If, however, different pairs connect at different points, these edge states cannot be eliminated by moving them up or down, and they have to connect the conduction band to the valence band taken together. An equivalent method in 1D or quasi-1D systems to distinguish these two types of states is to see whether these states in one half of the band structure intersect the Fermi level an odd or an even number of times. We therefore relate the number N of pairs of edge modes intersecting the Fermi level over the whole Brillouin zone to the change $\Delta\nu$ in the topological invariant ν as $N = \Delta\nu \mod 2$.

There are other methods to construct the topological invariant of a $\mathbb{Z}_2$ topological insulator. One described by Fu and Kane [33] starts by forming the matrix $W_{mn}(\mathbf{k}) = \langle u_m(\mathbf{k})|\Theta|u_n(-\mathbf{k})\rangle$ where u_m are the Bloch wavefunctions. This matrix is unitary. Because the operator Θ is antiunitary with $\Theta^2 = -1$, we get $w_{nm}(\mathbf{k}) = -w_{mn}(-\mathbf{k})$. At the special points where $\mathbf{k}$ and $-\mathbf{k}$ coincide (for example, the four points $\Lambda_a \in \{\Gamma, X, X', M\}$ for a square lattice), the matrix w is antisymmetric. Choosing a continuous representation of u_m within the Brillouin zone which allows for a global branch cut choice for $\sqrt{\det[w(\Lambda_a)]}$, we define a "signum" function on the Pfaffian of w, and we define ν through $(-1)^\nu = \prod_a \mathrm{Pf}[w(\Lambda_a)]/\sqrt{\det[w(\Lambda_a)]}$, with the $\mathbb{Z}_2$ topological invariant given by $\nu \mod 2$ [34].

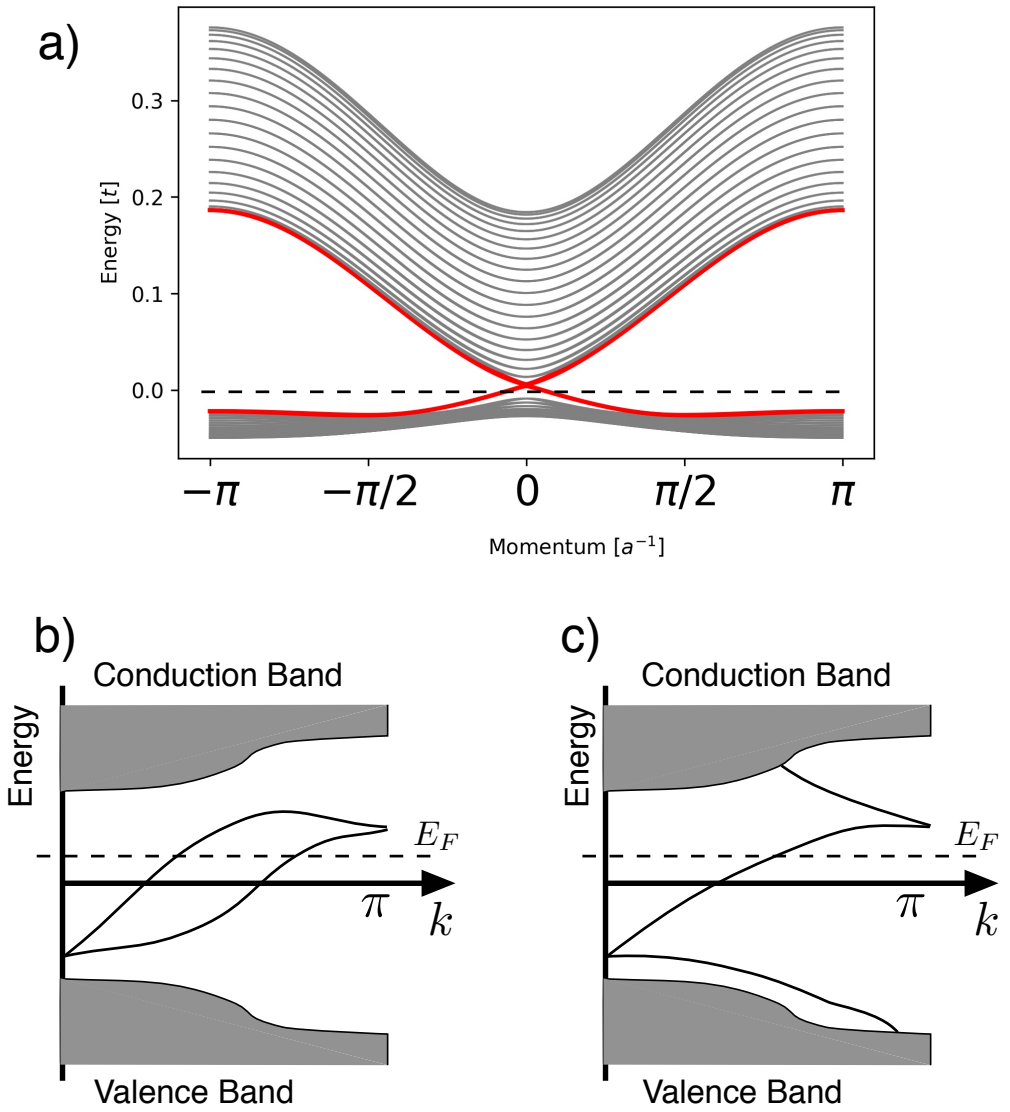

Figure 2.6: Example band structure of a $\mathbb{Z}_2$ topological insulator. (a) Band structure of a HgCdTe wire, using realistic parameters (see Table 2.7) but discretized on a square lattice of side $a = l_{\text{SO}}/40$. The lattice is $20a$ wide and infinitely long. $t = \hbar^2/2ma^2$ is the hopping parameter. The grey bands are the bulk bands and the red bands are the edge modes. If the Fermi level is held at the dashed line, the system will support topologically protected spin polarized edge modes. (b) Between the two Kramers degenerate points $k = 0$ and $k = \pi$, the Fermi level crosses the edge states an even number of times. Hence, this system is not topologically protected. (c) The Fermi level crosses the edge modes an odd number of times, thus the system is topologically nontrivial.

d (Å)	A (eV Å)	B (eV Å^2)	C (eV)	D (eV Å^2)	M (eV)
58	−3.62	−18.0	−0.0180	−0.594	0.00922
70	−3.42	−16.9	−0.0263	−0.514	−0.00686

Table 2.7: Material parameters for a HgCdTe quantum well for two different thicknesses d of the QW. In the second row, $M/B > 0$ and the system is in the nontrivial state [32].

In the case where the system conserves the S_z component of the spin, the picture of two counter-propagating edge modes, each with a Chern number, ends up being a much more realistic description, with two copies of a 2D quantum Hall insulator facing opposite directions stacked on top of each other (see Figure 2.5). We call the TKNN invariants of each copy $n_{\uparrow(\downarrow)}$. As mentioned, $n = n_\uparrow + n_\downarrow = 0$, but we can define a spin conductivity $n_\sigma = (n_\uparrow - n_\downarrow)/2$. Therefore topological invariant is given by $\nu = n_\sigma \mod 2$.

2.2.3. The Quantum Spin Hall Effect

We now provide a brief background review some physical systems that feature this $\mathbb{Z}_2$ topological protection in the form of QSHE. After the isolation of a single graphene layer [35, 36], QSHE was first predicted to occur in graphene by Kane and Mele [37]. However, the spin-orbit interaction (SOI) strength in graphene is not strong enough [38], with the nuclear mass of carbon being relatively low. The next important prediction came from Bernevig, Hughes and Zhang [32] in 2006 in the form of QSHE in CdTe/HgTe/CdTe quantum wells (QWs) that are thin enough to have inverted band structures. We discuss this system and the general properties of its Hamiltonian (the BHZ Hamiltonian, named after the authors) in the following paragraphs. Experimental verification soon arrived as reported in a paper by König *et al.* in 2007 [39], followed by edge channel transport experiments [40]. Another system predicted to manifest QSHE, which is of importance for this thesis, is the InAs/GaSb QW. These quantum wells were predicted by Liu *et al.* in 2008 [41]. First experimental evidence came in 2010 by Knez *et al.* [42].

We start by considering the HgTe/CdTe QWs. Both the HgTe and the CdTe part of the QW have zinc blende lattice structures with two different types of atoms. The inversion symmetry is broken and the relevant Hamiltonian must have a bulk inversion asymmetry (BIA) term. However, its presence does not change the overall topological properties of the system and for simplicity we shall disregard this term in the following discussion.

In their paper predicting the QSHE in HgTe/CdTe QWs [32], Bernevig, Hughes and Zhang start with the 6-band bulk $k.P$ model of Kane, focusing on the *s*-type Γ_6 and *p*-type Γ_8 bands around the Γ point in the Brillouin zone. In CdTe, the energy of Γ_6 is higher than that of Γ_8, and the effective mass of the former is positive and the effective mass of the latter is negative. In CdTe, this situation is inverted due to the relatively large SOC in HgTe caused by the heavy nucleus of Hg. Here, the light hole Γ_8 is the conduction band, the heavy hole band becomes the first valence band and Γ_6 is below the first valence band. The light hole and heavy hole bands in HgTe are degenerate. The HgTe QW sandwiched between CdTe keeps this inverted band behavior down to a critical thickness of $d_c = 6.3$nm, below which the CdTe band structure asserts itself.

For QW thicknesses $d_{QW} > d_c$, we consider the electron and hole bands discussed above. Ignoring BIA, Kramers degeneracy requires these bands to be doubly degenerate; without SOI, the degenerate states will simply be the spin-up and spin-down states. We construct the Hamiltonian using these basis, acting on the wavefunction

$$\Psi^T = \begin{pmatrix} |E+\rangle \\ |H+\rangle \\ |E-\rangle \\ |H-\rangle \end{pmatrix}, \tag{2.24}$$

where E, H represent the electron-and hole-states and the $\pm$ specify the spin direction. As the electron and hole states have opposite parity (one is *s*-like and the other is *p*-like), the Hamiltonian elements connecting them should be odd in $\mathbf{k}$ and therefore linear in lowest order. The heavy hole $|H\pm\rangle$ *p*-bands are of the form $|H\pm\rangle \sim |\pm p_\pm, \uparrow\downarrow\rangle$ with $p_\pm = p_x \pm ip_y$, so they need to be related to each other by $k_\pm$ terms in general. The diagonal terms cannot be odd, so they must contain terms of order k^0 and k^2 to the lowest order. Due to the degeneracy of the subbands, the basic Hamiltonian cannot couple the spin-up states to the spin-down states of the same band. A coupling between the same spin states of different bands would involve a second order process, which we ignore. Therefore, the Hamiltonian reduces to a block Hamiltonian with zero off-diagonal terms:

$$\mathcal{H} = \begin{pmatrix} h(\mathbf{k}) & 0 \\ 0 & h^*(-\mathbf{k}) \end{pmatrix}, \tag{2.25}$$

where

$$\begin{aligned} h(\mathbf{k}) &= \epsilon(\mathbf{k})\sigma_0 + d_\alpha(\mathbf{k})\sigma_\alpha, \epsilon(\mathbf{k}) && = C - Dk^2, \\ d_\alpha(\mathbf{k}) &= (Ak_x, -Ak_y, M(\mathbf{K})), \\ M(\mathbf{K}) &= M - Bk^2 \end{aligned} \tag{2.26}$$

and A, B, C, D and M are material parameters depending on, among other things, the QW geometry and thickness (see Table 2.7.)The corresponding bulk energy spectrum is

$$E_\pm = \epsilon(k) \pm \sqrt{A^2k^2 + M^2(k)}. \tag{2.27}$$

Here, the parameter M is the energy difference between the $|E\rangle$ and $|H\rangle$ bands. The sign of M changes at the critical thickness. Below the critical thickness d_c, $M > 0$ and the bands are ordered in the usual way. Above d_c, $M < 0$ and the bands are inverted. At d_c, $M = 0$; if $b = 0$ also, the system becomes two copies of a massless Dirac Hamiltonian.

There is no valley degree of freedom as in graphene; the system has only two Dirac cones (corresponding to spin degrees of freedom) as opposed to the four Dirac cones in graphene. Also, as we are dealing with a non-relativistic system, a quadratic dispersion is allowed. Sometimes the term M is therefore referred to as the Dirac mass and the term B (but, strangely enough, not B^{-1}) is referred to as the Newtonian mass in the literature.

For $B = 0$, this is simply two copies of the massive Dirac Hamiltonian, which we discussed in subsections 2.1.3 and 2.2.1. Then, whether the vector $\mathbf{d}$ visits the north or the south pole depends only on the sign of M, as before. However, in the case of nonzero B, the vector starts at the pole designated by the sign of M (north pole for $M > 0$) for $k_x, k_y \to 0$ and ends at the pole designated by the sign of B (south pole for $B > 0$) for $k_x, k_y \to \infty$. Thus, the winding number n is given by $n = +1$ if $M/B > 0$, carrying a Hall conductance of e^2/h, and $n = 0$ for $M/B < 0$, yielding a normal insulator.

On the other block of $\mathcal{H}$ where we get $h^*(-\mathbf{k})$, the sign analysis for M and B do not change, but the rotation directions change due to the linear part of $h(k_x, k_y)$. Therefore, the total Chern number is zero (there is zero Hall charge conductance). However, as the two diagonal parts represent different spins, the spin conductance of the Hall edge channel (the spin Hall conductance), which is the difference between the two Hall conductances, add to $2e^2/h$.

We now present the explicit edge state solutions of the BHZ Hamiltonian without the BIA and SIA terms [15]. (For completeness, we depict these terms in Appendix H.) We consider a semi-infinite plane $x > 0$. k_y in this case a good quantum number. We first see $k_y = 0$, and replace k_x by $-i\partial_x$ and get a block-diagonal equation. The eigenstates are of the form $\Psi_\uparrow = (\psi_0, 0)^T$ and $\Psi_\downarrow = (0, \psi_0)^T$ for the spin up and down components, with $\psi_0 = (\psi_+, \psi_-)^T$. The equation for ψ_0 reads:

$$[\epsilon(-i\partial_x, 0) + M(-i\partial_x, 0)\tau_z - isA\partial_x\tau_x]\,\psi_0 = E\psi_0, \tag{2.28}$$

where $s = 1$ for the upper block and $s = -1$ for the lower block. For simplicity, we focus on the upper block and we ignore the ϵ term. The remaining terms have particle-hole symmetry, so $E = 0$ solution is possible. With a look towards a possible edge state, we try an ansatz of $\psi_0 = \phi_0 e^{\lambda x}$. Near $\mathbf{k} = 0$, the real part of the solutions reads

$$\psi_0(x) = \begin{cases} N_\uparrow(e^{\lambda_1 x} - e^{\lambda_2 x})\phi_+, & A/B < 0 \\ N_\downarrow(e^{-\lambda_1 x} - e^{-\lambda_2 x})\phi_-, & A/B > 0, \end{cases} \tag{2.29}$$

where $\lambda_{1,2} = (A \pm \sqrt{A^2 - 4MB})/2B$ and $N_{\uparrow,\downarrow}$ are normalization constants and $\phi_\pm$ are spinors. Projecting the Hamiltonian to these edge states, we get an effective edge Hamil-

tonian as

$$H_{\text{edge}} = Ak_y\sigma_z. \tag{2.30}$$

We therefore have two states exponentially locked to an edge. A simple calculation shows that these have opposite spins and opposite group velocities, leading to two counter-propagating opposite spin states. as it stands, because the Hamiltonian is block-diagonal, these states cannot backscatter into each other, so they are protected.

2.2.4. Majorana States and The Kitaev Chain

In this subsection, we present a brief background overview of Majorana states and the Kitaev chain model. The original research in this thesis related to this topic is focused on topological phase transitions in 1D and quasi-2D *s*-wave and *p*-wave topological superconductors, which support Majorana edge states in their topologically nontrivial phase. Therefore, we present an introduction to Majorana states. For their history, physical structure, their prediction and possible detection in condensed matter systems and their use in topological quantum computation as non-Abelian anyons, we refer the reader to several reviews and to the references therein [15, 16, 43–46].

A Majorana fermion is a fermion that is its own antiparticle. Ettore Majorana originally asked the question in his 1937 paper [47, 48] whether a symmetric theory of electrons and positrons were possible, just before his disappearance. In condensed matter physics, some collective quasiparticle excitations can be their own antiparticles under certain conditions, which are referred to as Majorana states. Some of the systems in which Majorana states are posited to arise as collective quasiparticle excitations may include some systems related to $p + ip$ superconductors [15, 44, 49, 50], He^3 superfluids [51–53], in the surface of Sr_2RuO_4 at the center of superconducting vortices [54], quantum spin Hall insulators placed near *s*-wave superconductors with the presence of a magnetic field, semiconductor structures with high SOC in proximity to *s*-wave superconductors [50, 55, 56] and atomic chains embedded in *s*-wave superconductors [57, 58]. These Majorana states are non-Abelian anyons, meaning exchange operations involving them do not commute. Such operations are called *braiding* operations and can be used as a means to implement quantum computers [43, 46, 59–62]. The topologically protected and nonlocal nature of Majorana fermions, as well as their chargelessness (which we discuss below) make Majorana fermions good candidates for quantum memory [44].

Any fermion can be written as a sum of two Majorana fermions, or one can construct Majorana fermion operators from any fermion operator. Consider a generic Fermion an-

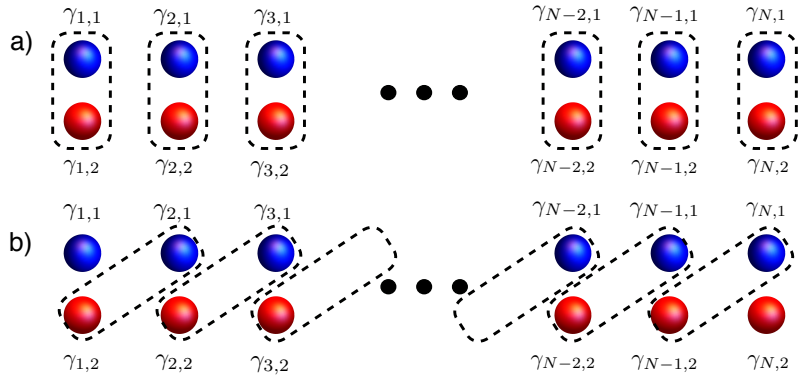

Figure 2.8: A Kitaev chain of N sites. (a) Each fermion on the site can be divided into a real and an imaginary part, each a Majorana fermion. (b) The Hamiltonian, when diagonalized, couples Majorana fermions of different sites, leaving a pair uncoupled, each one at a different end.

nihilation operator c_α, where α is a general quantum state label. Its antiparticle operator is the creation operator $c_\alpha^\dagger$. These obey the usual commutation relation $\{c_\alpha, c_\beta^\dagger\} = 2\delta_{\alpha\beta}$. We separate these into their Hermitian and anti-Hermitian parts as usual:

$$c_\alpha = \frac{1}{2}\left(\gamma_{\alpha,1} + i\gamma_{\alpha,2}\right). \tag{2.31}$$

The relations below can be shown using simple algebra:

$$\begin{aligned}
\gamma_{\alpha,1} &= c_\alpha^\dagger + c_\alpha \\
\gamma_{\alpha,2} &= i(c_\alpha^\dagger - c_\alpha) \\
\gamma_{\alpha,i} &= \gamma_{\alpha,i}^\dagger \qquad\qquad (i = 1, 2) \\
\{\gamma_{\alpha,i}, \gamma_{\beta,j}\} &= 2\delta_{\alpha\beta}\delta_{ij} \\
\gamma_{\alpha,i}^2 &= 1 \\
c_\alpha^\dagger c_\alpha &= \frac{1}{2}(1 + i\gamma_{\alpha,1}\gamma_{\alpha,2}).
\end{aligned} \tag{2.32}$$

These relations show they are their own antiparticles and that they are indeed fermions with the proper anti-commutation relations. Moreover, we need both $\gamma_{\alpha,1}$ and γ_{α_2} to construct the fermion number operator $c_\alpha^\dagger c_\alpha$. However, there is nothing new in this picture as of yet: It is just another way of writing an electron operator. One might just as well use electron operators. Another such example is a general Nambu spinor: $\Psi = (c_\uparrow^\dagger, c_\uparrow)^T$ is in itself a Majorana fermion: $\sigma_x(\Psi^\dagger)^T = \Psi$, where $\sigma_x K$ can be taken as the charge conjugation.

The emergence and protection of Majorana states can be demonstrated in the Kitaev chain model [63]. Kitaev considers a 1D chain of N sites hosting a possible fermion on each site (see Figure 2.8). The Hamiltonian has a p-wave superconducting pairing Δ, a

nearest neighbor hopping term t and an onsite energy μ:

$$\mathcal{H} = -\mu \sum_{i=1}^{N} c_i^\dagger c_i - \sum_{i=1}^{N-1} (t c_{i+1}^\dagger c_i + \Delta c_i c_{i+1} + \text{h.c.}). \tag{2.33}$$

We note that the superconducting pairing does not couple opposite spin particles; in fact, spin does not enter this model. (Such a system can be realized as a spin-polarized *p*-wave limit of an *s*-wave topological superconductor.) We also assume μ, t and Δ does not depend on the site and that t and Δ are real for simplicity, and we choose both of them to be positive. Moreover, we set the zero of our energy so that $\mu = 0$. To simplify the results, we consider the case $t = \Delta$. In this case, using similar definitions to those in Eq. 2.31, we arrive at the following:

$$\mathcal{H} = -it \sum_{i=1}^{N-1} \gamma_{i,2} \gamma_{i+1,1} \tag{2.34}$$

with the site indices i added to the Majorana operators. (We shifted the zero of our energy to remove constant terms.) An interesting point is there are N sites but $N-1$ terms in this Hamiltonian. We now consider a fermion defined by taking two Majorana particles from adjacent sites as $\tilde{c}_i = (\gamma_{i+1,1} + i\gamma_{i,2})/2$ (see Figure 2.8). We thus arrive at the following diagonalization of the Hamiltonian:

$$\mathcal{H} = 2t \sum_{i=1}^{N-1} \tilde{c}_i^\dagger \tilde{c}_i \tag{2.35}$$

As mentioned above, there is one less term than there are sites in this Hamiltonian. Indeed, one Majorana from each end of the wire, namely $\gamma_{1,1}$ and $\gamma_{N,2}$ are missing from it. This means that their presence or absence has no effect on the energy; they are zero energy excitations. Together, they form a normal fermion $\tilde{c}_M = (\gamma_{N,2} + i\gamma_{1,1})/2$, but this fermion is localized to the separate ends of the wire. This "superconducting" Hamiltonian can have an odd number of quasiparticles in its ground state due to $\tilde{c}_M$ not carrying energy. These "odd parity" superconductors have a nontrivial edge state.

For nonzero μ and $t \neq \Delta$, as long as $|\mu| < 2t$, i.e. the Hamiltonian energy of creating a single $\tilde{c}_i$ particle remains in the gap, the physics described above still holds, but now the Majorana state has an exponentially decaying tail into the bulk of the atomic chain. As long as the chain is large enough so that the decaying tails of the wavefunctions at each end do not overlap, we have the physics described above. If there is significant overlap, the Majorana states at the two ends hybridize to form an ordinary fermion.

2.2.5. Topological Superconductors

In this subsection, we consider both *p*-wave and *s*-wave topological superconductors in one and two dimensions. We consider the topological nature of these systems and make a connection to the Majorana states discussed previously. We finally comment on the relation between the *s*-wave and *p*-wave Bogoliubov-de Gennes (BdG) systems and very briefly touch upon possible experimental setups that may contain Majorana states. For a more detailed introduction, we refer the reader to, for example, References [16, 43, 44].

We start with examining the *p*-wave systems with the following model Hamiltonian:

$$H = \int d^2\mathbf{r} \left[\psi^\dagger \left(\frac{p^2}{2m} - \mu \right) \psi + \frac{1}{2}\Delta(e^{i\phi}\psi(p_x - ip_y)\psi + \text{H.c.}) \right], \tag{2.36}$$

where $\psi(\mathbf{r})$ annihilates a spinless fermion at position $\mathbf{r}$ with effective mass m. μ is the chemical potential, $\Delta > 0$ is the superconducting *p*-wave coupling and ϕ is the superconducting phase. (We note that in 1D, this Hamiltonian corresponds, up to some constants, to the continuum version of the Kitaev chain Hamiltonian of Eq. 2.33.) We then consider periodic boundary conditions in real space (or we can alternatively regularize the Hamiltonian on a lattice) to arrive at the BdG Hamiltonian in the momentum space for a spinless *p*-wave superconductor:

$$H = \frac{1}{2} \int \frac{d^2\mathbf{k}}{(2\pi)^2} \, \Psi^\dagger(\mathbf{k}) \, \mathcal{H}_{\text{BdG}} \, \Psi(\mathbf{k}) \tag{2.37}$$

with the BdG Hamiltonian given explicitly as

$$\mathcal{H}_{\text{BdG}} = \begin{pmatrix} \epsilon(k) & -i\Delta e^{-i\phi}(k_x - ik_y) \\ i\Delta e^{i\phi}(k_x + ik_y) & -\epsilon(k) \end{pmatrix}. \tag{2.38}$$

Here, the Nambu spinor $\Psi^\dagger(\mathbf{k}) = (\psi^\dagger(\mathbf{k}), \psi(-\mathbf{k}))^T$ and the kinetic term $\epsilon(k) = k^2/2m - \mu$.

The BdG Hamiltonian in Eq. 2.38 is similar to one block of the BHZ Hamiltonian in Eq. 2.25 and the Hamiltonians discussed in subsections 2.1.3 and 2.2.1. We can write the BdG Hamiltonian as

$$\mathcal{H}_{\text{BdG}} = -\Delta\tau_x(k_x \sin\phi + k_y \cos\phi) + \Delta\tau_y(k_x \cos\phi - k_y \sin\phi) + \epsilon(k)\tau_z \tag{2.39}$$

where τ_i for $i = 1, 2, 3$ are Pauli matrices in the particle-hole space. Similar to the BHZ case, we see that for $\mu < 0$, the vector $\mathbf{d}$ starts and ends at the north pole, signifying a trivial system. For $\mu > 0$, it goes from the north to the south pole, giving a Chern number $n = -1$, indicating a topologically nontrivial case.

As discussed in the previous subsections, such a Hamiltonian would support zero-

energy edge modes that are topologically protected. We now show that such edge states are Majorana states. It is possible to do this by taking the small k limit of the Hamiltonian where one can ignore the $k^2/2m$ term. One then calculates the edge-state solutions, from which one can show these solutions represent antiparticles of themselves. However, a much easier way is to consider the symmetries of the Hamiltonian. This BdG Hamiltonian has a particle-hole symmetry,

$$\Xi \mathcal{H}_{\text{BdG}}(\mathbf{k})\Xi^{-1} = -\mathcal{H}_{\text{BdG}}(-\mathbf{k}), \tag{2.40}$$

where $\Xi = \tau_x K$ is an antiunitary symmetry with K the complex conjugation operator. Therefore, every eigenstate at energy E has a counterpart at energy $-E$, related to each other with particle-hole symmetry. If there is a state at $E = 0$, and we know there is an edge state of that form because of the topological argument, the operator that creates a "particle" in that state would also destroy said particle, therefore the state would be a Majorana state.

We next consider an *s*-wave topological superconductor, with both spins present in the model, as well as an *s*-wave superconductor coupling strength and particle-hole symmetry. The system proposed by Oreg *et al.* [56] and Lutchyn *et al.* [55] uses Rashba spin-orbit coupling in a semiconductor wire, grown in proximity to an *s*-wave superconductor. The superconducting coupling is induced in the semiconductor wire by proximity to the superconductor. This superconducting gap, which is the bulk band gap that the quasiparticles see, can be closed by a Zeeman field. The Rashba spin-orbit coupling provides the competing mechanism to the Zeeman field to reopen the band gap with inverted bands, as in the QSH insulator. We therefore start with the Hamiltonian of a wire in the xy-plane with Rashba SOI coupling strength α under an applied magnetic field $\mathbf{B}$, which enters the Hamiltonian through the Zeeman term:

$$H_0 = \sum_{\sigma=\uparrow,\downarrow} \int d^2\mathbf{r}\, \psi_\sigma^\dagger(\mathbf{r})\mathcal{H}_0(\mathbf{r})\psi_\sigma(\mathbf{r}) \tag{2.41}$$

with the single particle Hamiltonian $\mathcal{H}_0(\mathbf{r})$ given by

$$\mathcal{H}_0(\mathbf{r}) = \frac{p^2}{2m} + V(\mathbf{r}) - \mu + \alpha\,(\mathbf{p}\times\boldsymbol{\sigma})\cdot\hat{z} + \frac{g\mu_B}{2}\mathbf{B}\cdot\boldsymbol{\sigma}, \tag{2.42}$$

where g is the Landé factor and μ_B is the Bohr magneton. The operator $\psi_\sigma^\dagger(\mathbf{r})$ creates an electron of spin σ at the position $\mathbf{r}$. We next consider the *s*-wave pairing term, which couples particles and holes through the usual artificial doubling of the degrees of freedom, by adding a time reversed version of the above Hamiltonian and writing the coupling between the above Hamiltonian and its time reversed version. The final Hamiltonian

reads as:

$$H = \frac{1}{2}\int d^2\mathbf{r}d^2\mathbf{r}'\,\Psi^\dagger(\mathbf{r})\mathcal{H}(\mathbf{r},\mathbf{r}')\Psi(\mathbf{r}), \tag{2.43}$$

where $\Psi = (\psi_\uparrow(\mathbf{r}), \psi_\downarrow(\mathbf{r}), -i\psi^\dagger_\downarrow(\mathbf{r}), i\psi^\dagger_\uparrow(\mathbf{r}))^T$ and the single particle Hamiltonian density $\mathcal{H}$ is given by

$$\mathcal{H}^{\text{SW}}_{\text{BdG}}(\mathbf{r},\mathbf{r}') = \begin{pmatrix} H_0(\mathbf{r})\delta(\mathbf{r}-\mathbf{r}') & \Delta^*(\mathbf{r}) \\ \Delta(\mathbf{r}) & -\sigma_y H_0^*(\mathbf{r})\sigma_y\delta(\mathbf{r}-\mathbf{r}') \end{pmatrix}. \tag{2.44}$$

For simplicity, in the following, we assume the superconducting pairing is translationally symmetric and isotropic ($\Delta^*(\mathbf{r}) = \Delta^*((|\mathbf{r}|))$. Our fundamental results about the topological properties of this Hamiltonian are not affected. The superfluous nature of two of the degrees of freedom is given by the fact that the Hamiltonian density in Eq. 2.44 has particle-hole symmetry, given by $\Xi\mathcal{H}^{\text{SW}}_{\text{BdG}}(\mathbf{r},\mathbf{r}')\Xi^\dagger = -\mathcal{H}^{\text{SW}}_{\text{BdG}}(\mathbf{r},\mathbf{r}')$ with $\Xi = \tau_y\sigma_y K$. The zero-energy eigensolutions of this Hamiltonian are Majorana states.

We next consider the spectrum of the *s*-wave BdG Hamiltonian and then how an effective *p*-wave system emerges from it in the full polarization, almost depleted wire limit. For constant μ, Δ, α and B, the spectrum is easily obtained [56]:

$$E^2_\pm = \varepsilon^2 + B^2 + \Delta^2 + (\alpha p)^2 \pm 2\sqrt{B^2(\Delta^2+\varepsilon^2) + (\alpha p)^2\varepsilon^2} \tag{2.45}$$

with $\varepsilon = p^2/2m - \mu$. Near $p = 0$, this spectrum reads $E^2_0 = (B - \sqrt{\Delta^2+\mu^2})^2$. The topological phase transition is governed by $B^2 - (\Delta^2 + \mu^2)$; if this parameter is positive, the gap is magnetic field dominated and the system is in a topologically nontrivial state supporting protected Majorana edge modes; if it is negative, the system is in a trivial state and the gap is pairing-dominated.

Finally, we consider this Hamiltonian in 1D and near $p = 0$. We keep the terms up to linear in p. We then switch on a small magnetic field to separate the spin-polarized bands in energy. We pick the Fermi level so that one such spin polarized band is full, while its counterpart is not. This leads to an effective spin-polarized (sometimes referred to as "spinless") Hamiltonian, a necessary step to obtain spinless *p*-wave topological superconductors [16, 43, 55, 56].

2.3. Generalized Classification of Topological Phases of Matter in Arbitrary Dimensions

We now consider the classification of topological insulators and superconductors according to their discrete irreducible symmetries. These materials are divided into ten sym-

metry classes, called the tenfold way, according to whether they obey various antiunitary symmetries, namely time reversal symmetry, particle-hole symmetry and chiral symmetry. Whether a single-particle Bogoliubov-de Gennes Hamiltonian can support a topologically nontrivial phase, and which group the topological invariant belongs to, can be immediately read off from this "periodic table". These classifications match the classification of symmetric spaces by Élie Cartan [64, 65]. Dyson, while considering the level statistics of systems and using the earlier work of Wigner, previously classified the Hamiltonians into three symmetry classes (the threefold way) [66]. Altland and Zirnbauer [67] generalized this classification to its modern form by including superconducting symmetry classes.

In this section, we provide the periodic table of topological insulators and superconductors for generalized dimensions. We mention some of the structure of this table, such as the Bott periodicity [68] and dimensional reduction without proof. We note the classes and dimensions (namely, classes BDI and D, in one or two dimensions) that are relevant to this thesis. Finally, we describe the connection between the transport properties and the *S*-matrix of a system and its topological classification as well as how one can determine the topological invariants from the *S*-matrix [69].

2.3.1. The Periodic Table of Topological Materials: The Tenfold Way

In topologically nontrivial systems, the topological properties and the existence of a gapless edge state cannot be changed by small deformations in the system or small changes in their first quantized Hamiltonians. Therefore, a discussion that relates the symmetries of said Hamiltonians to their topological properties cannot include symmetries such as translational symmetry, which can be broken with disorder while still not changing the topological properties [70]. In fact, any unitary symmetry cannot in general be used to make such classification. If a Hamiltonian is invariant under such a symmetry, it can be block-diagonalized in the representation of said symmetry. This section deals with the remaining symmetry properties of these irreducible blocks, which are the discrete antiunitary symmetries.

We consider the general BdG form of a fermionic Hamiltonian:

$$H = \sum_{\alpha,\beta} \psi_\alpha^\dagger(\mathbf{r}) \mathcal{H}(\mathbf{r}, \mathbf{r}') \psi_\beta(\mathbf{r}'), \tag{2.46}$$

where the fermionic creation and destruction operators obey the canonical anti-commutation relation $\{\psi_\alpha^\dagger, \psi_\beta\} = \delta_{\alpha\beta}$ and α, β are generalized quantum numbers, which can include an orbital index, a spin index and for lattice Hamiltonians, a position index. We assume

that there are N of them. If the BdG Hamiltonian $\mathcal{H}$ has an antiunitary symmetry, it can take one of the following forms:

$$\begin{aligned}\mathcal{T} :&\Theta^\dagger \mathcal{H}^* \Theta = +\mathcal{H} \\ \mathcal{C} :\ &\Xi^\dagger \mathcal{H}^* \Xi = -\mathcal{H}.\end{aligned} \tag{2.47}$$

We call the first symmetry ($\mathcal{T}$) the time-reversal symmetry (with a representation $\Theta = U_\Theta K$) and the second one ($\mathcal{C}$) the particle-hole symmetry (with a representation $\Xi = U_\Xi K$). Here, K is the complex conjugation operator and U_Θ, U_Ξ are unitary operators. Essentially, these symmetries are determining whether these Hamiltonians are purely real or purely imaginary up to a unitary transformation. We note that a Hamiltonian can have both of these symmetries at the same time. (For example, a Hamiltonian given by $C\sigma_x$, which is purely real, can be rotated to $C\sigma_y$, which is purely imaginary, where C is a real constant.) These are antiunitary symmetries, hence their representations can square to $\pm\mathbb{1}$. There are therefore ten possible ways that a BdG Hamiltonian can interact with these symmetries. Each symmetry has three possible outcomes: The symmetry is present and its square gives $+\mathbb{1}$; it is present with a square of $-\mathbb{1}$, it is absent; we label these cases with $\mathcal{T}, \Xi = +1, -1$ and 0, respectively. This accounts for $3 \times 3 = 9$ of the possible cases. For the tenth case, we consider the chiral symmetry $\mathcal{S} = \mathcal{T}.\mathcal{C}$, with the representation Π. (The symmetries are named $\mathcal{T}$ for "time reversal", $\mathcal{C}$ for "charge conjugation" and $\mathcal{S}$ for "sublattice symmetry".) It is a unitary operation, but whether a Hamiltonian has this symmetry or not, is given by the anticommutator of the Hamiltonian with a unitary operator rather than the commutator. For the cases where the Hamiltonian has either $\mathcal{T}$ or $\mathcal{C}$ symmetry, but not both, the system has no $\mathcal{S}$ symmetry (which we denote with $\Pi = 0$). If the system has both of these symmetries, then it also has the $\mathcal{S}$ symmetry, which we denote with $\Pi = 1$. For the case where the system has neither $\mathcal{T}$ nor $\mathcal{C}$ symmetry, the $\mathcal{S}$ symmetry may or may not be there, giving $\Pi = 1$ or $\Pi = 0$. This provides the tenth case.

The "periodic table of topological insulators", which we reproduce in this subsection, considers the unitary group of the time evolution operator obtained from the $N \times N$ single particle Hamiltonian $\exp(i\mathcal{H}t)$ (see Table 2.9). The first column is Cartan's notation for the relevant space. The second group of columns denotes whether the space has the relevant symmetry. The third column denotes whether the system is topologically nontrivial, and shows the group to which its topological invariant belongs to.

To highlight the relation between the Cartan classification and topological properties, we note the examples of class A and class AI in Table 2.9. Class A has no antiunitary symmetries. Consider a Hamiltonian in this class, discretized over a lattice, expressed as

Symmetry				Dimension							
A-Z	Θ	Ξ	Π	1	2	3	4	5	6	7	8
A	0	0	0	0	$\mathbb{Z}$	0	$\mathbb{Z}$	0	$\mathbb{Z}$	0	$\mathbb{Z}$
AIII	0	0	1	$\mathbb{Z}$	0	$\mathbb{Z}$	0	$\mathbb{Z}$	0	$\mathbb{Z}$	0
AI	1	0	0	0	0	0	$\mathbb{Z}$	0	$\mathbb{Z}_2$	$\mathbb{Z}_2$	$\mathbb{Z}_2$
BDI	1	1	1	$\mathbb{Z}$	0	0	0	$\mathbb{Z}$	0	$\mathbb{Z}_2$	$\mathbb{Z}_2$
D	0	1	0	$\mathbb{Z}_2$	$\mathbb{Z}$	0	0	0	$\mathbb{Z}$	0	$\mathbb{Z}_2$
DIII	-1	1	1	$\mathbb{Z}_2$	$\mathbb{Z}_2$	$\mathbb{Z}$	0	0	0	$\mathbb{Z}$	0
AII	-1	0	0	0	$\mathbb{Z}_2$	$\mathbb{Z}_2$	$\mathbb{Z}$	0	0	0	$\mathbb{Z}$
CII	-1	-1	-1	$\mathbb{Z}$	0	$\mathbb{Z}_2$	$\mathbb{Z}_2$	$\mathbb{Z}$	0	0	0
C	0	-1	0	0	$\mathbb{Z}$	0	$\mathbb{Z}_2$	$\mathbb{Z}_2$	$\mathbb{Z}$	0	0
CI	1	-1	1	0	0	$\mathbb{Z}$	0	$\mathbb{Z}_2$	$\mathbb{Z}_2$	$\mathbb{Z}$	0

Table 2.9: The periodic table of topological insulators, adapted from [34], listed with respect to their Altland-Zirnbauer classification and the presence or absence of a time reversal (Θ), particle-hole (Ξ) or chiral (Π) symmetry. The right side of the table lists the type of the topological invariant, if any. The table repeats itself from d to $d+8$, in what is called the Bott periodicity [68].

an $N \times N$ irreducible Hermitian matrix. Other than the Hermiticity, there is no special symmetry. The time evolution operator for this Hamiltonian would be in the $U(N)$ unitary group. However, if the same Hamiltonian also had a time reversal symmetry, i.e. if it was in class AI, then in some basis, this Hamiltonian would be a real symmetric $N \times N$ matrix, putting the corresponding time evolution operator in the $U(N)/O(N)$ coset. Each of the classes in Table 2.9 has such an irreducible representation. These representations also correspond to some of the irreducible representations of the Cartan classification of symmetric spaces. For further details, we refer the reader to [27, 67, 68, 70, 71] and references therein.

We now briefly note without proof some of the interesting features of this table. One is that for any number of dimensions, there are always five classes that support nontrivial topological phases. The other is that there is a periodicity to this table; the top two rows alternate at every increase of the dimension, whereas the bottom eight rows get their list of four nontrivial cases pushed down by one. This also means, for any dimension $d > 8$, the column is the same as the column belonging to the dimension $d - 8$. This feature, shown by Kitaev [68],is called the *Bott periodicity*.

We finally list the Cartan classifications of various Hamiltonians we encountered or are going to encounter in this work. The integer quantum Hall effect Hamiltonians we considered in Appendix A feature magnetic fields that break time reversal symmetry, and there is neither chiral symmetry nor particle-hole symmetry, hence they are in Class A. Quantum spin Hall Hamiltonians in 2D, such as the one in Eq. 2.25, have TR symmetry with the eigenvalue of the involution being -1, placing them in class AII. A Kitaev chain

has only a particle-hole symmetry, therefore it is in class D; so is an *s*-wave topological superconductor in 1D. A 1D *p*-wave topological superconductor has both TRS and particle-hole symmetry, therefore it is in class BDI.

2.4. Obtaining Topological Invariants Using Transport Properties of 2D Topological Materials

The overview provided up to this point in this chapter involved homogeneous systems with $\mathbf{k}$ being a good quantum number; in fact, we used $\mathbf{k}$ mostly as the parameter of the Hamiltonian to classify its topological properties. We now focus on inhomogeneous systems where $\mathbf{k}$ is not necessarily a good quantum number, such as disordered systems.

In this subsection, we connect the transport properties of topological insulator or superconductor *wires* to their topological invariants (see Fulga *et al.* [69]). We do this by considering the symmetries of the *S*-matrix due to the discrete antiunitary symmetries of the Hamiltonian. We consider, for simplicity, a two-lead wire with identical leads (such as the one discussed in the next chapter, see Figure 3.1). The *S*-matrix relates the incoming modes from all leads into the system to the outgoing modes. It has the following form:

$$S = \begin{pmatrix} r & t' \\ t & r' \end{pmatrix}, \tag{2.48}$$

where r (r') is the reflection matrix from the left (right) lead onto itself and t (t') is the transmission from the left (right) lead into the right (left) lead. (For further information about *S*-matrices in transport, see Reference [72].)

One important point to make is that the classification and the periodic table 2.9 of the previous subsection is derived in the literature usually for closed systems; however, transport experiments and the devices that make use of these systems are usually open systems. Therefore, a classification given by the *S*-matrix is beneficial. Another important reason is that the *S*-matrix formulation allows us to understand the effects of disorder on these topological systems. The expectation is that a disordered system should retain its topological properties up to a certain point. However, we show in this thesis, disorder creates a much more complicated phase diagram in topological superconductor nanowires. We consider N-mode wires, hence the *S*-matrix is a $2N \times 2N$ unitary matrix and it is in one of the ten subspaces of the $U(2N)$ group. As mentioned above, five of these subspaces can support a topologically nontrivial phase; in 1D, they are the classes AIII, BDI, D, DIII and CII. We reproduce Table I of Fulga *et al.* (see Table 2.10) as a summary of the results. We note that in this thesis, we utilize the topological invariant obtained from the

	D	DII	BDI	AIII	CII
Phase	$\mathbb{Z}_2$	$\mathbb{Z}_2$	$\mathbb{Z}$	$\mathbb{Z}$	$\mathbb{Z}$
$\mathcal{C}$	$S = S^*$	$S = S^*$	$S = S^*$	0	$S = \Sigma_y S^* \Sigma_y$
$\mathcal{T}$	0	$S = 0 S^T$	$S = S^T$	0	$S = \Sigma_y S^T \Sigma_y$
$\mathcal{S}$	0	$S^2 = -1$	$S^2 = 1$	$S^2 = 1$	$S^2 = 1$
SR symmetry	0	0	1	1 or 0	0
r matrix	$r = r^*$	$r = r^* = -r^T$	$r = r^* = r^T$	$r = r^\dagger$	$r = r^\dagger = \Sigma_y r^T \Sigma_y$
$\mathcal{Q}$	$\mathrm{sgn}\det(r)$	$\mathrm{sgn}\,\mathrm{Pf}(ir)$	$\nu(r)$	$\nu(r)$	$1/2\nu(r)$

Table 2.10: The constraints on the S-matrix depending on the Altland-Zirnbauer class in 1D. Only topologically nontrivial phases are shown. The first row represents the AZ class, the second row gives the group of the topological phase, the third through fifth rows give the constraint on the S-matrix that the presence of the relevant antiunitary symmetry imposes (0 means the system does not have that symmetry). The SR symmetry row is for the presence or absence of the spin rotation symmetry in a given system. The second-to-last row gives all the constraints on the reflection matrix, whereas the last row shows how to obtain the topological quantum number $\mathcal{Q}$ from a given S (indeed, r) matrix. $\nu(r)$ is the number of negative eigenvalues of r. Adapted from [69].

S-matrix in a disordered wire for classes BDI and D in particular. We therefore follow Reference [69] and outline the proof for these two classes (see *ibid.* for the derivation of the topological invariants from *S*-matrix for the other classes).

For the 1D superconducting symmetry class D, we should get a $\mathbb{Z}_2$ invariant, counting the parity of the number $\mathcal{N}$ of Majorana bound states that exists at each end of the wire. Since the superconducting case has particle-hole symmetry, there are always even number of modes, so $N = 2M$ for $M \in \mathbb{Z}_+$. We take the topological invariant to be $\mathcal{Q} = \pm 1$. Fulga *et al.* consider a long but finite normal lead as shown in Figure 2.11. To have a bound state, $\mathrm{Det}(1 - r_N r_{NS}) = 0$ must hold, where r_N is the reflection from the terminated end of the normal lead and r_{NS} is the reflection matrix from the normal lead-superconductor interface. For class D, in the appropriate (electron-hole) basis, $r_N = \mathrm{diag}(U_N, U_N^*)$ where U_N is an $M \times M$ unitary matrix. The other end has a more general reflection matrix

$$r_{NS} = \begin{pmatrix} r_{ee} & r_{eh} \\ r_{he} & r_{hh} \end{pmatrix}, \tag{2.49}$$

where particle-hole symmetry gives $r_{ee}^* = r_{hh}$ and $r_{eh}^* = r_{he}$. A unitary transformation $r = U_{\text{Majorana}} r_{NS} U_{\text{Majorana}}^\dagger$ with

$$U_{\text{Majorana}} = \frac{1}{\sqrt{2}} \begin{pmatrix} 1 & 1 \\ -i & i \end{pmatrix} \tag{2.50}$$

yields a real r, where U_{Majorana} acting on the electron-hole space produces the Majorana basis. Noting that $-r_N$ becomes an orthogonal matrix O_N under the same transformation,

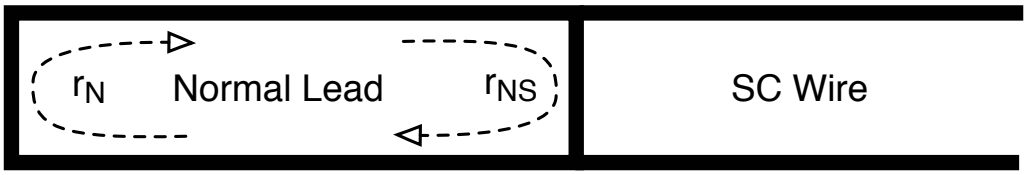

Figure 2.11: The wire and its ending considered by Fulga *et al.* [69] in their derivation of the topological numbers from the properties of the S-matrix.

the condition for Fermi level bound states become $\mathrm{Det}(1 + O_N r) = 0$. The number of bound states is therefore given by the number $\mathcal{N}$ of eigenvalues of $O_N r$ equal to -1. Other eigenvalues are either $+1$ or come in pairs of the form $e^{\pm i\phi}$. We therefore have $\mathrm{Det}(O_N r) = \mathrm{Det}(r) = \mathrm{Det}(r_{NS}) = (-1)^{\mathcal{N}}$, which is the invariant we are looking for [69].

For the chiral symmetry class BDI, the invariant is given by the negative eigenvalues of the reflection matrix r. We again terminate the wire so as to be able to talk about bound states, but we no longer strictly need a normal metal for termination, so the reflection matrix of the lead can be more general. In all of the chiral symmetry classes BDI, CII and AIII, the reflection matrices are Hermitian. We also assume that the wire is long enough that the transmission through it vanishes, making the reflection matrix have a determinant of 1., giving us a unitary matrix. Thus, it can be decomposed into a diagonal matrix $\mathcal{S}_{n_0} = \mathrm{diag}(1, \ldots 1, -1, \ldots, -1)$ with n_0 -1's and $N - n_0$ $+1$'s on the diagonal via a unitary transformation U_0. A similar transformation U_1 is also possible for r, giving $\mathcal{S}_{n_1}$ with n_1 eigenvalues equal to -1. We again search for the number of solutions $\mathcal{N}$ of $\mathrm{Det}(1 - r_0 r) = 0$. (When considering this number, we need to make sure to find the minimum possible $\mathcal{N}$ for any given unitary transformation for the decomposition; some cases may have accidental zero solutions that are not topologically protected and would move away from zero when the system is slightly changed, also changing the unitary transformation.) The condition for bound states now reads $\mathrm{Det}(1 - \mathcal{S}_{n_0} U_0^\dagger U_1 \mathcal{S}_{n_1} U_1^\dagger U_0) = 0$. We divide $U = U_0^\dagger U_1$ into four rectangular subblocks with the bottom right block being of size $n_0 \times n_1$. After some algebra, the bound state equation becomes:

$$\mathrm{Det} \begin{pmatrix} 0 & M_{N-n_0,n_1} \\ M_{n_0,N-n_1} & 0 \end{pmatrix} = 0, \tag{2.51}$$

where the matrix in the above equation is the matrix U with only its off-diagonal subblocks. As the matrices M_{mn} are not necessarily square, there are at least $|m - n|$ independent vectors (possibly accidentally more) for each M satisfying $Mv = 0$. Now, we use the fact that we have some leeway in choosing the termination and therefore r_0: We choose it so that all of its eigenvalues are -1. These two statements taken together show

there are in general $\mathcal{N} = \nu(r)$ solutions with negative eigenvalue leading to $\mathcal{Q} = \nu(r)$ for the BDI case [69].

Chapter 3

DISORDER-INDUCED TOPOLOGICAL TRANSITIONS IN MULTICHANNEL MAJORANA WIRES

In this chapter, we investigate topological properties of disordered multichannel hybrid structures proximity coupled to an *s*-wave superconductor with Rashba spin-orbit interaction (SOI) (RSW nanowires for short) and *p*-wave superconducting wires (PW wires). The usual expectation for these nanowires is that if their topological state is switched by modifying certain external parameters (such as gate potential or magnetic field), the spectral gap will close and open concomitantly with this transition. We show that for disordered nanowires, the closing and opening of a *transport* gap can cause further topological transitions, even in the presence of finite density of states (DOS), extending our earlier work on single channel wires [73] to multichannel wires. We derive analytical expressions for the boundaries of the topological phases of a disordered multichanneled RSW nanowire and find new topological regions in the phase diagram that show up as additional reentrant behavior in the experimentally relevant parameter regimes. In particular, new topological regions that show up in the low magnetic field limit, requires full description of all spin bands as shown by our analytical results (see Fig. 3.3). Hence, our results go beyond a simple *p*-wave description that requires a fully spin polarized wire. Finally we perform numerical simulations using a tight-binding (TB) approach and find very good agreement with our analytical formulae.

3.1. Introduction

Topologically nontrivial phases are exotic states of matter that have an electronic band gap in their bulk and protected gapless excitations at their boundaries [15, 22, 34]. Superconductors, being quasiparticle insulators, also feature topological phases with a quasiparticle gap in the bulk and excitations at their edges. For 1D systems, these edge states are fermionic zero-energy modes called Majorana states [16, 23, 43–45]. These states attracted intense attention owing to their non-Abelian nature, which led to proposals to use

them as topological qubits immune to decoherence [59, 60]. Although predicted to appear in exotic condensed matter systems with unconventional superconducting pairing [63, 74–78], recent proposals [55, 56, 61, 79] involving hybrid structures of more conventional materials have appeared. (Other proposals include References [57, 80–91].) This led to the recent conductance measurements done on a proximity coupled InSb nanowire [92], which showed possible evidence of Majorana end states in the form of zero bias conductance peaks. Other experiments reported further observations of zero bias peaks (ZBPs) in similar settings [93–97]. Very recently, scanning-tunneling spectroscopy experiments carried out on magnetic adatom chains on a conventional superconductor reported ZBPs at the ends of the chains. [58] While it is compelling to interpret the observation of these ZBPs as signatures of Majorana states, the issue is still under intense discussion. (Other sources of ZBPs include Kondo effect, weak anti-localization and disorder-induced level crossings, see, for example, References [96, 98–102].)

Semiconductor nanowire structures that are proximity-coupled to superconductors are technologically attractive platforms for Majorana physics. However, disorder has been prominently present in all such experimental samples to date. This led to a renewed interest in disordered superconducting wires, particularly focusing on the effects of disorder on Majorana states [50, 69, 73, 102–119]. These works focused mostly on disordered PW wires and showed that disorder is detrimental to the spectral gap as well as to the formation of Majorana fermions in both strictly 1D systems [73, 103, 104, 108, 114, 119] and in multichannel wires [50, 102, 115, 120]. In a recent study on the experimentally relevant RSW nanowire hybrid structures, some of us showed that disorder need not be detrimental to and in fact can even *create* topological order in strictly 1D wires [73]. We are not aware of a systematic study of the effects of disorder on the phase diagram of multichannel RSW nanowires.

In Majorana experiments, the subband spacing is typically considerably larger than the Zeeman splitting. For example, in InSb nanowires a subband spacing of order 15meV has been measured [121, 122] together with a g-factor of 40 to 58. Zero bias peaks that might signal Majorana fermions in these works are typically measured at magnetic fields from 0.1mT - 1T [92, 123] and exceptionally up to 2.5T. In all of these cases the Zeeman splitting remains smaller than the level spacing. Hence, one can argue that RSW nanowires are more experimentally relevant than PW nanowires, which require Zeeman splitting be much larger than level spacing.

This chapter is organized as follows: We begin the next section by specifying the system in question. We then derive the topological index in terms of the Lyapunov exponents and the effective superconducting length of the disordered multichannel RSW wire

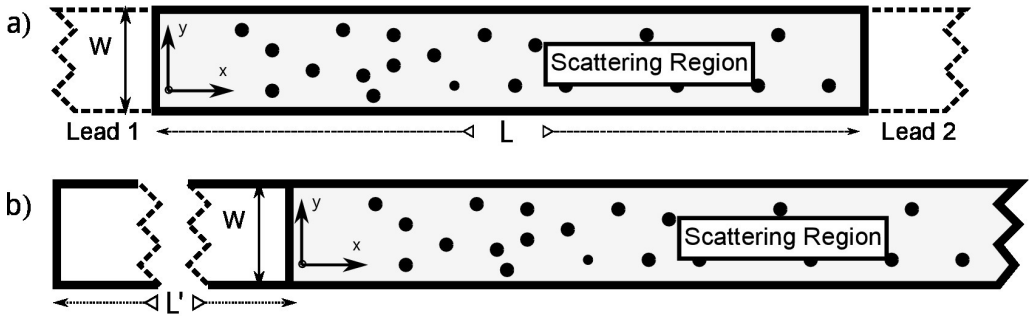

Figure 3.1: The multichanneled nanowire of width W, which is an RSW topological superconductor with a Gaussian disorder having an average value $\langle V \rangle = 0$. (a) In the leads, we take α_{SO}, Δ and $V(x, y)$ to be zero, making the leads metallic. Our analytical results assume a semi-infinite wire ($L \to \infty$), whereas in our numerical full tight-binding calculations we use wires of length $L \gg l_{\text{MFP}}, \xi, l_{\text{SO}}$. (b) The form of the wire used to construct the Majorana solutions in section 3.2.1. The part of the wire left of the scattering region is again metallic.

in subsection 3.2.1. In subsection 3.2.2, we analytically calculate this topological index using experimentally relevant system and transport parameters and compare our results with numerical tight-binding simulations. We then present our conclusions, finding that in disordered multichannel RSW nanowires with experimentally relevant parameters, the topological phase diagram is fragmented and previously unreported reentrant topologically nontrivial regions appear. In the Appendices, we detail the calculation of the mean free path of the system (Appendix C), detail our numerical simulations (Appendix D), present a full bandwith versions of our plots in the main text as opposed to the low energy region (Appendix E), and finally present our plots similar to the RSW system but produced for a *p*-wave nanowire with disorder, as system previously studied in literature, for completeness and comparison (Appendix F).

3.2. Topological Order in Disordered Multichannel Superconducting Nanowires

In this section, we investigate the topological properties of multichanneled topological superconductor nanowires. Such wires are experimentally realized by proximity coupling a semiconductor nanowire with Rashba spin-orbit interaction to an *s*-wave superconductor (RSW, see Fig. 3.1 (a)). The quasiparticles in RSW nanowires are described by the following Bogoliubov–de Gennes (BdG) Hamiltonian: [55, 56, 124]

$$H = \int \Psi^\dagger \, \mathcal{H}_{\text{BdG}} \, \Psi \, d\mathbf{r}$$
$$\mathcal{H}_{\text{BdG}} = \left(h_0 + \alpha_{\text{SO}}(\mathbf{p} \times \sigma)\right) \tau_z + B\sigma_x + \Delta\tau_x, \tag{3.1}$$

where $h_0 = \varepsilon(p) + V(\mathbf{r})$, $\Psi^\dagger = [\psi_\uparrow^\dagger, \psi_\downarrow^\dagger, \psi_\downarrow, -\psi_\uparrow]$ is the Nambu spinor with $\psi_{\uparrow(\downarrow)}$ being the destruction operator for an electron with spin up(down). The kinetic energy term $\varepsilon(p)$ is given by $\frac{\mathbf{p}^2}{2m} - \mu$ in a continuum system. We consider a 2D wire with $\mathbf{p} = (p_x, p_y)$. The

on-site potential is given by $V(\mathbf{r})$, μ is the chemical potential measured from the bottom of the band, $\alpha_{\rm SO}$ is the spin-orbit coupling (SOC) strength, Δ is the proximity-induced *s*-wave superconducting gap and B is the Zeeman field. The Pauli matrices σ_i (τ_i) act on the spin (electron-hole) space.

In the limit of large B, the wire is completely spin polarized. Then the low-energy quasiparticles are described by an effective *p*-wave Hamiltonian as discussed in previous literature [69, 73, 105–107, 109–111, 113–115, 119, 125]. For completeness, we discuss this limit in Appendix F.

The Hamiltonian in Eq. (3.1) is in the Altland-Zirnbauer (AZ) symmetry class D (*class D* for short) in two dimensions [67] with a topological number $Q_{\rm D} \in \mathbb{Z}_2$. In the absence of SOC along the y-direction, i.e. when the $\alpha_{\rm SO}\, p_y\, \sigma_x\tau_z$ term is set to zero, this Hamiltonian also possesses a chiral symmetry, placing it into AZ symmetry class BDI (*class BDI* for short) with an integer topological number $Q_{\rm BDI} \in \mathbb{Z}$ [115, 126]. In the thin wire limit, i.e. $W \ll l_{\rm SO}$, chiral symmetry breaking terms are $\mathcal{O}\left((W/l_{\rm SO})^2\right)$. Hence, the system in Eq. (3.1) has an approximate chiral symmetry [125–127]. We show in the next section that the class-BDI (chiral) topological number $Q_{\rm BDI} \in \mathbb{Z}$ and the class-D topological number are related as $Q_{\rm D} = (-1)^{Q_{\rm BDI}}$ (see Eq. (3.7)) [69].

3.2.1. Topological Index for a Disordered Multichannel *s*-wave Wire

To obtain the relevant topological index that counts the number of the Majorana end states for a RSW wire with disorder, we start with the BdG Hamiltonian $\mathcal{H}_{\rm BdG}$ in Eq. (3.1). Following Adagideli *et al.* [73], we perform the unitary transformation $\mathcal{H}_{\rm BdG} \to \mathcal{H}'_{\rm BdG} = \mathcal{U}^\dagger \mathcal{H}_{\rm BdG} \mathcal{U}$, where $\mathcal{U} = (1 + i\sigma_x)(1 + i\tau_x)\left[1 + \sigma_z + (1 - \sigma_z)\tau_x\right]/4$. Having thus rotated the Hamiltonian to the basis that off-diagonalizes its dominant part and leaves the small chiral symmetry breaking terms $\tau_z\sigma_z$ in the diagonal block, we obtain

$$\begin{aligned}\mathcal{H}'_{\rm BdG} = &-\tau_y\left(\sigma_z\, h_0 + \alpha_{\rm SO}\, p_x\right) + \tau_x\left(B\,\sigma_x + \Delta\right) \\ &+\ \tau_z\sigma_y\,\alpha_{\rm SO}\, p_y\,. \end{aligned} \tag{3.2}$$

We first set the chiral symmetry breaking term $\tau_z\,\sigma_y\,\alpha_{\rm SO}\,p_y$ to zero and focus on $E = 0$. The eigenvalue equation then decouples into the upper and lower spinor components. The solutions are of the form $\chi_+ = (\phi_+, 0)^T$ and $\chi_- = (0, \phi_-)^T$ where $\phi_\pm$ obey the following equation:

$$\left(\varepsilon(p)\sigma_z - i\,p_x\alpha_{\rm SO}\sigma_x \mp B \mp \Delta\sigma_x\right)\,\phi_\pm = 0. \tag{3.3}$$

Here, we have performed an additional rotation $\sigma_z \to \sigma_y$, $\sigma_y \to -\sigma_z$ and premultiplied

with $\pm\sigma_x$. We note that the operator acting on $\phi_\pm$ is not Hermitian.

We now perform a gauge transformation $\phi_\pm(x,y) \to e^{-\kappa_\alpha x}\phi_\pm(x,y)$ with a purely imaginary parameter $i\kappa_\alpha$. We take κ_α to be of first order in $\alpha_{\rm SO}$ and identify the following terms in the non-Hermitian operator in Eq. (3.3) in order of increasing power of $\alpha_{\rm SO}$:

$$\begin{aligned} H_0 &= h_0(p;x,y)\sigma_z \mp B \mp \Delta\sigma_x \\ H_1 &= \frac{i\hbar\kappa_\alpha p_x}{m}\sigma_z - i\alpha_{\rm SO}p_x\sigma_x \\ H_2 &= -\frac{\hbar^2\kappa_\alpha^2}{2m}\sigma_z + \hbar\alpha_{\rm SO}\kappa_\alpha\sigma_x, \end{aligned} \tag{3.4}$$

where we have indicated the (x,y) dependence of $h_0(p;x,y)$ through the potential $V(x,y)$. We absorb H_2 into H_0 by redefining μ and Δ. We now identify κ_α with the inverse of the effective superconducting length $\xi_{\rm eff}$, setting $\kappa_\alpha = \mp\xi_{\rm eff}^{-1} = \mp m\alpha_{\rm SO}\Delta/\hbar\epsilon$ with $\epsilon = \sqrt{B^2-\Delta^2}$. With this choice, $\{H_0, H_1\}_+ = 0$, which allows us to write the local solutions as follows:

$$\begin{aligned} \phi_\pm = \sum_n &\xi_\pm(\epsilon)\mathrm{e}^{\pm\kappa_\alpha x}\big(A_n f_n(x,y;\epsilon) + B_n g_n(x,y;\epsilon)\big) \\ &+ \xi_\pm(-\epsilon)\mathrm{e}^{\mp\kappa_\alpha x}\big(C_n f_n(x,y;-\epsilon) + D_n g_n(x,y;-\epsilon)\big), \end{aligned} \tag{3.5}$$

where $\xi_\pm(\epsilon)$ are the eigenvectors of $\epsilon\sigma_z \mp \Delta\sigma_x$ having an eigenvalue of $\pm|B|$ and f_n and g_n are the local solutions of the equation $h_0\psi = \epsilon\psi$. The presence of a multiple number of local solutions, which is the new aspect of the present problem, reflects the multichannel nature of the wire.

We then consider a semi-infinite wire ($x > 0$, $0 < y < W$) described by the Hamiltonian in Eq. (3.1) with Gaussian disorder. After going through the steps described above, we choose without loss of generality f_n to be the decaying and g_n the increasing function of x. We invoke a well known result from disordered multichannel normal state wires and express the asymptotic solutions as $f_n = e^{-\Lambda_n x}u_n(x,y)$ and $g_n = e^{\Lambda_n x}v_n(x,y)$ where $u_n(x,y), v_n(x,y)$ are $\mathcal{O}(1)$ functions as $x \to \infty$ and $\Lambda_n > 0$ are the *Lyapunov exponents* [69, 73, 113, 115, 128].

We now focus on a tight-binding system, where the number of Lyapunov exponents $N_{\rm max}$ is finite. (In the continuum limit, we have $N_{\rm max} \to \infty$.) For the boundary conditions at $x = 0$, we first extend the hardwall back to $x = -L'$ with L' a small value, and consider a normal metal in the strip $-L' < x < 0$ and $0 < y < W$ (see Figure 3.1 (b); in Eq. (3.1), $\alpha_{\rm SO} = 0$, $\Delta = 0$, $V(x,y) = 0$). The hardwall boundary condition at $x = -L'$ can be expressed as $\underline{\underline{R}} \cdot \underline{b}_+ = \underline{b}_-$ with $\underline{b}_+ \equiv (\ldots, A_n, C_n, \ldots)^T$, $\underline{b}_- \equiv (\ldots, B_n, D_n, \ldots)^T$ and $\underline{\underline{R}}$ as the extended reflection matrix [129]. We therefore have $2N_{\rm max}$ boundary conditions,

leaving $2N_{\text{max}}$ of the $4N_{\text{max}}$ parameters undetermined.

The boundary conditions at $x \to \infty$ require that $\phi_\pm$ have only exponentially decaying solutions. We focus on the $B > \Delta$ case, yielding real κ_α and ϵ. (As discussed in References [79] and [56], the $B < \Delta$ case yields no solutions.) We take $\kappa_\alpha > 0$ for definiteness. (The following arguments can be extended trivially to the $\kappa_\alpha < 0$ case.) The exponential asymptotic factors in the solutions contain a factor of $e^{\pm\kappa_\alpha x}$ in various sign combinations, affecting the overall convergence at $x \to \infty$. In particular, the solutions ϕ_+ have exponential factors of $e^{(\kappa_\alpha - \lambda_n(\epsilon))x}$, $e^{(\kappa_\alpha + \lambda_n(\epsilon))x}$, $e^{(-\kappa_\alpha - \lambda_n(-\epsilon))x}$ and $e^{(-\kappa_\alpha + \lambda_n(-\epsilon))x}$, whereas the ϕ_- solutions have the same form of exponential factors with the sign of κ_α switched. For $|\kappa_\alpha|$ smaller than all Lyapunov exponents, all B_n and D_n are set to zero as they would represent diverging solutions at $x \to \infty$. There are therefore $2N_{\text{max}}$ more conditions , bringing the total up to $4N_{\text{max}}$, to determine a total of $4N_{\text{max}}$ parameters, yielding only accidental solutions. However, for a given $n = n_*$, if $\min\left(\lambda_{n_*}(\epsilon), \lambda_{n_*}(-\epsilon)\right) < \kappa_\alpha < \max\left(\lambda_{n_*}(\epsilon), \lambda_{n_*}(-\epsilon)\right)$, there are three growing solutions for one of the $\phi_\pm$ sectors and only one for the other sector. (If $\lambda_{n_*}(\epsilon) < \lambda_{n_*}(-\epsilon)$, the ϕ_+ sector has the three growing solutions and vice versa.) The sector with three growing solutions thus has the number of boundary conditions increased by one and the other sector has the number of boundary conditions decreased by one. If any sector has more than $4N_{\text{max}}$ boundary conditions in total, then there are no solutions for that sector. Therefore, the BDI topological number $Q_{\text{BDI}} \in \mathbb{Z}$ is given by the number of free parameters, which is equal to $4N_{\text{max}}$ minus the total number of equations arising from the boundary condition at $x = -L'$. We obtain:

$$\begin{aligned} Q_{\text{BDI}} = &\sum_n \Theta\left(\xi_{\text{eff}}^{-1} - \Lambda_n(\epsilon)\right)\, \Theta\left(\Lambda_n(-\epsilon) - \xi_{\text{eff}}^{-1}\right) \\ &- \sum_n \Theta\left(\xi_{\text{eff}}^{-1} - \Lambda_n(-\epsilon)\right)\, \Theta\left(\Lambda_n(\epsilon) - \xi_{\text{eff}}^{-1}\right). \end{aligned} \tag{3.6}$$

We see that each Lyapunov exponent pair $\Lambda_n(\pm\epsilon)$ contributes a topological charge $Q_{\text{BDI}}^{(n)}$ to the overall topological charge. Hence $Q_{\text{BDI}} = \sum_n Q_{\text{BDI}}^{(n)}$, where

$$Q_{\text{BDI}}^{(n)} = \begin{cases} +1 & \text{if } \Lambda_n(-\epsilon) > \xi_{\text{eff}}^{-1} > \Lambda_n(\epsilon) \\ -1 & \text{if } \Lambda_n(-\epsilon) < \xi_{\text{eff}}^{-1} < \Lambda_n(\epsilon) \\ 0 & \text{otherwise.} \end{cases}$$

We thus generalize the results of Ref. [73] to a multichannel RSW wire. We note, however, that the total number of Majorana end states for a multichannel RSW wire in class BDI, given by $|Q_{\text{BDI}}|$, is not equal to sum of the Majorana states per Lyapunov exponent

pair, i.e. $|Q_{\rm BDI}| \neq \sum_n |Q^{(n)}_{\rm BDI}|$.

We now consider the full Hamiltonian in Eq. (3.1) with the chiral symmetry breaking term included. This Hamiltonian in two dimensions is in class D and only approximately in class BDI. The chiral symmetry breaking term pairwise hybridizes the Majorana states described above, moving them away from zero energy. However, because of the particle-hole symmetry in the topological superconductor, any disturbance or any perturbation that is higher order in $\alpha_{\rm SO}$ can only move the solutions away from zero energy eigenvalue in pairs; i.e. for any solution moving away from zero eigenvalue towards a positive value, a matching solution must move to a negative eigenvalue. Therefore, the number of zero eigenvalue solutions changes in pairs. Hence, the parity does not change. The parity changes, however, every time one of the Lyapunov exponents passes through the value of $\xi_{\rm eff}^{-1}$. We therefore arrive at the class D topological index $Q_{\rm D} = (-1)^{Q_{\rm BDI}}$ as [69]

$$Q_{\rm D} = \prod_{n,\pm} \mathrm{sgn}\big(\Lambda_n(\pm\epsilon)\,\xi_{\rm eff} - 1\big), \tag{3.7}$$

indicating that there is a class D Majorana solution at zero energy ($Q_{\rm D} = -1$) if there are an odd number of BDI Majorana states per edge. Therefore, for the topological state of the RSW wire to change from trivial to nontrivial or vice versa, it is necessary and sufficient to have $Q_{\rm BDI}$ described in Eq. (3.6) change by one. The above equation thus constitutes the multichannel generalization of Eq.(7) of Ref. [73].

To calculate the topological index $Q_{\rm D}$ in Eq. (3.7), we relate the Lyapunov exponents in Eq. (3.6) to transport properties, namely the mean free path, of a disordered wire. We first note that as $L \to \infty$, the Lyapunov exponents Λ_n are self-averaging, with a mean value $\bar{\Lambda}_n$ given by

$$\bar{\Lambda}_n(\mu_{\rm eff}) = \frac{n}{(\bar{N}(\mu_{\rm eff}) + 1)\, l_{\rm MFP}} \tag{3.8}$$

where $\mu_{\rm eff} = \mu \pm \epsilon$, $\bar{N}(\mu_{\rm eff}) = \lfloor W k_F(\mu_{\rm eff})/\pi \rfloor$, $k_F = \sqrt{2m\mu_{\rm eff}/\hbar^2}$, $n \in 1 \ldots \bar{N}(\mu_{\rm eff})$ and $l_{\rm MFP}$ is the MFP of the disordered wire [128]. We use Fermi's Golden Rule to approximate the mean free path $l_{\rm MFP}$ by calculating the lifetime of a momentum state and multiplying it with the Fermi speed. We obtain, for a quadratic dispersion relation $\varepsilon(p) = p^2/2m - \mu$,

$$l^{-1}_{\rm MFP} = \frac{4m^2\gamma}{\hbar^4 \pi k_F}\, \zeta_N^{-1}, \tag{3.9}$$

where ζ_N^{-1} is a dimensionless number whose detailed form is given in Eq. (C.5) (see Appendix C for details).

In order to compare our numerical tight-binding results with the analytical results obtained through Eq. (3.7) and (3.6), we also calculate the mean free path $l^{\rm TB}_{\rm MFP}$ for a tight-

binding (TB) dispersion relation $\varepsilon(k_{x,n}) = 2t\ (2 - \cos(k_{x,n}a) - \cos(n\pi a/W))$, where t is the hopping parameter, a is the lattice parameter for the TB lattice, W is the width of the lattice and $k_{x,n}$ is defined through $k_{x,n}^2 + k_{y,n}^2 = k_F^2$ with $k_{y,n} = n\pi/W$. We obtain

$$(l_{\text{MFP}}^{\text{TB}})^{-1} = \frac{\gamma}{\bar{N}^{\text{TB}} W a^2 t^2} (\zeta_N^{\text{TB}})^{-1}, \tag{3.10}$$

where $\bar{N}^{\text{TB}}$ is given by

$$\bar{N}^{\text{TB}} = \begin{cases} \lfloor (W/\pi a) \arccos(1 - \varepsilon/2t) \rfloor, & \text{for } 0 < \varepsilon < 4t, \\ \lfloor (W/\pi a) \arccos(1 - (4 - \varepsilon/2t)) \rfloor, & \text{for } 4t < \varepsilon < 8t. \end{cases}$$

The details of the calculation and the dimensionless constant ζ_N^{TB} are again found in Appendix C.

The topological phase boundaries, shown in Figures 3.2 and 3.3 as the bold black lines, are calculated by equating ξ^{-1} to Λ_n obtained from Eq. (3.8) and (3.10). We thus obtain the critical field B^* at which the system goes through a topological phase transition via thie following implicit equation:

$$B^* = \Delta \sqrt{\beta\, \Gamma_n^{\text{TB}} (\mu_{\text{eff}}(B^*)) + 1} \tag{3.11}$$

where $\beta = (W a^2 t^2/\gamma l_{\text{SO}})^2$, $\mu_{\text{eff}}(B^*) = \mu \pm \sqrt{(B^*)^2 + \Delta^2}$ and

$$\Gamma_n^{\text{TB}}(\mu_{\text{eff}}) = \left(\frac{\bar{N}^{\text{TB}}(\mu_{\text{eff}})}{n} \right)^2 \times \left(\zeta_N^{\text{TB}}(\mu_{\text{eff}}) \right)^2 \left(\bar{N}^{\text{TB}}(\mu_{\text{eff}}) + 1 \right)^2.$$

Equation (3.11) constitutes the central finding of this chapter. It is an analytical expression that determines all topological phase boundaries of a multichannel disordered wire.

An experimentally interesting point is the largest values of various system parameters that allow a topological transition. Using Equations (3.6) and (3.7), we estimate the upper critical field $B^*|_\gamma$, i.e. the minimum value of B above which the system is always in a topologically trivial state at a given disorder strength γ, as

$$B^*|_\gamma \sim \Delta \frac{l_{\text{tr}}^{\max}}{l_{\text{SO}}}, \tag{3.12}$$

where $l_{\text{tr}}^{\max} = \max(\{\Lambda_n^{-1}\})$ is the maximum localization length achievable in the system. For a fixed nonzero disorder, $B^*|_{\gamma>0}$ is infinite for a continuum system as the localization length increases indefinitely with increasing Fermi energy. For a TB system, the upper critical field $B^*|_{\gamma>0}$ is finite because the localization length is bounded in TB systems. For a clean wire, $B^*|_{\gamma=0}$ is infinite for both the TB and the continuum models.

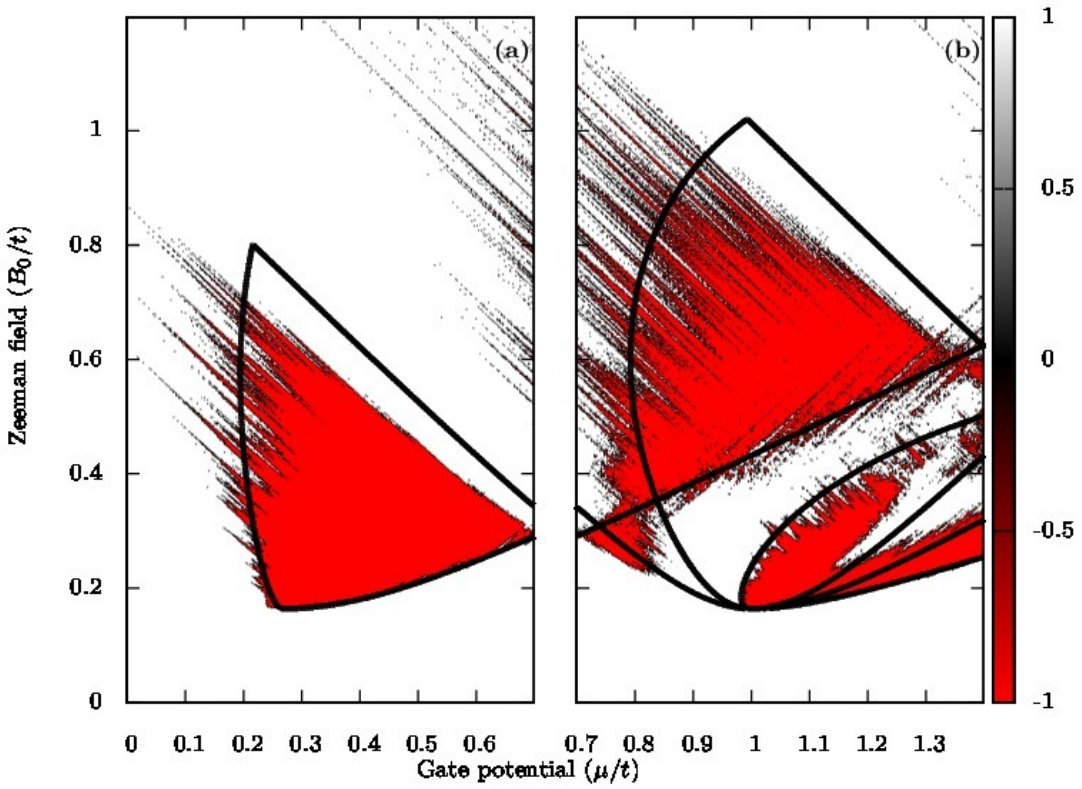

Figure 3.2: μ vs. B vs. Q_{D} for a five-channel system (compare with Figs. E.4 and E.3.) The background red-white colors are obtained using a numerical tight-binding simulation with $L = 30000a$ and $W = 5a$, while the black lines, which represent the topological phase boundaries, are obtained analytically using Eq. (3.7). Here, $V_0 = \sqrt{\gamma/a^2} = 0.2t$, $\alpha_{\mathrm{SO}} = 0.02\hbar/ma$ ($l_{\mathrm{SO}} = 4.08\mu m$) and $\Delta = 0.164t$, where $t = \hbar^2/2ma^2$ and $a = 0.01 l_{\mathrm{SO}}$ is the tight-binding lattice spacing. The fragmented nature of the topological phase diagram seen in (b) cannot be explained in a p-wave picture. See Appendix D for a discussion of corresponding experimental parameters.

3.2.2. Numerical Simulations

In this section, we obtain the topological index of a disordered multichannel wire numerically and compare it with our analytical results from the previous section. For our numerical simulations, we take the TB form of the Hamiltonian in Eq. (3.1) whose details can be found in the Appendix D. We consider a wire of length $L \gg l_{\mathrm{MFP}}$, ξ or $_{\mathrm{SO}}$, with metallic leads ($\alpha_{\mathrm{SO}} = 0$, $\Delta = 0$ and $V(x, y) = 0$ in the leads). We use the results of Fulga *et al.* to obtain the topological quantum number of the disordered multichannel wire from the scattering matrices of the wires [69]. For a semi-infinite wire in the symmetry class D, the topological charge is given by $Q_{\mathrm{D}} = \det(r)$ in terms of the reflection matrix r. For a quasiparticle insulator, this determinant can only take the values ± 1. However, for a finite system this determinant can in general have any value in the $[-1, 1]$ interval. We obtain the reflection matrix of the TB system in our numerical TB simulations using the

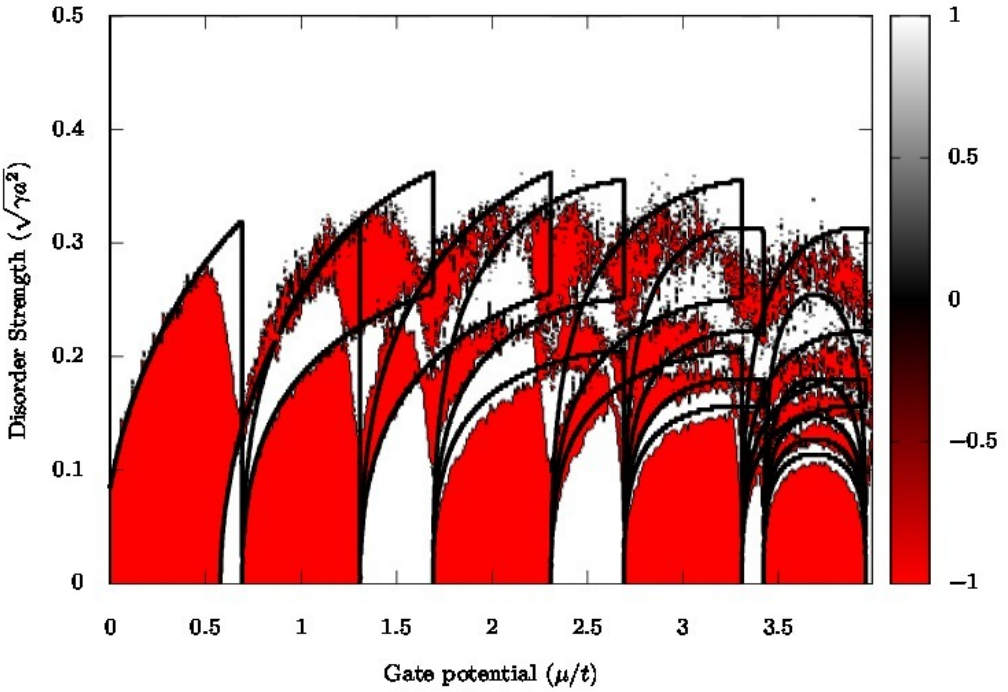

Figure 3.3: μ vs. $V_0 = \sqrt{\gamma/a^2}$ vs. Q for a multichannel RSW wire. The black lines, which represent topological phase boundaries, are obtained analytically using Eq. (3.7). The background red-white colors are obtained using tight-binding numerical simulations with $L = 60000a$. In both cases, $W = 4a$, $\alpha_{\rm SO} = 0.015\hbar/ma$, $\Delta = 0.20t$ and $B = 0.35t$, where $t = \hbar^2/2ma^2$ is the tight-binding hopping parameter and a is the TB lattice spacing. See Appendix D for a discussion of corresponding experimental parameters.

Kwant library [130] and then use this relation to calculate Q_{D}. We plot the topological phase diagram in Figures 3.2 and 3.3, where the red and white colors represent $Q_{\mathrm{D}} = -1$ and $Q_{\mathrm{D}} = +1$ respectively.

Figure 3.2 exemplifies our central result given in Eq. (3.11). We find that for a nearly depleted wire (Fig. 3.2a), the topological phase merely shifts to the higher values of the chemical potential in agreement with Ref. [73]. For higher chemical potentials/doping, we observe a fragmented topological phase diagram (Fig. 3.2b). We find good agreement with our analytical results from Eq. (3.11). We note in passing that, this fragmentation cannot be explained by a simple *p*-wave picture as these topological phases arise despite the incomplete spin-polarization of the wire under a low magnetic field. For a full phase diagram over the entire bandwidth, but for slightly different material parameters, see Figure E.4, where the reentrant phases are apparent.

In Fig. 3.3, we plot the topological number Q_{D} as a function of the disorder strength $\sqrt{\gamma/a^2}$ and μ, for a constant B_{Zeeman} over the full TB bandwidth. The reentrant nature of the topological phase diagram can also be seen in this plot, for example, by following the $\mu = 1.5$ line as γ is increased. As the disorder strength increases, series of topological transitions occur, similar to the PW wire [115]. However, unlike the PW wire, the number of transitions is given by $\bar{N}(\mu + \epsilon) + \bar{N}(\mu - \epsilon)$ rather than $\bar{N}(\mu)$, with $\bar{N}(\mu)$ defined as $\bar{N}(\mu_{\mathrm{eff}}) = \lfloor W k_F(\mu_{\mathrm{eff}})/\pi \rfloor$. For further discussion of the emergence of effective p-wave picture at high magnetic fields, see Appendix E.

3.3. Conclusion

In summary, we investigate the effect of disorder in multichannel Rashba SOC proximity-induced topological superconductor nanowires (RSW nanowires) at experimentally relevant parameter ranges. We derive formulae that determine all topological phase boundaries of a multichannel disordered RSW wire. We test these formulae with numerical tight-binding simulations at experimentally relevant parameter ranges and find good agreement without any fitting parameters. We show that there are additional topological transitions for the RSW wires leading to a richer phase diagram with further fragmentation beyond that of the *p*-wave models.

Chapter 4

CAN ONE HEAR THE SHAPE OF A TOPOLOGICAL CROSSING?

In this chapter, we study the statistics of the level-crossings between even and odd fermion parity levels in disordered or chaotic ballistic superconductor nanostructures at the Fermi energy as a function of external parameters such as the magnetic field B or the chemical potential μ. Such crossings that signal a change in the ground state fermion parity, are regarded to be precursors of Majorana fermions (MFs) that appear in the long-wire geometry. Hence, they became the focus of recent attention [70, 97, 98, 131–138]. We first obtain formulae for the average parity crossing density. Next, we find that the fluctuations in these systems also follow universal statistics that may be either Gaussian orthogonal, Poissonian or sub-Poissonian, depending on the underlying scattering details as well as the geometry of the sample. Our results thus extend the results of Ref. [131] to more realistic wires and dot geometries. We also find that the parity crossing points are described by the normal-state properties of the system. We finally discuss under what conditions these crossings signal MFs.

4.1. Weyl Expansion

From 1911 to 1915, Hermann Weyl studied the spectra of wave equations in finite systems for various boundary conditions. (For a collection of his work, see Reference [139].) For sufficiently non-problematic boundaries, the wave equation has an infinite number of real nonnegative solutions. Weyl considered the problem of the distribution of real eigenvalues for large eigenvalues: How does the number of eigenvalues that are smaller then λ_{max} behave asymptotically as $\lambda_{\text{max}} \to \infty$? Equivalently, what is the asymptotic form of the average distance between eigenvalues, called the *level spacing* of the Laplace operator (or its generalized N-dimensional form) for generic boundary shapes? These shapes can be formed out of shapes that feature chaotic dynamics in the classical limit or out of a system with fixed shape with different disorder realizations. Weyl showed that for a wave equation $\nabla^2\psi + k^2\psi = 0$, as $k \to \infty$, the number of eigenvalues $N(k)$ below k depends

only on the volume (or area on 2D) of the system for any shape for either Dirichlet or Neumann boundary conditions, *to zeroth order* [140]. His result was:

$$\begin{aligned} N_0(k) &= l\,\frac{k}{\pi} && d=1 \\ N_0(k) &= A\,\frac{k^2}{4\pi} && d=2 \\ N_0(k) &= V\,\frac{k^3}{6\pi^2} && d=3 \end{aligned} \tag{4.1}$$

where A, V are the area and volume, respectively. Note that the derivative of these results would give the density of states. The problem of the statistical distribution of real eigenvalues and its generalizations, and higher order corrections are well studied, we refer the reader to Reference [140] for further details. Focusing on the the smooth part of the density of states, the result for either Dirichlet of Neumann boundary conditions is

$$\rho(E) \simeq \frac{Vk}{4\pi^2} \mp \frac{S}{16\pi} + \frac{1}{12\pi^2 k}\int_{\partial V} d\sigma \frac{1}{2}\left(\frac{1}{R_1}+\frac{1}{R_2}\right), \tag{4.2}$$

where S is the surface area, ∂V is the boundary of the system and R_i are the two main radii of curvature of the boundary at the point of integration in the integrand. The upper (lower) sign in front of the surface term corresponds to the Dirichlet (Neumann) boundary conditions [141, 142]. Balian and Bloch generalized this result to mixed boundary conditions using multiple reflection expansion of the Green's function of the system [143]. Such expansions of the smooth density of states in terms of a volume term, a surface term, a curvature term, and an Euler characteristics term (see Eq. 2.1), valid for high wavenumbers (short wavelengths), are called *Weyl expansions*. These show that the spectra of finite systems can be related to their shape in the short wave-length limit. The remaining correction, namely the density of states fluctuations and its correlations will sensitively depend on whether the corresponding classical dynamics is chaotic or integrable as well as the type of scattering that is featured in the system.

4.2. Universal Level Spacing Statistics

While working on energy levels of neutrons in highly excited nuclei, Wigner considered the statistical distribution of eigenenergies. He assumed that the fluctuations in the system would randomize the Hamiltonian [144], and hence considered an ensemble of random Hamiltonians with the only conditions that (i) the ensemble members should be Hermitian (corresponding to a unitary time evolution), (ii) that if there are fundamental symmetries of the system, the Hamiltonians should obey those symmetries, and (iii) how one constructs the Hamiltonians should have no further constraints, leading to an ensem-

ble of Hamiltonians in which all of their matrix elements were independent (up to the system symmetries) and random. Dyson used this work and he formulated "the threefold way" [145], in which he considered whether a system has time reversal symmetry or spin rotation symmetry (for Hamiltonians that have spin degrees of freedom), he classified the Hamiltonians into three classes: If the system has none of these symmetries, the Hamiltonians are just Hermitian, and belong to the Gaussian Unitary Ensemble (GUE). If they have time reversal symmetry but no spin degrees of freedom (or they have spin rotational invariance), they are real symmetric, belonging to the Gaussian Orthogonal Ensemble (GOE). If they have time reversal symmetry, have spin degrees of freedom, and spin rotation invariance is broken, they are in the Gaussian Symplectic Ensemble (GSE) and are real quaternions. (The tenfold way of subsection 2.3.1 is a direct generalization of this classification.) Each of these ensembles have a Gaussian probability distribution for the Hamiltonian H, given by

$$P_{N,\beta}(H) = \mathcal{N}_{N,\beta} e^{-\frac{\mathrm{Tr}(H^2)}{2\sigma^2}} dH. \tag{4.3}$$

Here, N is the size of the matrix and the *Dyson parameter* β counting the number of real numbers required to define a single element of the Hamiltonian matrix (1 for GOE, 2 for GUE and 4 for GSE). The parameter σ determines the width of the probability distribution. (It turns out that spectral correlations are independent of this width as $N \to \infty$ away from the edge of the spectrum [128].) The difference between the ensembles are given by their measures, which must reflect the number of independent parameters: $dH = \prod_{i<j} dH_{ij}$ for GOE, $dH = \prod_i dH_{ii} \prod_{i<j} \mathrm{Re}\, dH_{ij} \,\mathrm{Im}\, dH_{ij}$, etc. The original problem of Weyl, in this context, now can be considered as: Given the above distributions for the Hamiltonians, what are the distributions for eigenenergies? (For a review, see, for example [146]. This problem can also be generalized to transport and localization problems where now it is the scattering matrices that are random [128].)

The Wigner-Dyson statistics are the eigenvalue statistics of random matrices, modeled with completely independent entries. However, Bohigas, Giannoni and Schmit (BGS) conjectured [147–149] that the eigenvalue statistics of quantum systems that are chaotic in the classical limit, which have some correlation in the matrix elements and thus show signs of level repulsion, can also be described by the same statistics. There is now a whole body of numerical and analytical work supporting this conjecture (see, for example, [128, 150–152] and references therein). In a system where all unitary symmetries are completely broken, such as in the case of a chaotic system, the level-spacing distribution thus becomes universal, reflecting the presence or absence of antiunitary symmetries as well as the dimensionality.

4.3. Parity Crossing Statistics for a Topological Superconductor

The ground state in most superconductors have an even number of electrons (sometimes called "even parity"), reflecting their completely paired nature. However, under certain conditions the even electron-numbered state can cross an odd electron-numbered (odd parity) state, changing the ground state parity. This symmetry, called the fermion parity, ensures that no level repulsion can take place. While well known within the context of Josephson junctions [131], these crossings have attracted recent attention as they are the zero dimensional topological phase transitions in which two Majorana fermions appear exactly at the transition point. There are also works that regard such crossings to be signatures of the presence of a pair of Majorana states in clean one dimensional wires [153–155].

In this section, we extend the Weyl expansion as well as level distributions from its usual context of energy eigenvalues to chemical potential (or magnetic field) values where ground state parity changes, essentially tying the parity crossings to the shape of the system. Alluding to Kac's famous paper [156], we thus "can hear the shape of a series topological transitions." We will also discuss how the parity-crossings in a finite one-dimensional wire are related to the wire being in the topological phase.

We start by considering the parity crossings in an arbitrarily shaped p-wave cavity. Such a cavity is naturally formed if a Rashba SOI coupled semiconductor wire/cavity under an applied magnetic field is brought into contact with a conventional superconductor. While the latter system is effectively described by the former, there are certain crucial aspects missed by the effective p-wave model, such as those mentioned in the previous chapter, or the subtle difference between the counting method of the endpoint Majorana states before hybridizing), hence we will consider the more realistic semiconductor model separately to account for these differences (see Eq. 3.6 and the surrounding discussion).

Our starting point is the p-wave Hamiltonian:

$$H_p = \begin{pmatrix} \frac{p^2}{2m} + V(\mathbf{x}) - \mu & \Delta'(p_x - ip_y) \\ \Delta'(p_x + ip_y) & -\frac{p^2}{2m} - V(\mathbf{x}) + \mu \end{pmatrix}, \tag{4.4}$$

where μ is the chemical potential, $V(\mathbf{x})$ is the on-site potentialincluding disorder and confinement potentials. Crossing points are chemical potential values for which the above Hamiltonian has eigenfunctions of zero energy, i.e. $H_p\chi = 0$, pre-multiplying this equation with τ_3, we cast the problem as a (non-Hermitian) eigenvalue problem:

$$\Big(\frac{1}{2m}\big(\mathbf{p} + im\Delta'\boldsymbol{\eta}\big)^2 - \frac{m}{2}\Delta'^2 - V(\mathbf{x})\Big)\chi = \mu\chi. \tag{4.5}$$

We identify this operator as the Hamiltonian of a Rashba 2DEG with an imaginary Rashba parameter $\alpha = i\Delta'$. While there is no reason that a particular eigenvalue is real, those that are real correspond to the values of the crossing points, while the complex eigenvalues are associated with avoided crossings.

We now show that, in the experimentally relevant limit of $W \ll \xi$, almost all eigenvalues of this operator are real. Rescaling the eigenfunction $\chi = \mathrm{e}^{\boldsymbol{\eta}\cdot\mathbf{x}/\xi - x^2/\xi^2}\tilde{\chi}$, expanding in powers of W/ξ, we obtain:

$$\Big(\frac{1}{2m}(\mathbf{p} + \tau_3 m^2 \xi^{-2}(\mathbf{z}\times\mathbf{x}))^2 + V(x) - \frac{\Delta'^2}{2m}\Big)\tilde{\chi} = \mu\tilde{\chi}. \tag{4.6}$$

We thus see that the crossing points are eigenvalues of the normal state Hamiltonian with a fictitious magnetic field $\pm m^2/e\xi^2$ and constant potential shift $-\Delta'^2/2m$. Note that, the energy levels are even functions of applied magnetic fields, therefore to the order we are working, the effect of the fictitious magnetic field on the crossing points can be ignored. We thus arrive at the rather surprising result that the values of all crossing points are simply energy eigenvalues of the normal state (see Fig. 4.1).

This identification allows us to obtain the average and statistics of parity crossings. For the mean level spacing, we invoke the Weyl expansion to obtain:

$$\Delta\mu = \begin{cases} \frac{2\pi\sqrt{\mu}}{L} & \text{if } d = 1 \\ \frac{4\pi}{S} & \text{if } d = 2 \\ \frac{4\pi^2}{V\sqrt{\mu}} & \text{if } d = 3. \end{cases} \tag{4.7}$$

4.4. Deviation from the Weyl Expansion

The deviations from the average behavior obtained above depends on whether the underlying system is regular, diffusive, chaotic or localized. For energy spacings smaller than the Thouless energy, these deviations are universal and are described by an ensemble of real Hermitian random matrices, namely the orthogonal ensemble. The corresponding distribution of crossing spacings is given by the Wigner-Dyson distribution. Hence, the probability density P of finding a crossing spacing of $\delta\mu$ is:

$$P(\delta\mu) = \frac{\pi\delta\mu}{2\Delta\mu}\exp\big(-\pi\delta\mu^2/4\Delta\mu^2\big). \tag{4.8}$$

When the mean crossing spacing is much bigger than the Thouless energy, the normal state is localized and the level spacing distribution is Poissonian (this is also true for

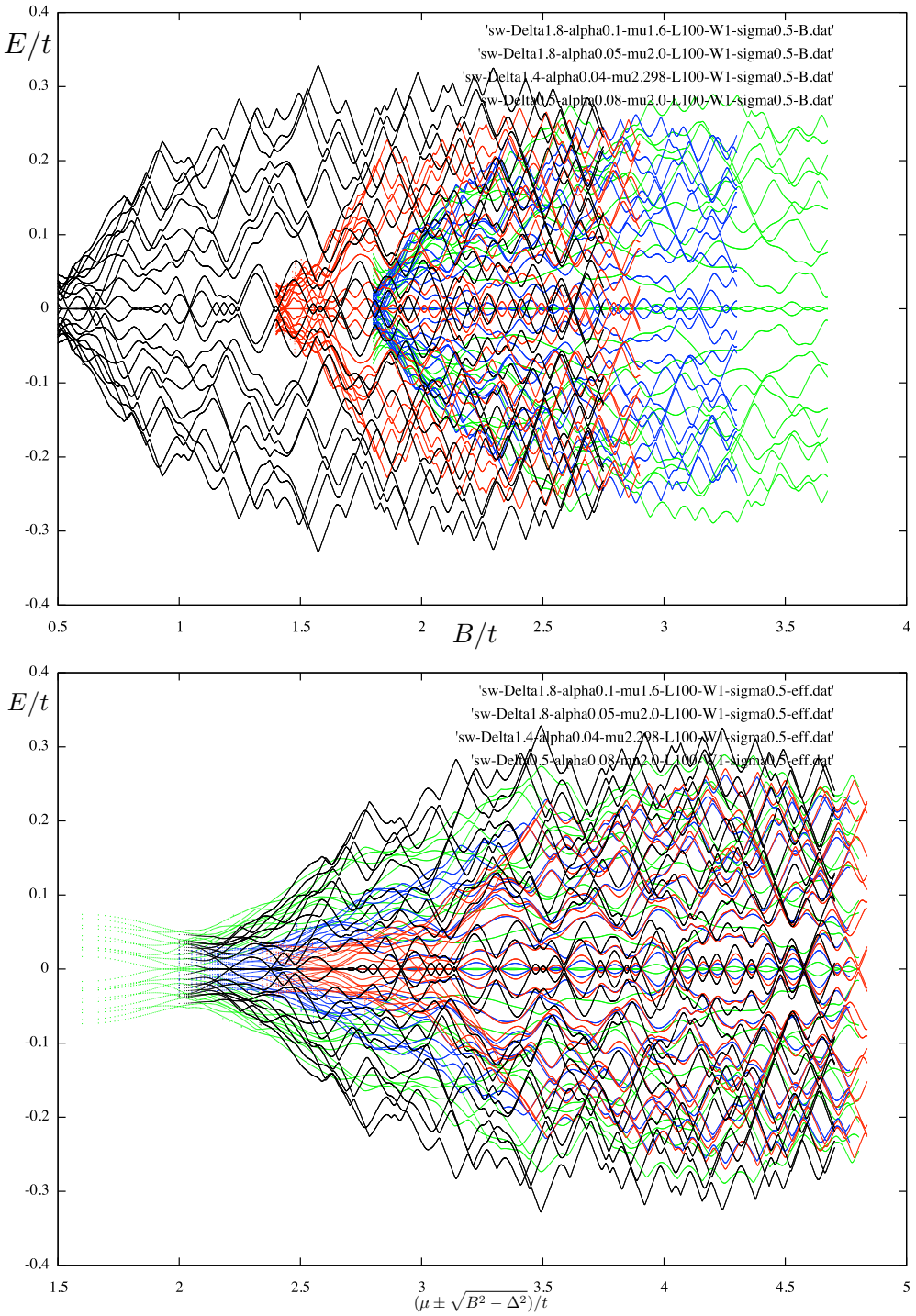

Figure 4.1: A plot of the lowest ten eigenvalues of the disordered s-wave Hamiltonian in Eq. 4.11, discretized on a 1D lattice of 100 sites, plotted as a function of (a) B/t and (b) $\sqrt{B^2-\Delta^2}/t$, for different values of Hamiltonian parameters. In both plots, the black set of curves represents the lowest ten eigenvalues obtained for $\Delta = 0.5t$, $\alpha = 0.08ta$, $\mu = 2.0t$; the red set is for $\Delta = 1.4t$, $\alpha = 0.04ta$, $\mu = 2.298t$; the green set is for $\Delta = 1.8t$, $\alpha = 0.05t$, $\mu = 2.0t$; and the blue set is for $\Delta = 1.8t$, $\alpha = 0.1ta$, $\mu = 1.6t$. Here, $t = \hbar^2/2ma^2$ is the hopping parameter. In all cases, the disorder strength is the same. Of interest is the statistics of each eigenvalue crossing the zero point. (Particle-hole symmetry assures another state will cross zero at the same point; level repulsion does not occur because of this symmetry.) Note that when the same plot in (a) is plotted as a function of $\sqrt{B^2-\Delta^2}$, all crossings happen at the same points for all parameters.

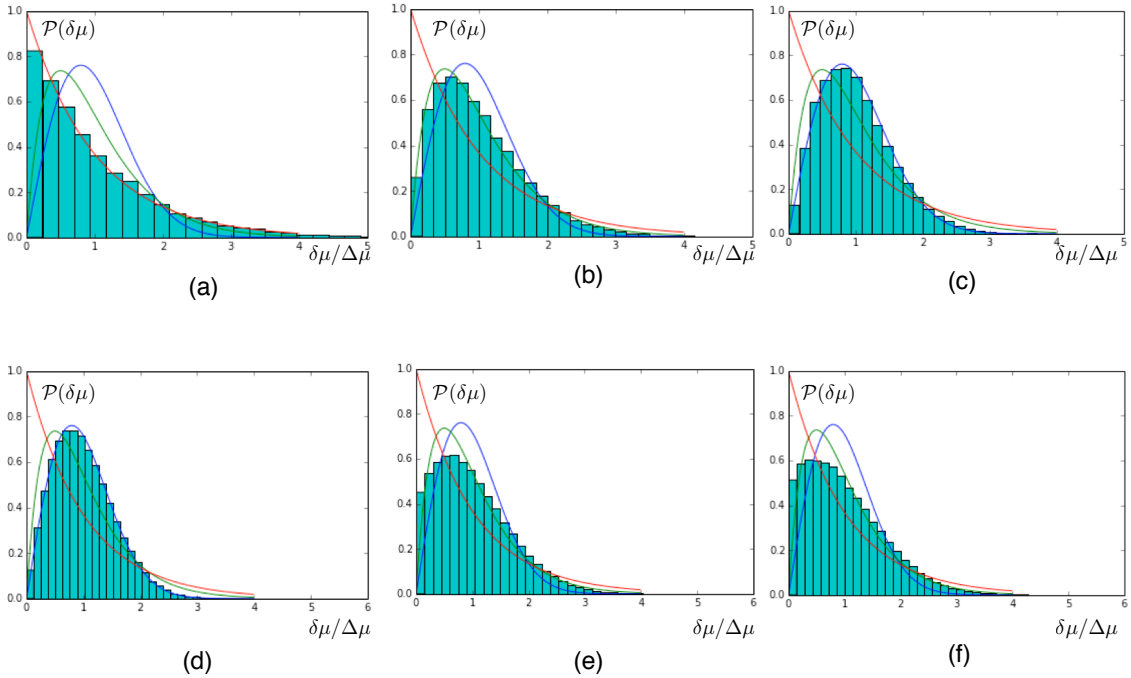

Figure 4.2: Level spacing distributions for localized wire with (a) $L \ll \ell$, (b) $L \gtrsim \ell$ and (c) $L \lesssim \ell$ in the p-wave regime. The red lines correspond to the Poisson distribution (Eq.Z4.9), the green line is semi-Poissonian (Eq 4.10 and the red line is Wigner-Dyson (Eq. 4.8). As the system becomes less polarized, an opposite spin comes into the picture ((e) through (f)), the statistics start to involve two independent sequences of crossing spaces even though each sequence is correlated within itself. Thus, the level repulsion disappears, while the large spacing tail remains Gaussian.

cavities with regular dynamics):

$$P(\delta\mu) = \exp\big(-\delta\mu/\Delta\mu\big). \tag{4.9}$$

When the localization length is comparable to the system size, the normal state system is near the Anderson phase transition, the states are forced to overlap leading to linear level repulsion for small spacings that turn into Poissonian ensemble for larger energy spacings (the scale being the Thouless energy), signaling the fractal structure of the Majorana wavefunction. The resulting distribution is semi-Poissonian:

$$P(\delta\mu) = \frac{\delta\mu}{\Delta\mu}\exp\big(-2\delta\mu/\Delta\mu\big). \tag{4.10}$$

4.5. *S*-wave Topological Superconductors

We now focus on a related system: a semiconductor wire under an applied magnetic field in proximity to an s-wave superconductorwoth Rashba spin-orbit coupling. The

Hamiltonian is given by:

$$H = h(p,x)\tau_z + \alpha p \sigma_y \tau_z + B\sigma_x + \Delta\tau_x. \tag{4.11}$$

Here, α the spin-orbit coupling strength, Δ is the induced s-wave order parameter, B the Zeeman energy, and $h(p,x) = p^2/2m + V(x) - \mu$ is the single particle Hamiltonian. The Pauli matrices in the spin space are denoted by σ_i ($i = x, y, z$). We have two external parameters μ and B. Echoing the calculation above, we again map the problem to a non-Hermitian one where real eigenvalues are the crossing points. For B [μ], we pre-multiply with σ_x [τ_z].

For B crossings we have:

$$A = h(p,x)\tau_z\sigma_x + i\alpha p \sigma_z \tau_z + \Delta\tau_x\sigma_x. \tag{4.12}$$

Alternatively, we can follow Ref. [73] or the method of the previous chapter (which derives from said reference) to off-diagonalize the Hamiltonian and obtain:

$$(h(p,x)\sigma_z - i\alpha p \sigma_x \phi_\pm \pm \Delta\sigma_x) = \pm B\phi_\pm \tag{4.13}$$

The solution to order α^2 is given by

$$\begin{aligned}\phi_\pm = \xi_\pm(b)\mathrm{e}^{\pm\kappa x}\big(Af(x;b) + Bg(x;b)\big) \\ +\xi_\pm(-b)\mathrm{e}^{\mp\kappa x}\big(Cf(x;-b) + Dg(x;-b)\big),\end{aligned} \tag{4.14}$$

where $b = \sqrt{B^2 - \Delta^2}$ and $\kappa = m\alpha\Delta/\hbar b$. $\xi_+(b)$ is the eigenvector of $b\sigma_z + \Delta\sigma_x$ having a positive eigenvalue. Here, $f(x;b)$ and $g(x;b)$ are local solutions of $h(p,x)\psi = b\psi$. We find the crossing points by demanding that ψ satisfies the full boundary conditions. Hence, we have a crossing point if $b = \pm\sqrt{B^2 - \Delta^2}$ is an eigenvalue of $h(p,x)$. The crossing points therefore form curves in the $B - \mu$ plane and satisfy:

$$B_n^2 = (\mu - E_n)^2 + \Delta^2, \tag{4.15}$$

where E_n's are the energy eigenvalues of the spinless, normal state Hamiltonian $h\psi = E_n\psi$. Using this relation we relate the crossing density as a function of B or μ in terms of the density of states $\nu(E) = \sum_n \delta(E - E_n)$:

$$\rho(B) = \sum_{p=0,1} \frac{\nu\big(\mu + (-1)^p\sqrt{B^2 - \Delta^2}\big)}{\sqrt{1 - \Delta^2/B^2}} \tag{4.16a}$$

$$\rho(\mu) = \sum_{p=0,1} \nu\big(\mu + (-1)^p\sqrt{B^2 - \Delta^2}\big). \tag{4.16b}$$

These relations are the central result of this chapter. It allows us to relate average and oscillations of crossing density as well as its correlations in terms of the well-known relations satisfied by normal-state DOS.

4.5.1. Level Spacing

The *average crossing spacing* can be obtained by inverting the average density:

$$\Delta\mu_s \propto \begin{cases} \frac{\theta(\mu+b)}{L}\left(\frac{\theta(\mu-b)\sqrt{\mu^2-B^2+\Delta^2}}{\sqrt{\mu+b}-\sqrt{\mu-b}}+\frac{\theta(b-\mu)}{\sqrt{\mu+b}}\right) & \text{if } d=1 \\ \frac{\theta(\mu+b)}{S}\left(\theta(\mu-b)\frac{1}{2}+\theta(b-\mu)\right) & \text{if } d=2 \\ \frac{\theta(\mu+b)}{V}\left(\frac{\theta(\mu-b)}{\sqrt{\mu+b}+\sqrt{\mu-b}}+\frac{\theta(b-\mu)}{\sqrt{\mu+b}}\right) & \text{if } d=3. \end{cases} \tag{4.17}$$

In particular, we see that at higher chemical potential values out of the clean topological phase boundary, $\mu > b$, the crossing spacing is approximately halved.

4.6. Conclusion

In this chapter, we derive the Weyl expansion for the mean spacing between adjacent parity crossings of the *s*-wave and *p*-wave topological superconductors. We also show that all crossing points are correlated and are the eigenvalues of a normal state Hamiltonian and coincide when plotted in terms of the effective parameters of this normal-state Hamiltonian. We also show that the statistics of the fluctuations of the parity crossing spacings are universal, but their respective ensemble and universal statistics depend on the comparison between the Thouless energy and mean energy spacing, which corresponds to a comparison between the localization length and the system size.

Chapter 5

WORK EXTRACTION AND LANDAUER'S PRINCIPLE IN A QUANTUM SPIN HALL DEVICE

In this chapter, we introduce an information engine device model, which could be utilized as a battery or a supercapacitor, that uses the spin-polarized edge currents of a quantum spin Hall device as the working fluid and a coupled (nuclear) spin bath as the Maxwell's Demon memory.

5.1. Introduction

According to Landauer's principle, erasure of one bit of information requires an amount of heat greater than $k_B T \ln 2$ to be dissipated [157, 158]. The principle ensures that the second law of thermodynamics is obeyed as a blank bit is utilized to extract work by an amount $k_B T \ln 2$ from the environment. The "engine" that is capable of this extraction is sometimes called a "Maxwell's Demon" (MD), referring to the thought experiment proposed by Maxwell in 1871 [159, 160]. While interest in MD from the point of view of fundamental physics never faded [161–163], promise of highly efficient engines that operate in the nano-domain as well as alternative methods of energy storage gave a recent impetus to research on the physics of MD both experimentally (using colloidal particles [164–166], photonic systems [167, 168], NMR systems [169, 170], single electron transistors [171–173], cavity QED with superconducting qubits) [174] and theoretically [175–188]. Despite the multitudinous platforms in which MD action is theorized or demonstrated, scalability remains an issue.

In this chapter, we propose and investigate a new MD implementation that harvests thermal energy from the electronic environment and converts it to electrical work using a quantum spin Hall insulator (QSHI). As a memory resource we use the available "spin bath" that usually includes the nuclear spins present in the device and/or magnetic impurities introduced via doping. QSHIs feature an insulating bulk and a pair of counter-propagating gapless spin-momentum locked helical edge states (HES). These states are

topologically protected from backscattering under time-reversal symmetry (TRS) [189] (see Figure 5.1). First predicted to occur in graphene nanoribbons [31, 37], they were later predicted and experimentally demonstrated in HgTe/CdTe quantum wells (QWs) [32, 39] as well as in InAs/GaSb QW structures [41, 190]. The TRS prohibiting the backscattering of the edge states is broken by the presence of nuclear or impurity spins. This backscattering shows up as extra dissipation, lowering the expected quantized conductance of the QSHI edge [191–195]. Here we show another salient feature of such scattering: an initial state of polarized nuclear spins (blank memory) drives an electrical current. Thus nuclear/impurity spins act as a memory resource of a MD that converts heat from the environment into electrical work.

We show below that for the heat harvesting operation of our engine, no energy exchange between nuclear and electronic systems is necessary; in fact, the nuclear spins are degenerate in our system, forming a non-energetic (pure) memory. Hence this is an alternative way for energy storage (Figure 5.2) that is protected from undesired explosive discharges. The total energy needed to reset the "memory" (or, in other words, recharge the device) by fully polarizing nuclear spins exceeds the extracted energy, in agreement with the second law of thermodynamics and Landauer's principle. We also provide a method to generate such a nuclear spin polarization, completing the discharge-recharge cycle of the quantum information engine (QIE) (Figure 5.2). Note that each nucleus with nonzero nuclear spin coupling to the electron spin in the QSHE system contributes to the MD memory, hence the MD memory size here could be several orders of magnitude larger compared to those that were reported in the literature, thus solving the scaling problem for heat harvesting engines. Furthermore, our estimates show that equivalent energy/power density of our proposed engine compares favorably with conventional energy storage such as supercapacitors.

5.2. Basic Operating Principles

We now describe the basic operating principles of our MD implementation. The effective dynamics of electrons and holes in QSHI materials is well described by the Bernevig-Hughes-Zhang (BHZ) Hamiltonian [32]:

$$\mathcal{H}_{\text{BHZ}} = \epsilon(k)\sigma_0\tau_z - Dk^2\sigma_0\tau_0 + A(k_x\sigma_z\tau_x - k_y\sigma_0\tau_y), \tag{5.1}$$

where $\epsilon(k) = M - Bk^2$ and M, B, D, A are the material parameters. Here $\sigma_i\tau_j \equiv \sigma_i \otimes \tau_j$ with σ_i and τ_j are the Pauli matrices corresponding to spin and electron-hole degrees of freedom respectively. In this description, the various two-dimensional QSHI

QW structures differ only in their material and effective parameters [22], while the main edge state physics remains the same (Figure 5.1a). Next, we project the system into an effective edge Hamiltonian, obtaining $h_\beta^{\text{eff}} = -i\beta\,\hbar v_F \partial_x \sigma_z$ where $\beta = +1$ ($\beta = -1$) for the bottom (top) edge and v_F is the Fermi velocity of the effective edge state (Figure 5.1b). Note that the spin axes becomes position dependent under spin-orbit coupling [196].

The second important element in our QIE is the nuclear spin subsystem that forms the "memory" of the MD that operates on electron-hole dynamics via their spins. We model the interaction between the spins of the nuclei and the spins of the electrons by the Fermi contact interaction. The total effective Hamiltonian including this interaction is then given by

$$\begin{aligned} H_\beta &= -i\beta\,\hbar v_F \partial_x \sigma_z + \lambda M_z(x)\sigma_z \\ H_{\text{s-flip}} &= \frac{\lambda}{2}\sum_{i=1}^{N} \delta(x - x_i)(I_{i+}\sigma_- + I_{i-}\sigma_+). \end{aligned} \tag{5.2}$$

where $I_\pm \sigma_\mp = \sum_{i=1}^{N} \delta(x - x_i)\, I_{i\pm}\sigma_\mp$ is the spin-flip term with I_i being the spin operator of the i^{th} nucleus, $M_z(x)$ the Overhauser field and λ the hyperfine interaction strength [197]. Note that the Overhauser field merely moves the edge state in momentum space without causing any gap and can be gauged away via the unitary transformation $H_\beta \to U H_\beta U^\dagger$ with $U = \exp(i\frac{\beta\lambda}{\hbar v_F}\int^x M_z(x')dx')$. For the sake of simplicity we assume the hyperfine interaction strength λ to be the same for each nuclear spin, which does not affect our overall results. We note that because the spin of the electron and its momentum is completely locked, as $H_{\text{s-flip}}$ flips the spin of the edge electron and one nuclear spin, it also causes backscattering (see Figure 5.1d). The Fermi contact interaction process runs in competition with other processes that affect the nuclear spins, mainly the quadrupole interaction causing spin-flip between nuclear spins. However, the rate of this interaction is orders of magnitude smaller than the coupling between nuclear and electronic spins [198].

We now describe the charging/discharging (or alternatively erasure/work extraction, see Appendix G) operation. In the charging phase, we apply a charge current, which without loss of generality we assume to be flowing to the left. Then there are more right movers than left movers and hence more up(down) spins in the bottom(top) edge. Therefore, there is more right to left backscattering for both edges (see Figure 5.2a), increasing the number of up(down) nuclear spins for the bottom(top) edge. This process polarizes the nuclear spins until a certain net bias-dependent value is reached [191, 193]. This is the process of dynamical nuclear polarization for the quantum spin Hall edges, well-known in other contexts such as spin injection from ferromagnets [199, 200]. We stress that under a current bias, opposite edges are driven towards opposite polarization

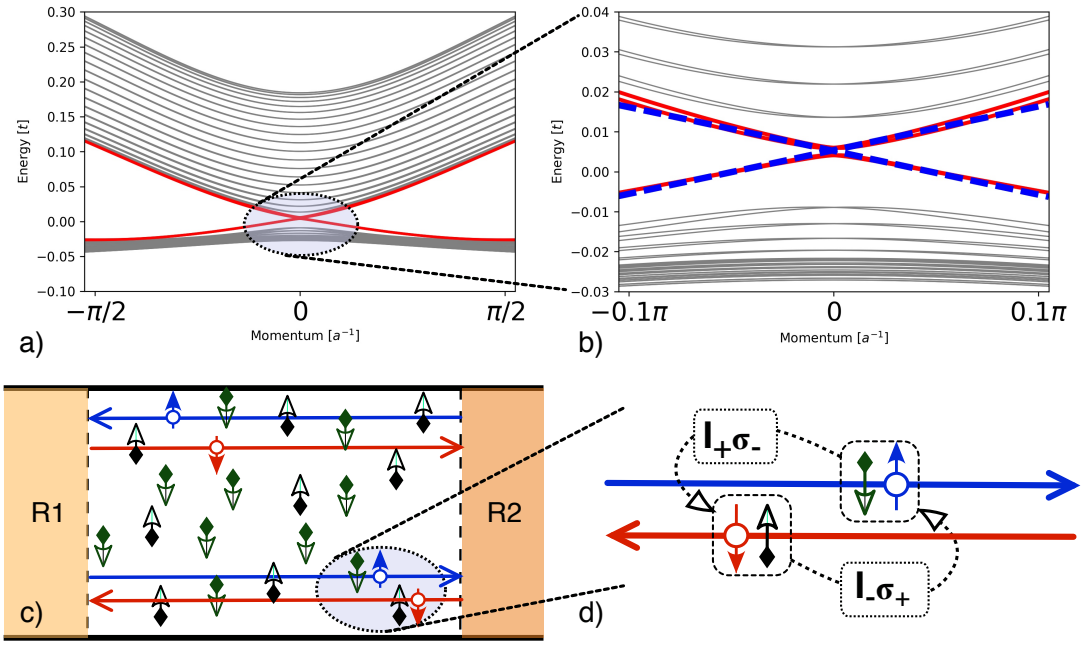

Figure 5.1: The quantum spin Hall insulator with nuclear spins and electron-nuclear spin flip interaction. (a) The band structure of a typical QSHE nanowire system (using the BHZ model with tight-binding approximation). Red lines represent the edge states. (b) The band structure of the simplified Hamiltonian h_{eff} projected to a single edge (dashed blue lines). (c) Schematic description of the QSHE system with the edge currents interacting with the nuclear spins in the system, with the diamonds representing nuclear spins. (d) The spin flip interaction with the nuclear spins that form the Maxwell Demon.

values.

More importantly, the reverse process is also possible: fully polarized nuclear spins near a QSH edge drive a charge current (see Figure 5.2b). This is the discharging phase. Consider a nonzero initial nuclear spin polarization (caused by, say, the driving current that was applied earlier, hence has opposite signs for opposite edges) and for the sake of simplicity assume zero applied voltage bias. Now there are more up(down)-nuclear spins than down(up)-nuclear spins in the bottom(top) edge, hence there are more down(up)-spins flipped to up(down)-spins in the bottom(top) edge leading to an imbalance of left movers relative to right movers. Any time a backscattering occurs, the event leaves its footprint via a spin-flip in the nuclear memory. A reverse bias can now be applied so that the current is opposite of the voltage bias in order to extract work (see Appendix G). We show below that the energy is supplied by the thermal energy of the reservoirs. All this is reminiscent of a MD operation wherein the MD predominantly backscatters the right movers relative to the left movers, thus setting up a current between reservoirs that are otherwise in equilibrium, while recording the outcome in the nuclear spin memory(see Figure 5.2). Under applied reverse bias, the MD/QIE harvests heat to convert it to electrical work.

5.3. Dynamics of The System

We now quantify our model. The spin-flip scattering rate at the edge can be calculated using Fermi's golden rule. As mentioned above, all right(left) moving electrons have spin up(down) for the bottom edge (for the top edge all left(right) moving electrons have spin down(up)). From now on, without loss of generality, we focus on the bottom edge, where we denote the corresponding distribution functions by the subscript $+(-)$. Then the total rate for a single spin-flip scattering at a given energy, in which a right mover becomes a left mover by flipping a nuclear spin from down to up is given by [191, 193]:

$$\Gamma_{-+}(\epsilon) = \frac{\gamma_0}{\hbar} N_\downarrow f_+(\epsilon)(1 - f_-(\epsilon)), \tag{5.3}$$

where $\gamma_0 \equiv \lambda^2/8\pi\hbar^2 v_F^2$ is a dimensionless effective interaction strength for a single nuclear spin.

5.3.1. Nuclear Polarization Dynamics

The effects of spin-flip scattering on the nuclear spins is given by the rate equation:

$$\frac{dN_\uparrow}{dt} = \int d\epsilon \left(\Gamma_{-+}(\epsilon) - \Gamma_{+-}(\epsilon)\right). \tag{5.4}$$

We find it useful to define the mean polarization $m \equiv \frac{N_\uparrow - N_\downarrow}{2(N_\uparrow + N_\downarrow)}$. Then, the rate of change of the mean polarization m is written as:

$$\frac{dm}{dt} = \gamma_0 \Gamma_B - m\gamma_0 \Gamma_T, \tag{5.5}$$

where

$$\begin{aligned} \Gamma_B &= \int \frac{d\epsilon}{\hbar} \frac{f_+ - f_-}{2}, \\ \Gamma_T &= \int \frac{d\epsilon}{\hbar} (f_+ + f_- - 2f_+f_-). \end{aligned} \tag{5.6}$$

We assume a short edge (see below) and approximate the distributions $f_\pm^0$ by the Fermi distribution of the reservoir from which they originate. We then obtain $\hbar\Gamma_B = (\mu_L - \mu_R)/2$, and $\hbar\Gamma_T = (\mu_L - \mu_R)\coth(\frac{\mu_L - \mu_R}{2k_BT})$. Hence, using Eq. (5.5), the polarization dynamics is given by

$$m(t) = (m_0 - \bar{m})\mathrm{e}^{-t/\tau_m} + \bar{m}, \tag{5.7}$$

where m_0 is the initial mean polarization and $\bar{m} \equiv \Gamma_B/\Gamma_T = (1/2)\tanh(\frac{\mu_L - \mu_R}{2k_BT})$ is defined to be the target mean polarization and $\tau_m = 1/\gamma_0\Gamma_T$ is the characteristic time

scale for nuclear polarization dynamics.

5.3.2. Electron Dynamics and Induced Current

We now calculate the total current. The distribution functions obey the Boltzmann-like equation for the edge in consideration:

$$\partial_t f_\pm = \pm(\Gamma_{+-}(\epsilon) - \Gamma_{-+}(\epsilon)\,)\,\nu(0)^{-1} \mp v_F \partial_x f_+,$$

where, $\nu(0) = L/2\pi\hbar v_F$ is the density of states of the edge electrons. We assume that the nuclear polarization m is changing slowly and seek a steady state solution. Then the distributions obey:

$$\partial_x f_\pm = (\Gamma_{+-}(\epsilon) - \Gamma_{-+}(\epsilon)\,)\,(v_F\nu(0))^{-1} \equiv \Gamma[f_+, f_-] \tag{5.8}$$

For short edges ($\Gamma L \ll 1$), we expand in gradients of the distribution functions. At the leading order, we obtain a linear position dependence:

$$f_\pm = f_\pm^0 + \Gamma[f_+^0, f_-^0]\,(x \pm L/2), \tag{5.9}$$

where $f_\pm^0$ is the distribution of the left(right) reservoir. We then obtain the total current:

$$I_{tot} = \frac{e}{h}\int d\epsilon(f_+ - f_-) = \frac{e^2}{h}V - eN\gamma_0(\Gamma_B - m\Gamma_T). \tag{5.10}$$

We identify and focus on two sources of current in the system in the short edge regime: (i) the usual current $\frac{e^2}{h}V$ due to voltage bias without the nuclear spin flip interaction, and (ii) the MD-induced current $-eN\frac{dm}{dt} = -eN\gamma_0\,(\Gamma_B - m\Gamma_T)$ due to the presence of nuclear polarization m. In the latter case, a net backscattering current, caused by right-moving up spin electrons scattering to left-moving down spin electron states, is driven by a net negative nuclear spin and vice versa. The net polarization of the nuclear spins acts as an MD.

We note that the total current is not zero for vanishing bias voltage, demonstrating the "Demon action" that induces a current between two reservoirs at equal temperature and chemical potential, while using the nuclear spins as a memory resource.

5.3.3. Generated Power

In order to use the quantum information engine, we attach it to an electrical circuit as in Fig. 5.2. In this setup, the QIE provides power to loads 1 and 2, which can be modeled by

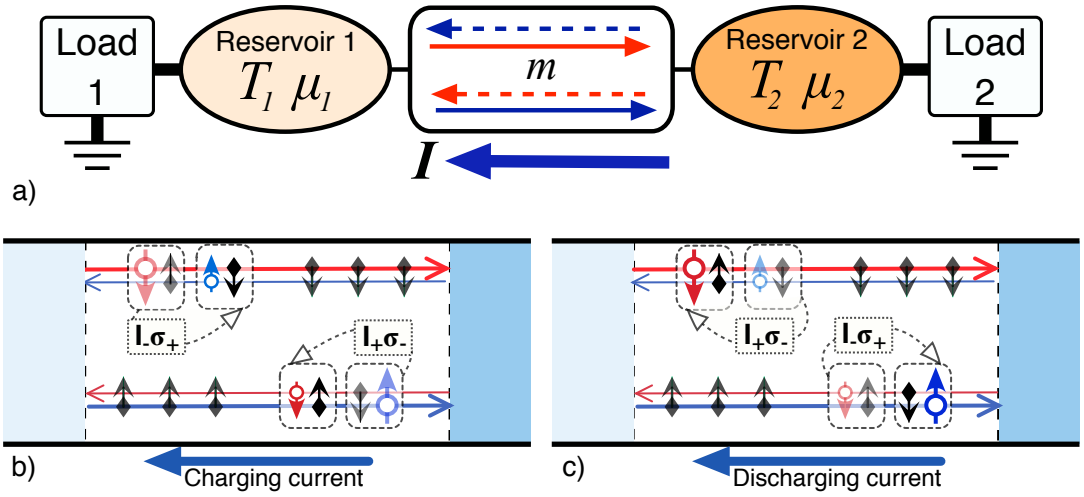

Figure 5.2: (a) QSH based quantum information engine, providing power to loads 1 and 2. Schematic description of (b) the charging and (c) the discharging phase of the QIE. In the charging phase, an applied bias current aligns the nuclear spins. In the discharging phase, flipping nuclear spins drive a current. An applied reverse bias can extract power.

a (reverse) bias voltage V. The power generated (Fig. 5.3) is given by:

$$P = \frac{eV}{h}\left[eV(1-\pi N\gamma_0) + 2\pi N\gamma_0\hbar\Gamma_T m\right]. \tag{5.11}$$

For $eV < \frac{2\zeta\Gamma_T m}{(\zeta-2)}$, with $\zeta = 2\pi N\gamma_0$, we obtain $P < 0$, indicating the fact that the circuit is powered by the QIE. (For $eV > \frac{2\zeta\Gamma_T m}{(\zeta-2)}$, the circuit is providing power to charge the nuclear spin resource). We find the maximal work done by the nuclear spin resource in the weak coupling/short edge limit by maximizing the power and integrating up to the time when the power changes sign:

$$W_{tot} = \alpha k_B T N^2 \gamma_0. \tag{5.12}$$

where α is a parameter of $\mathcal{O}(1)$ (We note that $\alpha \sim \pi/4$ for a work extraction under constant voltage bias. We also note that the time it takes to complete the charge/discharge cycle is only limited by the time it takes for an edge-resolved nuclear spin polarization to relax via spin-flip between nuclear spins. Nuclear spin polarization in similar systems have been reported to hold for days [201].). In this limit, the amount of extracted work follows a quadratic scaling law that implies denser storage than the conventional/expected linear scaling. Here, T is the operating temperature, limited by the gap of the helical topological state in question.

5.4. Experimental Realization

We now discuss experimental feasibility of our MD implementation. Systems featuring spin-momentum locked topological edge states have been available to experiments for

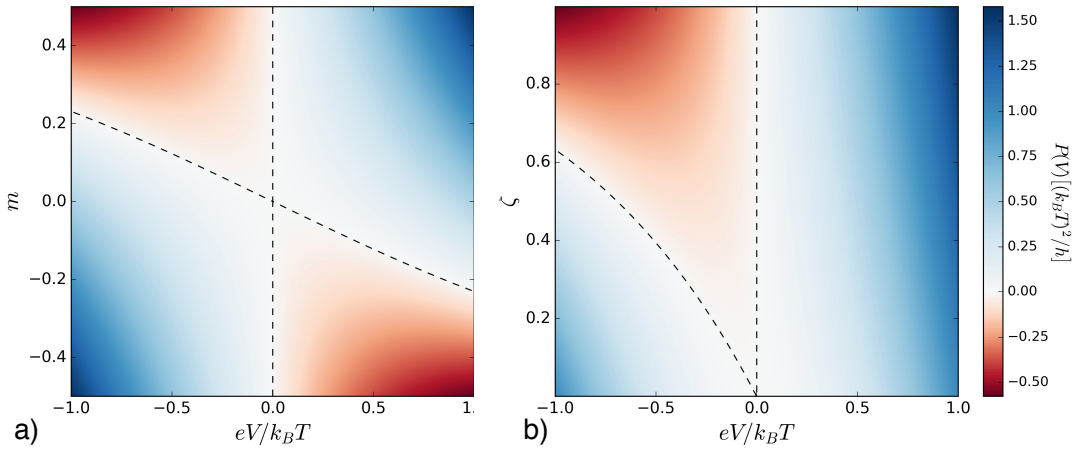

Figure 5.3: P-V graph, calculated using Eq. 5.11, (a) as a function of mean polarization m with $\zeta = 1.0$ and (b) as a function of ζ with full polarization m = 0.5. On the dashed line, P = 0. Power can have negative values for $V < 0$ $(V > 0)$ for a given mean polarization $m > 0$ $(m < 0)$ (here, $e > 0$), as an indication of the work extraction phase.

about a decade [15, 34]. Among these materials, systems with high nuclear spin density generally provide high energy density. In addition, systems with higher bulk band gaps could be operated at higher temperatures, again leading to higher energy densities (see Eq. 5.12). Systems that feature high hyperfine interaction strength or low Fermi velocity provide high power density and fast operation, thus can be utilized as spin-supercapacitors. Assuming $N \sim 10^7$ and $\gamma_0 \sim 10^{-8}$, we estimate the equivalent energy density and power density that can be stored in the device in the short edge limit to be $\sim 10\text{kJ/kg}$ and $\sim 10\text{MW/kg}$ (not including overhead). On the other hand, systems with low interaction strength (see Eq. 5.3) due to high Fermi velocity and/or suppressed hyperfine interaction can be utilized as spin batteries that keep their polarization for long times. For example, thin film flakes of 3D topological QSH insulator Bi_2Te_2Se (BTS221) feature a relatively large Fermi velocity ($v_F \sim 10^6 m/s$) [202], which is two orders of magnitude larger than that of, say, InAs/GaSB QWs ($v_F \sim 10^4 m/s$) [190]. Thus, BTS221 features a much smaller electron-nuclear spin flip interaction strength (therefore requiring large currents to write the spin memory) and orders of magnitude longer memory retention times. In fact, recent experimental work that uses thin film flakes of BTS221 observed days long polarization retention times [201].

We next consider InAs/GaSb QW structures as an example. These QWs have a smaller Fermi velocity v_F [189, 190] and higher nuclear spin density compared to, for example, HgCdTe QWs [203]. This hints to a larger $N\gamma_0$ in InAs/GaSb QWs and therefore to a faster operation and higher energy density. We note that in these QWs, the electrons have spin $\pm 1/2$ but the holes have spin $\pm 3/2$ whose coupling to the spin flip interaction

requires a higher order process [203]. The nuclear spin density in these QWs, as well as the effective electron spin–nuclear spin coupling strength, could possibly be further adjusted by magnetic impurity doping, providing a design freedom that might prove useful for different functionalities of the QIE.

5.5. Conclusion

In conclusion, we have described a Maxwell's Demon system that utilizes the spin-flip interaction between helical edge states and nuclear spins in quantum spin Hall topological insulators. Available nuclear or magnetic impurity spins can be utilized as a Maxwell's demon memory to harvest work from thermal energy of the reservoirs. We also showed how to erase the memory and thus "charge" the system by applying a voltage bias. Erasing the memory (or polarizing the spin subsystem) requires dissipation of heat by an amount at least $k_B T \ln 2$ per bit, in agreement with the Landauer's principle and the second law. Estimates of equivalent work that can be extracted show that power/energy densities that exceed existing supercapacitors are achievable.

Chapter 6

CONCLUSION

In this thesis, we considered the effects of disorder and scattering in low dimensional topological materials in one or two dimensions [1–3].

In chapter 2, we gave a brief overview of topological materials as a background in consideration of the subject matter of the thesis.

In chapter 3, we investigated the effect of disorder in multichannel Rashba SOC proximity-induced topological superconductor nanowires (RSW nanowires) at experimentally relevant parameter ranges. We derived formulae that determine all topological phase boundaries of a multichannel disordered RSW wire. We then tested these formulae with numerical tight-binding simulations at experimentally relevant parameter ranges and found good agreement without any fitting parameters. We showed that there are additional topological transitions for the RSW wires leading to a richer phase diagram with further fragmentation beyond that of the *p*-wave models [1].

In chapter 4, we studied the statistics of level-crossings in dirty superconductor nanostructures at the Fermi energy as a function of external parameters such as the magnetic field B or the chemical potential μ. We obtained formulae for the average crossing density. We found that the fluctuations in these systems also follow universal statistics that may be either Gaussian orthogonal, Poissonian or sub-Poissonian, depending on the underlying scattering details as well as the geometry of the sample. Our results extend the results of Ref. [131] to more realistic wires and dot geometries. We also found that the parity crossing points are described by the normal-state properties of the system. We finally discussed under what conditions these crossings signal MFs [2].

In chapter 5, we have described a Maxwell's Demon system that utilizes the spin-flip interaction between helical edge states and nuclear spins in quantum spin Hall topological insulators. We showed that the available nuclear or magnetic impurity spins can be utilized as a Maxwell's demon memory to harvest work from thermal energy of the reservoirs. We also showed how to erase the memory and thus "charge" the system by applying a voltage bias, and demonstrated the agreement of our findings with with the Landauer's

principle and the second law. Estimates of equivalent work that can be extracted show that power/energy densities that exceed existing supercapacitors are achievable [3].

Bibliography

[1] B. Pekerten, A. Teker, O. Bozat, M. Wimmer, and I. Adagideli, "Disorder-induced topological transitions in multichannel Majorana wires," *Phys. Rev. B*, vol. 95, p. 064507, 2017.

[2] B. Pekerten, A. M. Bozkurt, and I. Adagideli, "Can one hear the shape of a topological crossing?" Manuscript in progress.

[3] A. Mert Bozkurt, B. Pekerten, and I. Adagideli, "Work Extraction and Landauer's Principle in a Quantum Spin Hall Device," *arXiv* 1705.04985, 2017.

[4] K. v. Klitzing, G. Dorda, and M. Pepper, "New method for high-accuracy determination of the fine-structure constant based on quantized Hall resistance," *Phys. Rev. Lett.*, vol. 45, p. 494, 1980.

[5] R. B. Laughlin, "Quantized Hall conductivity in two dimensions," *Phys. Rev. B*, vol. 23, p. 5632, 1981.

[6] D. J. Thouless, M. Kohmoto, M. P. Nightingale, and M. den Nijs, "Quantized Hall conductance in a two-dimensional periodic potential," *Phys. Rev. Lett.*, vol. 49, p. 405, 1982.

[7] M. Kohmoto, "Topological invariant and the quantization of the Hall conductance," *Annals of Physics*, vol. 160, no. 2, p. 343, 1985.

[8] J. M. Kosterlitz and D. J. Thouless, "Long range order and metastability in two dimensional solids and superfluids. (application of dislocation theory)," *Journal of Physics C: Solid State Physics*, vol. 5, no. 11, p. L124, 1972.

[9] J. M. Kosterlitz and D. J. Thouless, "Ordering, metastability and phase transitions in two-dimensional systems," *Journal of Physics C: Solid State Physics*, vol. 6, no. 7, p. 1181, 1973.

[10] D. C. Tsui, H. L. Stormer, and A. C. Gossard, "Two-dimensional magnetotransport in the extreme quantum limit," *Phys. Rev. Lett.*, vol. 48, p. 1559, 1982.

[11] R. B. Laughlin, "Anomalous quantum Hall effect: An incompressible quantum fluid with fractionally charged excitations," *Phys. Rev. Lett.*, vol. 50, p. 1395, 1983.

[12] F. D. M. Haldane, "Nonlinear field theory of large-spin heisenberg antiferromagnets: Semiclassically quantized solitons of the one-dimensional easy-axis néel state," *Phys. Rev. Lett.*, vol. 50, p. 1153, 1983.

[13] F. D. M. Haldane, "Model for a quantum Hall effect without landau levels: Condensed-matter realization of the "parity anomaly"," *Phys. Rev. Lett.*, vol. 61, p. 2015, 1988.

[14] H. L. Stormer, "Nobel lecture: The fractional quantum Hall effect," *Rev. Mod. Phys.*, vol. 71, p. 875, 1999.

[15] X.-L. Qi and S.-C. Zhang, "Topological insulators and superconductors," *Rev. Mod. Phys.*, vol. 83, p. 1057, 2011.

[16] M. Leijnse and K. Flensberg, "Introduction to topological superconductivity and Majorana fermions," *Semiconductor Science and Technology*, vol. 27, no. 12, p. 124003, 2012.

[17] Y. Ando and L. Fu, "Topological Crystalline Insulators and Topological Superconductors: From Concepts to Materials," *Annual Review of Condensed Matter Physics*, vol. 6, p. 361, 2017.

[18] R. M. Kaufmann, D. Li, and B. Wehefritz-Kaufmann, "Notes on topological insulators," *Reviews in Mathematical Physics*, vol. 28, no. 10, p. 1630003, 2016.

[19] R. Resta, "Geometry and topology in electronic structure theory." Lecture notes obtained from webpage at http://www-dft.ts.infn.it/~resta/, Accessed 26.06.2017, 2016.

[20] D. Tong, "Lectures on the Quantum Hall Effect," *arXiv* 1606.06687, 2016.

[21] D. Thouless, *Topological Quantum Numbers in Nonrelativistic Physics*. World Scientific Publishing Company Pte Limited, 1998.

[22] M. Franz and L. Molenkamp, eds., *Topological Insulators*, vol. 6 of *Contemporary Concepts of Condensed Matter Science*. Elsevier, 2013.

[23] B. A. Bernevig and T. Hughes, *Topological Insulators and Topological Superconductors*. Princeton University Press, 41 William Street, Princeton, New Jersey 08540: Princeton University Press, 2013.

[24] F. Ortmann, S. Roche, S. Valenzuela, and L. Molenkamp, *Topological Insulators: Fundamentals and Perspectives*. Wiley, 2015.

[25] J. Asbóth, L. Oroszlány, and A. Pályi, *A Short Course on Topological Insulators: Band Structure and Edge States in One and Two Dimensions*. Lecture Notes in Physics, Springer International Publishing, 2016.

[26] S. Shen, *Topological Insulators: Dirac Equation in Condensed Matter*. Springer Series in Solid-State Sciences, Springer Singapore, 2017.

[27] M. Nakahara, *Geometry, Topology and Physics, Second Edition*. Graduate student series in physics, Taylor & Francis, 2003.

[28] A. Matsko, A. Savchenkov, D. Strekalov, V. Ilchenko, and L. Maleki, "Review of applications of whispering-gallery mode resonators in photonics and nonlinear optics," *IPN Progress Report*, vol. 42, no. 162, p. 1, 2005.

[29] D. V. Strekalov, C. Marquardt, A. B. Matsko, H. G. L. Schwefel, and G. Leuchs, "Nonlinear and quantum optics with whispering gallery resonators," *Journal of Optics*, vol. 18, no. 12, p. 123002, 2016.

[30] M. V. Berry, "Quantal phase factors accompanying adiabatic changes," *Proceedings of the Royal Society of London A: Mathematical, Physical and Engineering Sciences*, vol. 392, no. 1802, p. 45, 1984.

[31] C. L. Kane and E. J. Mele, "Z_2 topological order and the quantum spin Hall effect," *Phys. Rev. Lett.*, vol. 95, p. 146802, 2005.

[32] B. A. Bernevig, T. L. Hughes, and S.-C. Zhang, "Quantum spin Hall effect and topological phase transition in HgTe quantum wells," *Science*, vol. 314, no. 5806, p. 1757, 2006.

[33] L. Fu and C. L. Kane, "Topological insulators with inversion symmetry," *Phys. Rev. B*, vol. 76, p. 045302, 2007.

[34] M. Z. Hasan and C. L. Kane, "*Colloquium* : Topological insulators," *Rev. Mod. Phys.*, vol. 82, p. 3045, 2010.

[35] K. S. Novoselov, A. K. Geim, S. V. Morozov, D. Jiang, Y. Zhang, S. V. Dubonos, I. V. Grigorieva, and A. A. Firsov, "Electric field effect in atomically thin carbon films," *Science*, vol. 306, no. 5696, p. 666, 2004.

[36] A. H. Castro Neto, F. Guinea, N. M. R. Peres, K. S. Novoselov, and A. K. Geim, "The electronic properties of graphene," *Rev. Mod. Phys.*, vol. 81, p. 109, 2009.

[37] C. L. Kane and E. J. Mele, "Quantum spin Hall effect in graphene," *Phys. Rev. Lett.*, vol. 95, p. 226801, 2005.

[38] M. Gmitra, S. Konschuh, C. Ertler, C. Ambrosch-Draxl, and J. Fabian, "Band-structure topologies of graphene: Spin-orbit coupling effects from first principles," *Phys. Rev. B*, vol. 80, p. 235431, 2009.

[39] M. König, S. Wiedmann, C. Brüne, A. Roth, H. Buhmann, L. W. Molenkamp, X.-L. Qi, and S.-C. Zhang, "Quantum spin Hall insulator state in HgTe quantum wells," *Science*, vol. 318, no. 5851, p. 766, 2007.

[40] A. Roth, C. Brüne, H. Buhmann, L. W. Molenkamp, J. Maciejko, X.-L. Qi, and S.-C. Zhang, "Nonlocal transport in the quantum spin Hall state," *Science*, vol. 325, no. 5938, p. 294, 2009.

[41] C. Liu, T. L. Hughes, X.-L. Qi, K. Wang, and S.-C. Zhang, "Quantum spin Hall effect in inverted type-II semiconductors," *Phys. Rev. Lett.*, vol. 100, p. 236601, 2008.

[42] I. Knez, R. R. Du, and G. Sullivan, "Finite conductivity in mesoscopic Hall bars of inverted InAs/GaSb quantum wells," *Phys. Rev. B*, vol. 81, p. 201301, 2010.

[43] J. Alicea, "New directions in the pursuit of Majorana fermions in solid state systems," *Reports on Progress in Physics*, vol. 75, no. 7, p. 076501, 2012.

[44] C. Beenakker, "Search for Majorana fermions in superconductors," *Annual Review of Condensed Matter Physics*, vol. 4, no. 1, p. 113, 2013.

[45] S. R. Elliott and M. Franz, "*Colloquium* : Majorana fermions in nuclear, particle, and solid-state physics," *Rev. Mod. Phys.*, vol. 87, p. 137, 2015.

[46] D. Aasen, M. Hell, R. V. Mishmash, A. Higginbotham, J. Danon, M. Leijnse, T. S. Jespersen, J. A. Folk, C. M. Marcus, K. Flensberg, and J. Alicea, "Milestones toward Majorana-based quantum computing," *Phys. Rev. X*, vol. 6, p. 031016, 2016.

[47] E. Majorana and L. Maiani, *A symmetric theory of electrons and positrons*, p. 201. Berlin, Heidelberg: Springer Berlin Heidelberg, 2006.

[48] E. Majorana, "Teoria simmetrica dell'elettrone e del positrone," *Il Nuovo Cimento (1924-1942)*, vol. 14, no. 4, p. 171, 2008.

[49] G. E. Volovik, "Fermion zero modes on vortices in chiral superconductors," *Journal of Experimental and Theoretical Physics Letters*, vol. 70, no. 9, p. 609, 1999.

[50] T. D. Stanescu, R. M. Lutchyn, and S. Das Sarma, "Majorana fermions in semiconductor nanowires," *Phys. Rev. B*, vol. 84, p. 144522, 2011.

[51] R. Roy, "Topological superfluids with time reversal symmetry," *arXiv* 0803.2868, 2008.

[52] X.-L. Qi, T. L. Hughes, S. Raghu, and S.-C. Zhang, "Time-reversal-invariant topological superconductors and superfluids in two and three dimensions," *Phys. Rev. Lett.*, vol. 102, p. 187001, 2009.

[53] S. B. Chung and S.-C. Zhang, "Detecting the Majorana fermion surface state of ^{3}He-*B* through spin relaxation," *Phys. Rev. Lett.*, vol. 103, p. 235301, 2009.

[54] A. P. Mackenzie and Y. Maeno, "The superconductivity of Sr_2RuO_4 and the physics of spin-triplet pairing," *Rev. Mod. Phys.*, vol. 75, p. 657, 2003.

[55] R. M. Lutchyn, J. D. Sau, and S. Das Sarma, "Majorana fermions and a topological phase transition in semiconductor-superconductor heterostructures," *Phys. Rev. Lett.*, vol. 105, p. 077001, 2010.

[56] Y. Oreg, G. Refael, and F. von Oppen, "Helical liquids and Majorana bound states in quantum wires," *Phys. Rev. Lett.*, vol. 105, p. 177002, 2010.

[57] F. Pientka, L. I. Glazman, and F. von Oppen, "Topological superconducting phase in helical Shiba chains," *Phys. Rev. B*, vol. 88, p. 155420, 2013.

[58] S. Nadj-Perge, I. K. Drozdov, J. Li, H. Chen, S. Jeon, J. Seo, A. H. MacDonald, B. A. Bernevig, and A. Yazdani, "Observation of Majorana fermions in ferromagnetic atomic chains on a superconductor," *Science*, vol. 346, no. 6209, p. 602, 2014.

[59] A. Kitaev, "Fault-tolerant quantum computation by anyons," *Annals of Physics*, vol. 303, no. 1, p. 2, 2003.

[60] C. Nayak, S. H. Simon, A. Stern, M. Freedman, and S. Das Sarma, "Non-Abelian anyons and topological quantum computation," *Rev. Mod. Phys.*, vol. 80, p. 1083, 2008.

[61] J. Alicea, "Majorana fermions in a tunable semiconductor device," *Phys. Rev. B*, vol. 81, p. 125318, 2010.

[62] B. I. Halperin, Y. Oreg, A. Stern, G. Refael, J. Alicea, and F. von Oppen, "Adiabatic manipulations of Majorana fermions in a three-dimensional network of quantum wires," *Phys. Rev. B*, vol. 85, p. 144501, 2012.

[63] A. Y. Kitaev, "Unpaired Majorana fermions in quantum wires," *Physics-Uspekhi*, vol. 44, no. 10S, p. 131, 2001.

[64] Élie Cartan, "Sur une classe remarquable d'espaces de Riemann, I," *Bulletin de la Société Mathématique de France*, vol. 54, p. 214, 1926.

[65] Élie Cartan, "Sur une classe remarquable d'espaces de Riemann, II," *Bulletin de la Société Mathématique de France*, vol. 55, p. 114, 1927.

[66] K. Efetov, *Supersymmetry in Disorder and Chaos*. Cambridge University Press, 1999.

[67] A. Altland and M. R. Zirnbauer, "Nonstandard symmetry classes in mesoscopic normal-superconducting hybrid structures," *Phys. Rev. B*, vol. 55, p. 1142, 1997.

[68] A. Kitaev, "Periodic table for topological insulators and superconductors," *AIP Conference Proceedings*, vol. 1134, no. 1, p. 22, 2009.

[69] I. C. Fulga, F. Hassler, A. R. Akhmerov, and C. W. J. Beenakker, "Scattering formula for the topological quantum number of a disordered multimode wire," *Phys. Rev. B*, vol. 83, p. 155429, 2011.

[70] S. Ryu, A. P. Schnyder, A. Furusaki, and A. W. W. Ludwig, "Topological insulators and superconductors: Tenfold way and dimensional hierarchy," *New Journal of Physics*, vol. 12, no. 6, p. 065010, 2010.

[71] A. P. Schnyder, S. Ryu, A. Furusaki, and A. W. W. Ludwig, "Classification of topological insulators and superconductors," *AIP Conference Proceedings*, vol. 1134, no. 1, p. 10, 2009.

[72] S. Datta, *Electronic Transport in Mesoscopic Systems*. Cambridge Studies in Semiconductor Physi, Cambridge University Press, 1997.

[73] I. Adagideli, M. Wimmer, and A. Teker, "Effects of electron scattering on the topological properties of nanowires: Majorana fermions from disorder and superlattices," *Phys. Rev. B*, vol. 89, p. 144506, 2014.

[74] R. Jackiw and P. Rossi, "Zero modes of the vortex-fermion system," *Nuclear Physics B*, vol. 190, no. 4, p. 681, 1981.

[75] M. M. Salomaa and G. E. Volovik, "Cosmiclike domain walls in superfluid ^3B: Instantons and diabolical points in (k,r) space," *Phys. Rev. B*, vol. 37, p. 9298, 1988.

[76] G. W. Moore and N. Read, "Nonabelions in the fractional quantum Hall effect," *Nucl. Phys.*, vol. B360, p. 362, 1991.

[77] N. Read and D. Green, "Paired states of fermions in two dimensions with breaking of parity and time-reversal symmetries and the fractional quantum Hall effect," *Phys. Rev. B*, vol. 61, p. 10267, 2000.

[78] D. A. Ivanov, "Non-Abelian statistics of half-quantum vortices in p-wave superconductors," *Phys. Rev. Lett.*, vol. 86, p. 268, 2001.

[79] J. D. Sau, S. Tewari, R. M. Lutchyn, T. D. Stanescu, and S. Das Sarma, "Non-Abelian quantum order in spin-orbit-coupled semiconductors: Search for topological majorana particles in solid-state systems," *Phys. Rev. B*, vol. 82, p. 214509, 2010.

[80] T.-P. Choy, J. M. Edge, A. R. Akhmerov, and C. W. J. Beenakker, "Majorana fermions emerging from magnetic nanoparticles on a superconductor without spin-orbit coupling," *Phys. Rev. B*, vol. 84, p. 195442, 2011.

[81] M. Kjaergaard, K. Wölms, and K. Flensberg, "Majorana fermions in superconducting nanowires without spin-orbit coupling," *Phys. Rev. B*, vol. 85, p. 020503, 2012.

[82] I. Martin and A. F. Morpurgo, "Majorana fermions in superconducting helical magnets," *Phys. Rev. B*, vol. 85, p. 144505, 2012.

[83] S. Nadj-Perge, I. K. Drozdov, B. A. Bernevig, and A. Yazdani, "Proposal for realizing Majorana fermions in chains of magnetic atoms on a superconductor," *Phys. Rev. B*, vol. 88, p. 020407, 2013.

[84] B. Braunecker and P. Simon, "Interplay between classical magnetic moments and superconductivity in quantum one-dimensional conductors: Toward a self-sustained topological Majorana phase," *Phys. Rev. Lett.*, vol. 111, p. 147202, 2013.

[85] J. Klinovaja, P. Stano, A. Yazdani, and D. Loss, "Topological superconductivity and Majorana fermions in RKKY systems," *Phys. Rev. Lett.*, vol. 111, p. 186805, 2013.

[86] S. Nakosai, Y. Tanaka, and N. Nagaosa, "Two-dimensional p-wave superconducting states with magnetic moments on a conventional s-wave superconductor," *Phys. Rev. B*, vol. 88, p. 180503, 2013.

[87] M. M. Vazifeh and M. Franz, "Self-organized topological state with Majorana fermions," *Phys. Rev. Lett.*, vol. 111, p. 206802, 2013.

[88] Y. Kim, M. Cheng, B. Bauer, R. M. Lutchyn, and S. Das Sarma, "Helical order in one-dimensional magnetic atom chains and possible emergence of Majorana bound states," *Phys. Rev. B*, vol. 90, p. 060401, 2014.

[89] J. Röntynen and T. Ojanen, "Topological superconductivity and high Chern numbers in 2D ferromagnetic Shiba lattices," *Phys. Rev. Lett.*, vol. 114, p. 236803, 2015.

[90] J. Li, T. Neupert, Z. Wang, A. H. MacDonald, A. Yazdani, and B. A. Bernevig, "Two-dimensional chiral topological superconductivity in Shiba lattices," *Nature Communications*, vol. 7, p. 12297, 2016.

[91] B. Scharf and I. Žutić, "Probing Majorana-like states in quantum dots and quantum rings," *Phys. Rev. B*, vol. 91, p. 144505, 2015.

[92] V. Mourik, K. Zuo, S. M. Frolov, S. R. Plissard, E. P. A. M. Bakkers, and L. P. Kouwenhoven, "Signatures of Majorana fermions in hybrid superconductor-semiconductor nanowire devices," *Science*, vol. 336, no. 6084, p. 1003, 2012.

[93] A. Das, Y. Ronen, Y. Most, Y. Oreg, M. Heiblum, and H. Shtrikman, "Zero-bias peaks and splitting in an al-inas nanowire topological superconductor as a signature of Majorana fermions," *Nat. Phys.*, vol. 8, no. 12, p. 887, 2012.

[94] M. T. Deng, C. L. Yu, G. Y. Huang, M. Larsson, P. Caroff, and H. Q. Xu, "Anomalous zero-bias conductance peak in a Nb-InSb nanowire-Nb hybrid device," *Nano Letters*, vol. 12, no. 12, p. 6414, 2012.

[95] A. D. K. Finck, D. J. Van Harlingen, P. K. Mohseni, K. Jung, and X. Li, "Anomalous modulation of a zero-bias peak in a hybrid nanowire-superconductor device," *Phys. Rev. Lett.*, vol. 110, p. 126406, 2013.

[96] H. O. H. Churchill, V. Fatemi, K. Grove-Rasmussen, M. T. Deng, P. Caroff, H. Q. Xu, and C. M. Marcus, "Superconductor-nanowire devices from tunneling to the multichannel regime: Zero-bias oscillations and magnetoconductance crossover," *Phys. Rev. B*, vol. 87, p. 241401, 2013.

[97] E. J. H. Lee, X. Jiang, M. Houzet, R. Aguado, C. M. Lieber, and S. De Franceschi, "Spin-resolved Andreev levels and parity crossings in hybrid superconductor-semiconductor nanostructures," *Nat Nano*, vol. 9, no. 1, p. 79, 2014.

[98] E. J. H. Lee, X. Jiang, R. Aguado, G. Katsaros, C. M. Lieber, and S. De Franceschi, "Zero-bias anomaly in a nanowire quantum dot coupled to superconductors," *Phys. Rev. Lett.*, vol. 109, p. 186802, 2012.

[99] J. Liu, A. C. Potter, K. T. Law, and P. A. Lee, "Zero-bias peaks in the tunneling conductance of spin-orbit-coupled superconducting wires with and without Majorana end-states," *Phys. Rev. Lett.*, vol. 109, p. 267002, 2012.

[100] D. Bagrets and A. Altland, "Class D spectral peak in Majorana quantum wires," *Phys. Rev. Lett.*, vol. 109, p. 227005, 2012.

[101] D. I. Pikulin, J. P. Dahlhaus, M. Wimmer, H. Schomerus, and C. W. J. Beenakker, "A zero-voltage conductance peak from weak antilocalization in a Majorana nanowire," *New Journal of Physics*, vol. 14, no. 12, p. 125011, 2012.

[102] P. Neven, D. Bagrets, and A. Altland, "Quasiclassical theory of disordered multichannel Majorana quantum wires," *New Journal of Physics*, vol. 15, no. 5, p. 055019, 2013.

[103] O. Motrunich, K. Damle, and D. A. Huse, "Griffiths effects and quantum critical points in dirty superconductors without spin-rotation invariance: One-dimensional examples," *Phys. Rev. B*, vol. 63, p. 224204, 2001.

[104] I. A. Gruzberg, N. Read, and S. Vishveshwara, "Localization in disordered superconducting wires with broken spin-rotation symmetry," *Phys. Rev. B*, vol. 71, p. 245124, 2005.

[105] A. R. Akhmerov, J. P. Dahlhaus, F. Hassler, M. Wimmer, and C. W. J. Beenakker, "Quantized conductance at the Majorana phase transition in a disordered superconducting wire," *Phys. Rev. Lett.*, vol. 106, p. 057001, 2011.

[106] A. C. Potter and P. A. Lee, "Engineering a $p + ip$ superconductor: Comparison of topological insulator and Rashba spin-orbit-coupled materials," *Phys. Rev. B*, vol. 83, p. 184520, 2011.

[107] A. C. Potter and P. A. Lee, "Erratum: Engineering a $p + ip$ superconductor: Comparison of topological insulator and Rashba spin-orbit-coupled materials [Phys. Rev. B 83, 184520 (2011)]," *Phys. Rev. B*, vol. 84, p. 059906, 2011.

[108] P. W. Brouwer, M. Duckheim, A. Romito, and F. von Oppen, "Topological superconducting phases in disordered quantum wires with strong spin-orbit coupling," *Phys. Rev. B*, vol. 84, p. 144526, 2011.

[109] P. W. Brouwer, M. Duckheim, A. Romito, and F. von Oppen, "Probability distribution of Majorana end-state energies in disordered wires," *Phys. Rev. Lett.*, vol. 107, p. 196804, 2011.

[110] J. D. Sau, S. Tewari, and S. Das Sarma, "Experimental and materials considerations for the topological superconducting state in electron- and hole-doped semiconductors: Searching for non-Abelian Majorana modes in 1D nanowires and 2D heterostructures," *Phys. Rev. B*, vol. 85, p. 064512, 2012.

[111] A. M. Lobos, R. M. Lutchyn, and S. Das Sarma, "Interplay of disorder and interaction in Majorana quantum wires," *Phys. Rev. Lett.*, vol. 109, p. 146403, 2012.

[112] F. Pientka, A. Romito, M. Duckheim, Y. Oreg, and F. von Oppen, "Signatures of topological phase transitions in mesoscopic superconducting rings," *New Journal of Physics*, vol. 15, no. 2, p. 025001, 2013.

[113] W. DeGottardi, D. Sen, and S. Vishveshwara, "Majorana fermions in superconducting 1D systems having periodic, quasiperiodic, and disordered potentials," *Phys. Rev. Lett.*, vol. 110, p. 146404, 2013.

[114] J. D. Sau and S. Das Sarma, "Density of states of disordered topological superconductor-semiconductor hybrid nanowires," *Phys. Rev. B*, vol. 88, p. 064506, 2013.

[115] M.-T. Rieder, P. W. Brouwer, and I. Adagideli, "Reentrant topological phase transitions in a disordered spinless superconducting wire," *Phys. Rev. B*, vol. 88, p. 060509, 2013.

[116] D. Chevallier, P. Simon, and C. Bena, "From Andreev bound states to Majorana fermions in topological wires on superconducting substrates: A story of mutation," *Phys. Rev. B*, vol. 88, p. 165401, 2013.

[117] W. DeGottardi, M. Thakurathi, S. Vishveshwara, and D. Sen, "Majorana fermions in superconducting wires: Effects of long-range hopping, broken time-reversal symmetry, and potential landscapes," *Phys. Rev. B*, vol. 88, p. 165111, 2013.

[118] P. Jacquod and M. Büttiker, "Signatures of Majorana fermions in hybrid normal-superconducting rings," *Phys. Rev. B*, vol. 88, p. 241409, 2013.

[119] H.-Y. Hui, J. D. Sau, and S. Das Sarma, "Generalized Eilenberger theory for majorana zero-mode-carrying disordered p-wave superconductors," *Phys. Rev. B*, vol. 90, p. 064516, 2014.

[120] F. Pientka, G. Kells, A. Romito, P. W. Brouwer, and F. von Oppen, "Enhanced zero-bias Majorana peak in the differential tunneling conductance of disordered multisubband quantum-wire/superconductor junctions," *Phys. Rev. Lett.*, vol. 109, p. 227006, 2012.

[121] I. van Weperen, S. R. Plissard, E. P. A. M. Bakkers, S. M. Frolov, and L. P. Kouwenhoven, "Quantized conductance in an InSb nanowire," *Nano Letters*, vol. 13, no. 2, p. 387, 2013. PMID: 23259576.

[122] J. Kammhuber, M. C. Cassidy, H. Zhang, O. Gül, F. Pei, M. W. A. de Moor, B. Nijholt, K. Watanabe, T. Taniguchi, D. Car, S. R. Plissard, E. P. A. M. Bakkers, and L. P. Kouwenhoven, "Conductance quantization at zero magnetic field in InSb nanowires," *Nano Letters*, vol. 16, no. 6, p. 3482, 2016. PMID: 27121534.

[123] H. Zhang, Ö. Gül, S. Conesa-Boj, K. Zuo, V. Mourik, F. K. de Vries, J. van Veen, D. J. van Woerkom, M. P. Nowak, M. Wimmer, D. Car, S. Plissard, E. P. A. M. Bakkers, M. Quintero-Pérez, S. Goswami, K. Watanabe, T. Taniguchi, and L. P. Kouwenhoven, "Ballistic Majorana nanowire devices," *arXiv* 1603.04069, 2016.

[124] P. De Gennes, *Superconductivity Of Metals And Alloys*. Advanced Books Classics, Westview Press, 1999.

[125] M.-T. Rieder, G. Kells, M. Duckheim, D. Meidan, and P. W. Brouwer, "Endstates in multichannel spinless p-wave superconducting wires," *Phys. Rev. B*, vol. 86, p. 125423, 2012.

[126] S. Tewari and J. D. Sau, "Topological invariants for spin-orbit coupled superconductor nanowires," *Phys. Rev. Lett.*, vol. 109, p. 150408, 2012.

[127] M. Diez, J. P. Dahlhaus, M. Wimmer, and C. W. J. Beenakker, "Andreev reflection from a topological superconductor with chiral symmetry," *Phys. Rev. B*, vol. 86, p. 094501, 2012.

[128] C. W. J. Beenakker, "Random-matrix theory of quantum transport," *Rev. Mod. Phys.*, vol. 69, p. 731, 1997.

[129] P. Mello and N. Kumar, *Quantum Transport in Mesoscopic Systems: Complexity and Statistical Fluctuations, a Maximum-entropy Viewpoint*. Mesoscopic physics and nanotechnology, Oxford: Oxford University Press, 2004.

[130] C. W. Groth, M. Wimmer, A. R. Akhmerov, and X. Waintal, "Kwant: A software package for quantum transport," *New Journal of Physics*, vol. 16, no. 6, p. 063065, 2014.

[131] C. W. J. Beenakker, J. M. Edge, J. P. Dahlhaus, D. I. Pikulin, S. Mi, and M. Wimmer, "Wigner-Poisson statistics of topological transitions in a Josephson junction," *Phys. Rev. Lett.*, vol. 111, p. 037001, 2013.

[132] B. M. Andersen, K. Flensberg, V. Koerting, and J. Paaske, "Nonequilibrium transport through a spinful quantum dot with superconducting leads," *Phys. Rev. Lett.*, vol. 107, p. 256802, 2011.

[133] K. T. Law and P. A. Lee, "Robustness of Majorana fermion induced fractional Josephson effect in multichannel superconducting wires," *Phys. Rev. B*, vol. 84, p. 081304, 2011.

[134] C. W. J. Beenakker, D. I. Pikulin, T. Hyart, H. Schomerus, and J. P. Dahlhaus, "Fermion-parity anomaly of the critical supercurrent in the quantum spin-Hall effect," *Phys. Rev. Lett.*, vol. 110, p. 017003, 2013.

[135] T. Yokoyama, M. Eto, and Y. V. Nazarov, "Josephson current through semiconductor nanowire with spin-orbit interaction in magnetic field," *Journal of the Physical Society of Japan*, vol. 82, no. 5, p. 054703, 2013.

[136] W. Chang, V. E. Manucharyan, T. S. Jespersen, J. Nygård, and C. M. Marcus, "Tunneling spectroscopy of quasiparticle bound states in a spinful Josephson junction," *Phys. Rev. Lett.*, vol. 110, p. 217005, 2013.

[137] J. D. Sau and E. Demler, "Bound states at impurities as a probe of topological superconductivity in nanowires," *Phys. Rev. B*, vol. 88, p. 205402, 2013.

[138] R. Ilan, J. H. Bardarson, H.-S. Sim, and J. E. Moore, "Detecting perfect transmission in Josephson junctions on the surface of three dimensional topological insulators," *New Journal of Physics*, vol. 16, no. 5, p. 053007, 2014.

[139] H. Weyl and K. Chandrasekharan, *Gesammelte Abhandlungen I.* No. v. 4 in Springer Collected Works in Mathematics, Springer Berlin Heidelberg, 1968.

[140] H. Baltes and E. Hilf, *Spectra of finite systems: A review of Weyl's problem, the eigenvalue distribution of the wave equation for finite domains and its applications on the physics of small systems*. Bibliographisches Institut, 1976.

[141] Å. Pleijel, "A study of certain Green's functions with applications in the theory of vibrating membranes," *Arkiv för matematik*, vol. 2, no. 6, p. 553, 1954.

[142] B. F. H., "Extended asymptotic eigenvalue distributions for bounded domain in n-space.," *J. Math. Mech.*, vol. 6, p. 119, 1957.

[143] R. Balian and C. Bloch, "Distribution of eigenfrequencies for the wave equation in a finite domain," *Annals of Physics*, vol. 60, no. 2, p. 401, 1970.

[144] E. P. Wigner, "Characteristic vectors of bordered matrices with infinite dimensions," *Annals of Mathematics*, vol. 62, no. 3, p. 548, 1955.

[145] F. J. Dyson, "The threefold way: Algebraic structure of symmetry groups and ensembles in quantum mechanics," *Journal of Mathematical Physics*, vol. 3, no. 6, p. 1199, 1962.

[146] M. Mehta, *Random Matrices*. Pure and Applied Mathematics, Elsevier Science, 2004.

[147] O. Bohigas, M. J. Giannoni, and C. Schmit, "Characterization of chaotic quantum spectra and universality of level fluctuation laws," *Phys. Rev. Lett.*, vol. 52, p. 1, 1984.

[148] O. Bohigas, M. Giannoni, and C. Schmit, "Spectral properties of the Laplacian and random matrix theories," *Journal de Physique Lettres*, vol. 45, no. 21, p. 1015, 1984.

[149] D. Waltner, *Semiclassical Approach to Mesoscopic Systems: Classical Trajectory Correlations and Wave Interference*. Springer Tracts in Modern Physics, Springer-Verlag Berlin Heidelberg: Springer Berlin Heidelberg, 2012.

[150] M. Gutzwiller, *Chaos in Classical and Quantum Mechanics*. Interdisciplinary Applied Mathematics, Springer-Verlag New York Inc.: Springer New York, 1991.

[151] L. D'Alessio, Y. Kafri, A. Polkovnikov, and M. Rigol, "From quantum chaos and eigenstate thermalization to statistical mechanics and thermodynamics," *Advances in Physics*, vol. 65, no. 3, p. 239, 2016.

[152] K. Richter and M. Sieber, "Semiclassical theory of chaotic quantum transport," *Phys. Rev. Lett.*, vol. 89, p. 206801, 2002.

[153] S. Das Sarma, J. D. Sau, and T. D. Stanescu, "Splitting of the zero-bias conductance peak as smoking gun evidence for the existence of the Majorana mode in a superconductor-semiconductor nanowire," *Phys. Rev. B*, vol. 86, p. 220506, 2012.

[154] E. Prada, P. San-Jose, and R. Aguado, "Transport spectroscopy of ns nanowire junctions with Majorana fermions," *Phys. Rev. B*, vol. 86, p. 180503, 2012.

[155] D. Rainis, L. Trifunovic, J. Klinovaja, and D. Loss, "Towards a realistic transport modeling in a superconducting nanowire with Majorana fermions," *Phys. Rev. B*, vol. 87, p. 024515, 2013.

[156] M. Kac, "Can one hear the shape of a drum?," *The American Mathematical Monthly*, vol. 73, no. 4, p. 1, 1966.

[157] R. Landauer, "Irreversibility and heat generation in the computing process," *IBM Journal of Research and Development*, vol. 5, no. 3, p. 183, 1961.

[158] C. H. Bennett, "The thermodynamics of computation—a review," *International Journal of Theoretical Physics*, vol. 21, no. 12, p. 905, 1982.

[159] K. Maruyama, F. Nori, and V. Vedral, "Colloquium: The physics of maxwell's demon and information," *Rev. Mod. Phys.*, vol. 81, p. 1, 2009.

[160] H. Leff and A. Rex, eds., *Maxwell's Demon 2: Entropy, Classical and Quantum Information, Computing*. Taylor & Francis, 2002.

[161] S. Lloyd, "Quantum-mechanical Maxwell's demon," *Phys. Rev. A*, vol. 56, p. 3374, 1997.

[162] M. O. Scully, "Extracting work from a single thermal bath via quantum negentropy," *Phys. Rev. Lett.*, vol. 87, p. 220601, 2001.

[163] T. D. Kieu, "The second law, Maxwell's demon, and work derivable from quantum heat engines," *Phys. Rev. Lett.*, vol. 93, p. 140403, 2004.

[164] S. Toyabe, T. Sagawa, M. Ueda, E. Muneyuki, and M. Sano, "Experimental demonstration of information-to-energy conversion and validation of the generalized Jarzynski equality," *Nature Physics*, vol. 6, no. 12, p. 988, 2010.

[165] A. Berut, A. Arakelyan, A. Petrosyan, S. Ciliberto, R. Dillenschneider, and E. Lutz, "Experimental verification of Landauer's principle linking information and thermodynamics," *Nature*, vol. 483, no. 7388, p. 187, 2012.

[166] E. Roldán, I. A. Martínez, J. M. R. Parrondo, and D. Petrov, "Universal features in the energetics of symmetry breaking," *Nat Phys*, vol. 10, no. 6, p. 457, 2014.

[167] M. D. Vidrighin, O. Dahlsten, M. Barbieri, M. S. Kim, V. Vedral, and I. A. Walmsley, "Photonic Maxwell's demon," *Phys. Rev. Lett.*, vol. 116, p. 050401, 2016.

[168] M. A. Ciampini, L. Mancino, A. Orieux, C. Vigliar, P. Mataloni, M. Paternostro, and M. Barbieri, "Experimental extractable work-based multipartite separability criteria," *NPJ Quantum Information*, vol. 3, no. 1, p. 10, 2017.

[169] P. A. Camati, J. P. S. Peterson, T. B. Batalhão, K. Micadei, A. M. Souza, R. S. Sarthour, I. S. Oliveira, and R. M. Serra, "Experimental rectification of entropy production by Maxwell's demon in a quantum system," *Phys. Rev. Lett.*, vol. 117, p. 240502, 2016.

[170] J. P. S. Peterson, R. S. Sarthour, A. M. Souza, I. S. Oliveira, J. Goold, K. Modi, D. O. Soares-Pinto, and L. C. Céleri, "Experimental demonstration of information to energy conversion in a quantum system at the Landauer limit," *Proceedings of the Royal Society of London A: Mathematical, Physical and Engineering Sciences*, vol. 472, no. 2188, 2016.

[171] J. V. Koski, V. F. Maisi, T. Sagawa, and J. P. Pekola, "Experimental observation of the role of mutual information in the nonequilibrium dynamics of a Maxwell demon," *Phys. Rev. Lett.*, vol. 113, p. 030601, 2014.

[172] J. V. Koski, V. F. Maisi, J. P. Pekola, and D. V. Averin, "Experimental realization of a szilard engine with a single electron," *Proceedings of the National Academy of Sciences*, vol. 111, no. 38, p. 13786, 2014.

[173] J. V. Koski, A. Kutvonen, I. M. Khaymovich, T. Ala-Nissila, and J. P. Pekola, "On-chip Maxwell's demon as an information-powered refrigerator," *Phys. Rev. Lett.*, vol. 115, p. 260602, 2015.

[174] N. Cottet, S. Jezouin, L. Bretheau, P. Campagne-Ibarcq, Q. Ficheux, J. Anders, A. Auffèves, R. Azouit, P. Rouchon, and B. Huard, "Observing a quantum Maxwell demon at work," *arXiv* 1702.05161, 2017.

[175] S. Hilt, S. Shabbir, J. Anders, and E. Lutz, "Landauer's principle in the quantum regime," *Phys. Rev. E*, vol. 83, p. 030102, 2011.

[176] D. Mandal, H. T. Quan, and C. Jarzynski, "Maxwell's refrigerator: An exactly solvable model," *Phys. Rev. Lett.*, vol. 111, p. 030602, 2013.

[177] A. C. Barato and U. Seifert, "An autonomous and reversible Maxwell's demon," *Europhysics Letters*, vol. 101, no. 6, p. 60001, 2013.

[178] P. Strasberg, G. Schaller, T. Brandes, and M. Esposito, "Thermodynamics of a physical model implementing a Maxwell demon," *Phys. Rev. Lett.*, vol. 110, p. 040601, 2013.

[179] J. M. Horowitz, T. Sagawa, and J. M. R. Parrondo, "Imitating chemical motors with optimal information motors," *Phys. Rev. Lett.*, vol. 111, p. 010602, 2013.

[180] S. Deffner, "Information-driven current in a quantum Maxwell demon," *Phys. Rev. E*, vol. 88, p. 062128, 2013.

[181] J. J. Park, K.-H. Kim, T. Sagawa, and S. W. Kim, "Heat engine driven by purely quantum information," *Phys. Rev. Lett.*, vol. 111, p. 230402, 2013.

[182] J. Roßnagel, O. Abah, F. Schmidt-Kaler, K. Singer, and E. Lutz, "Nanoscale heat engine beyond the carnot limit," *Phys. Rev. Lett.*, vol. 112, p. 030602, 2014.

[183] J. Gemmer and J. Anders, "From single-shot towards general work extraction in a quantum thermodynamic framework," *New Journal of Physics*, vol. 17, no. 8, p. 085006, 2015.

[184] J. P. Pekola, D. S. Golubev, and D. V. Averin, "Maxwell's demon based on a single qubit," *Phys. Rev. B*, vol. 93, p. 024501, 2016.

[185] A. Kutvonen, J. Koski, and T. Ala-Nissila, "Thermodynamics and efficiency of an autonomous on-chip Maxwell's demon," *Scientific Reports*, vol. 6, p. 21126, 2016.

[186] M. Campisi, J. Pekola, and R. Fazio, "Feedback-controlled heat transport in quantum devices: Theory and solid-state experimental proposal," *New Journal of Physics*, vol. 19, no. 5, p. 053027, 2017.

[187] C. Elouard, D. Herrera-Martí, B. Huard, and A. Auffèves, "Extracting work from quantum measurement in Maxwell demon engines," *arXiv* 1702.01917, 2017.

[188] G. Rosselló, R. López, and G. Platero, "A chiral Maxwell Demon," *arXiv* 1703.03221, 2017.

[189] M. König, H. Buhmann, L. W. Molenkamp, T. Hughes, C.-X. Liu, X.-L. Qi, and S.-C. Zhang, "The quantum spin Hall effect: Theory and experiment," *Journal of the Physical Society of Japan*, vol. 77, no. 3, p. 031007, 2008.

[190] L. Du, I. Knez, G. Sullivan, and R.-R. Du, "Robust helical edge transport in gated $\mathrm{InAs/GaSb}$ bilayers," *Phys. Rev. Lett.*, vol. 114, p. 096802, 2015.

[191] A. M. Lunde and G. Platero, "Helical edge states coupled to a spin bath: Current-induced magnetization," *Phys. Rev. B*, vol. 86, p. 035112, 2012.

[192] V. Cheianov and L. I. Glazman, "Mesoscopic fluctuations of conductance of a helical edge contaminated by magnetic impurities," *Phys. Rev. Lett.*, vol. 110, p. 206803, 2013.

[193] A. Del Maestro, T. Hyart, and B. Rosenow, "Backscattering between helical edge states via dynamic nuclear polarization," *Phys. Rev. B*, vol. 87, p. 165440, 2013.

[194] L. Kimme, B. Rosenow, and A. Brataas, "Backscattering in helical edge states from a magnetic impurity and Rashba disorder," *Phys. Rev. B*, vol. 93, p. 081301, 2016.

[195] C.-H. Hsu, P. Stano, J. Klinovaja, and D. Loss, "Nuclear spin-induced localization of the edge states in two-dimensional topological insulators," *arXiv* 1703.03421, 2017.

[196] I. Adagideli, V. Lutsker, M. Scheid, P. Jacquod, and K. Richter, "Spin transistor action from hidden Onsager reciprocity," *Phys. Rev. Lett.*, vol. 108, p. 236601, 2012.

[197] C. Slichter, *Principles of Magnetic Resonance*. Springer Series in Solid-State Sciences, Springer Berlin Heidelberg, 1996.

[198] R. I. Dzhioev and V. L. Korenev, "Stabilization of the electron-nuclear spin orientation in quantum dots by the nuclear quadrupole interaction," *Phys. Rev. Lett.*, vol. 99, p. 037401, 2007.

[199] S. Datta and B. Das, "Electronic analog of the electro-optic modulator," *Applied Physics Letters*, vol. 56, no. 7, p. 665, 1990.

[200] G. Schmidt, D. Ferrand, L. W. Molenkamp, A. T. Filip, and B. J. van Wees, "Fundamental obstacle for electrical spin injection from a ferromagnetic metal into a diffusive semiconductor," *Phys. Rev. B*, vol. 62, p. R4790, 2000.

[201] J. Tian, S. Hong, I. Miotkowski, S. Datta, and Y. P. Chen, "Observation of current-induced, long-lived persistent spin polarization in a topological insulator: A rechargeable spin battery," *Science Advances*, vol. 3, no. 4, 2017.

[202] S.-Y. Xu, L. A. Wray, Y. Xia, R. Shankar, A. Petersen, A. Fedorov, H. Lin, A. Bansil, Y. S. Hor, D. Grauer, R. J. Cava, and M. Z. Hasan, "Discovery of several large families of topological insulator classes with backscattering-suppressed spin-polarized single-Dirac-cone on the surface," *arXiv* 1007.5111, 2010.

[203] A. M. Lunde and G. Platero, "Hyperfine interactions in two-dimensional HgTe topological insulators," *Phys. Rev. B*, vol. 88, p. 115411, 2013.

[204] D. Tong, "Kinetic theory." Lecture notes obtained from webpage at http://www.damtp.cam.ac.uk/user/tong/kinetic.html, Accessed 26.06.2017, 2012.

[205] W. Tan, L. Chen, X. Ji, and H.-Q. Lin, "Photonic simulation of topological superconductor edge state and zero-energy mode at a vortex," *Scientific Reports*, vol. 4, p. 7381, 2014.

[206] L. Lu, J. D. Joannopoulos, and M. Soljacic, "Topological photonics," *Nat Photon*, vol. 8, no. 11, p. 821, 2014.

[207] D. G. Rothe, R. W. Reinthaler, C.-X. Liu, L. W. Molenkamp, S.-C. Zhang, and E. M. Hankiewicz, "Fingerprint of different spin-orbit terms for spin transport in HgTe quantum wells," *New Journal of Physics*, vol. 12, no. 6, p. 065012, 2010.

Appendix A

INTEGER QUANTUM HALL EFFECT: LAUGHLIN ARGUMENT AND TKNN INVARIANT

The experimental discovery of the quantization of Hall conductance in a 2D electron gas (2DEG) by von Klitzing, Dorda and Pepper [4] lead the way to extremely precise calibration of resistance measurement and to the determination of the fine structure constant using what is now dubbed the von Klitzing constant ($R_K = h/e^2 = 25812.807557(18)\Omega$), and it lead to the modern interest in the study of topological insulators. Von Klitzing received the 1985 Nobel prize in Physics for this discovery. The theoretical explanation for the precise nature of the quantization was achieved by Laughlin [5] and by Thouless, Kohmoto, Nightingale and den Nijs [6].

The classical Hall effect is due to the Lorentz force felt by the moving charges in a conductor under a magnetic field. In a 2D conducting system, when charges are driven via an electric field in one direction and a magnetic field perpendicular to the plane of the conductor is applied, there will be a resulting Lorentz force, creating a voltage gradient within the conductor *perpendicular to* the direction of the current. A simple hand-waving picture for QHE involves the "skipping orbits" argument, which serves to motivate the idea of a quantized edge conductance, but obscures the topological reasoning underlying the Landau levels. Under a strong magnetic field, the electrons will move in closed orbits, each allowing a single magnetic flux quantum. The electrons move around these orbits in a given direction determined by the magnetic field direction. When the electron hits an edge, it has to move along further along the edge as it cannot backscatter due to this given direction. Hence we have the edge states: we have the skipping motion of cyclotron orbits at the edges. This motion is *chiral* in the sense that they only propagate in one direction along the edge, determined by the direction of the magnetic field. These states are protected against disorder because there is no quantum state they can backscatter into, for a sample wide enough (or a magnetic field strong enough) so that the opposite edges carrying current in opposite directions are well separated (see Figure A.1).

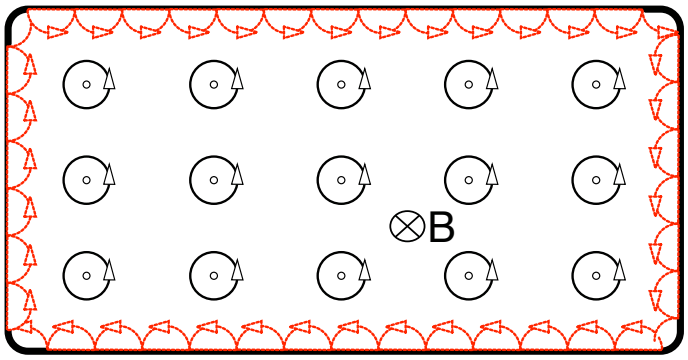

Figure A.1: The orbits of electrons in a quantum Hall system under an applied magnetic field. The closed cyclotron orbits form the Landau levels. At the edges, a chiral state travels in a single direction, determined by the direction of the magnetic field B. These "skipping orbits" in this cartoon picture are shown in red.

We start describing the topological nature of the underlying cause of QHE by outlining Laughlin's charge-pumping argument [5, 7]. Laughlin considers a metallic strip, formed into a cylinder, with a current due to an electric field flowing along the cylinder. Laughlin then applies a magnetic field piercing this cylinder outward perpendicularly, and considers the resulting Hall voltage across the top and bottom edges of the cylinder as in Figure A.2. This picture simply ensures periodic boundary conditions in a 2DEG along the direction of current. The Hall current is related to the drift velocity, which is proportional to the derivative of the electronic potential with respect to the total magnetic flux through the strip, where the magnetic flux is changed adiabatically:

$$\begin{aligned} I &= c\frac{\partial U}{\partial \phi} \\ &= \frac{c}{L}\frac{\partial U}{\partial A} \end{aligned} \tag{A.1}$$

where L is the length of the strip along the current and A is the vector potential. This is due to the presence of a gauge choice in which $k_\theta \rightarrow k_\theta + eA/c$, meaning a derivative with respect to k_θ yielding the drift velocity along the θ direction can be written as a derivative with respect to A or with respect to the total flux ϕ. Localized states, if any, are not affected by insertion of a magnetic flux and the only states affected are extended states, phase coherent across the sample. This insertion of the flux will change the phase of all wavefunctions by $e^{\frac{ieAx}{\hbar c}} = e^{\frac{i2\pi Ax}{\phi_0}}$ with $\phi_0 = h/e$ is the flux quantum and x is the coordinate along the side of the cylinder. For this gauge transformation to be possible for extended states (for the wavefunctions to be single valued), we must have

$$A = n\frac{c\phi_0}{L} \tag{A.2}$$

with $n \in \mathbb{Z}$. Such a gauge transformation would mean the shifting of the center of

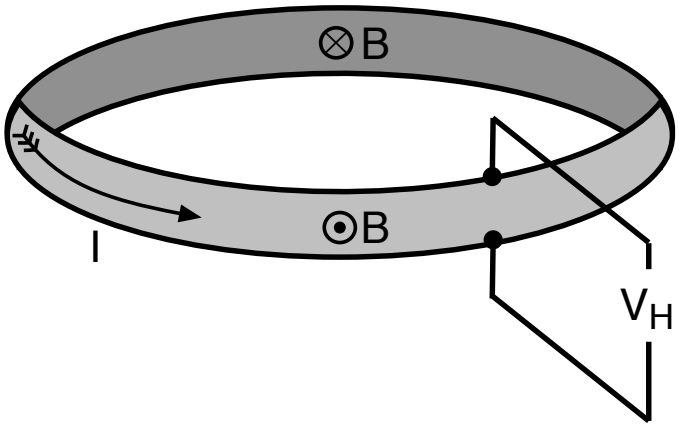

Figure A.2: The QHE cylinder used by Laughlin to make his argument. A magnetic field pierces the sides of the cylinder in a perpendicular fashion. Current is applied around the sides, and a Hall voltage V_H is observed. Under sufficiently strong magnetic fields, the conductance I/V_H is quantized as a function of magnetic field.

the Landau level wavefunction solutions by $y_0 \to y_0 - \alpha(\Delta A)/H$ whereas the energies change linearly with A, with y_0 being the center of the wavefunction along the y-direction (within the 2DEG plane, perpendicular to the current) and α is just a constant depending on the units of measurement of the magnetic field H. Going back to Eq. A.1, a flux insertion results in a transfer of charge from one edge to the other, with a conductivity $I/V = ne^2/h$ with n an integer, and a shifting of the state towards the edge.

We now discuss the TKNN (Thouless, Kohmoto, Nightingale and den Nijs) invariant [6]. Following Kohmoto's 1985 paper [7] we briefly outline the topological protection and integer quantization, using the concepts outlined in the previous subsections. (For a more detailed introduction, we refer the reader to, for example, References [15, 22, 23, 34].)

Considering the Kubo formula for conductance within a crystal which has a rectangular lattice with lattice constants a and b, the Hamiltonian and the Bloch wavefunctions are written as:

$$H = \frac{\hbar^2}{2m^*}\left(\mathbf{p} - e\mathbf{A}c\right)^2 + U(x,y), \tag{A.3}$$

with $T_x(a)U(x,y)T_x^{-1}(a) = T_y(b)U(x,y)T_y^{-1}(b) = U(x,y)$ where $T_x(a)$ ($T_y(b)$) is the translation operator along the x (y) direction by an amount a (b). They choose the flux through a unit cell $\phi = abeB/h$ to be a rational multiple of the flux quantum $\phi = p/q\phi_0$ with p, q prime. With a magnetic field in the z-direction and the choice of the gauge as the Landau gauge ($A = (0, eBx, 0)$), the eigenfunctions satisfy the following generalized Bloch condition:

$$\psi_{k_x,k_y}(x,y) = \psi_{k_x,k_y}(x+qa,y)e^{-2\pi iy/b - ik_x qa}$$

$$\psi_{k_x,k_y}(x,y) = \psi_{k_x,k_y}(x,y_b)e^{-ik_y b} \tag{A.4}$$

with k_x, k_y vectors in the Brillouin zone. This form of the Bloch condition uses the *magnetic unit cell* (Figure A.3), which is q unit cells stacked side by side along the x-direction with an integer number (p) of flux quanta passing through them. The corresponding Bloch wavefunctions are given by $u_{k_x,k_y}(x,y) = \psi_{k_x,k_y}(x,y)e^{-ik_x x - ik_y y}$ with the Hamiltonian

$$H(k_x,k_y) = \frac{1}{2m}\left(-i\hbar\partial_x + \hbar k_x\right)^2 + \frac{1}{2m}\left(-i\hbar\partial_y + \hbar k_y - eBx\right)^2 + U(x,y). \tag{A.5}$$

This Hamiltonian has the form of Eq. 2.2 with $\xi = (k_x, k_y)$. Applying the Kubo formula using this Hamiltonian (see Appendix B), Thouless *et al.* arrive at the following expression for Hall conductivity:

$$\begin{aligned}\sigma_{xy}^H &= \frac{ie}{2\pi\phi_0}\sigma \int d^2k \int d^2r \left(\partial_{k_x}u^*\partial_{k_y}u - \partial_{k_y}u^*\partial_{k_x}u\right) \\ &= \frac{ie}{4\pi\phi_0}\sigma \oint dk_\alpha \int d^2r \left(u^*(\partial_{k_\alpha}u) - (\partial_{k_\alpha}u^*)u\right).\end{aligned} \tag{A.6}$$

The second line above is due to Stokes' theorem: Consider the vector field $\mathbf{A}(k_x,k_y) = \langle u_{k_x,k_y}(x,y)|\nabla_{\mathbf{k}}|u_{k_x,k_y}(x,y)\rangle$ where the expectation value is taken over the unit cell. We then see that the integrand in the first line is simply the z-component of $\nabla_{\mathbf{k}} \times \mathbf{A}(k_x,k_y)$, integrated over the "magnetic Brillouin zone": $k_x \in [0, 2\pi/qa]$ and $k_y \in [2\pi/b]$. The similarity to Eq. 2.5 is now apparent: $\mathbf{A}$ is the Berry connection. We also note that the integral in the second line is taken over a torus T^2. If $\mathbf{A}(k_x,k_y)$ is uniquely defined over all of the torus, then the only nonzero result can come from the boundaries of the surface, and the torus has none. Therefore for a nonzero result, there must be some problematic points in the definition of the connection.

We now emphasize the common source of this equation and the Berry connection [7]. The argument for the quantization of Hall conductivity is essentially the same argument we outline in Subsection 2.1.3.

We first show that the Bloch wavefunctions must have at least one zero in the magnetic Brillouin zone, a result which we need in the following argument. While the Hamiltonian for zero magnetic field commutes with the translation operator if the translation is by a Bravais vector, this is not the case in general for nonzero magnetic field. He defines a magnetic translation operator in which the usual $\mathbf{p}$ is now written as the canonical momentum as usual, with $\mathbf{p} \to \mathbf{p} - e\mathbf{A}/c$ and $\mathbf{T_x} \to \exp i/\hbar(\mathbf{p} - e\mathbf{A}/c)\mathbf{x}$. In this form, translation from one corner of the (rectangular) unit cell to an opposite corner via two different paths does not yield the same result: $[\mathbf{T}_a, \mathbf{T}_b] = 1 - \exp 2\pi i\phi/\phi_0$ with $\phi = Bab$ being the flux through the unit cell. However, if one considers a rational value for $\phi/\phi_0 = p/q$

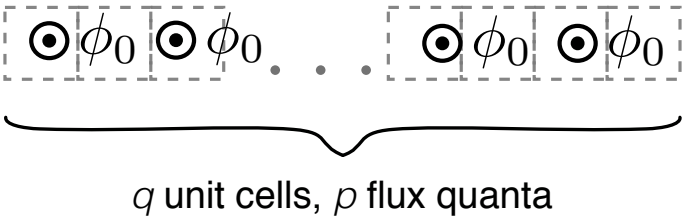

Figure A.3: q unit cells of size $a \times b$, admitting a total of p flux quanta ϕ_0. If p and q are mutually prime, then this figure depicts a magnetic unit cell.

as before (p, q prime) and extends the unit cell by stacking q unit cells side by side, the translation operators over the two different paths from one corner on this "magnetic unit cell" to another commute (see Figure A.3). When a gauge transformation $\mathbf{A} \to \mathbf{A} + \nabla f$ is performed, there is an accompanying phase change on a wavefunction $\psi \to e^{ie/\hbar f}\psi$, but this cannot change the overall phase gain around the magnetic unit cell. If we consider $u = |u|e^{i\theta_{k_x,k_y}(x,y)}$, we must have

$$p = \frac{-1}{2\pi} \oint d\mathbf{l}\, \frac{\partial}{\partial \mathbf{l}} \theta_{k_x,k_y}(x,y) \tag{A.7}$$

an integer (prime, with our choice of the magnetic unit cell) where the integral is over the boundary of the magnetic unit cell. As we discussed, even though θ is gauge-dependent, this integral is gauge-invariant.

We now consider the direction of the unit vector along u in the complex u-space. The integral above shows this rotates around the origin p times when we travel along the magnetic unit cell boundary (see Figure A.4). This number is independent of the potential and is a topological invariant. Moreover, at the center of this rotation, the vector u must be zero. This concludes the argument that u must have a zero within the magnetic unit cell for some k_x and k_y.

We next perform a gauge transformation $u_{k_x,k_y}(x,y) \to u_{k_x,k_y}(x,y)e^{if(k_x,k_y)}$ with f a smooth function of k_i. Physical observables are unchanged by this operation. The corresponding transformation on $\mathbf{A}$ is $\mathbf{A} \to \mathbf{A} + \nabla_{k_x,k_y} f$, which does not change the Hall conductance, as expected. However, this means one can choose the phase of each $|u_{k_x,k_y}\rangle$ for a given k_x, k_y arbitrarily. Without loss of generality, we fix the phase by requiring $\mathrm{Im}\,\langle x_0, y_0|u_{k_x,k_y}\rangle = 0$. This is not enough to fix the phase everywhere, however, as u_{k_x,k_y} must be zero for some k_x, k_y in the magnetic Brillouin zone as we saw above. Consider the case of having a single zero. Divide the torus into two parts (see Figure A.5), one containing this zero (H_{I}) and one not (H_{II}), with their intersection (boundaries) a curve on the torus. We fix the phases separately in these regions, for example, by requiring that u in H_{I} evaluated at $(x_1, y_1) \neq (x_0, y_0)$ is always real and nonzero. This is sufficient to fix the overall phase everywhere on the torus. We also note that while the phase of

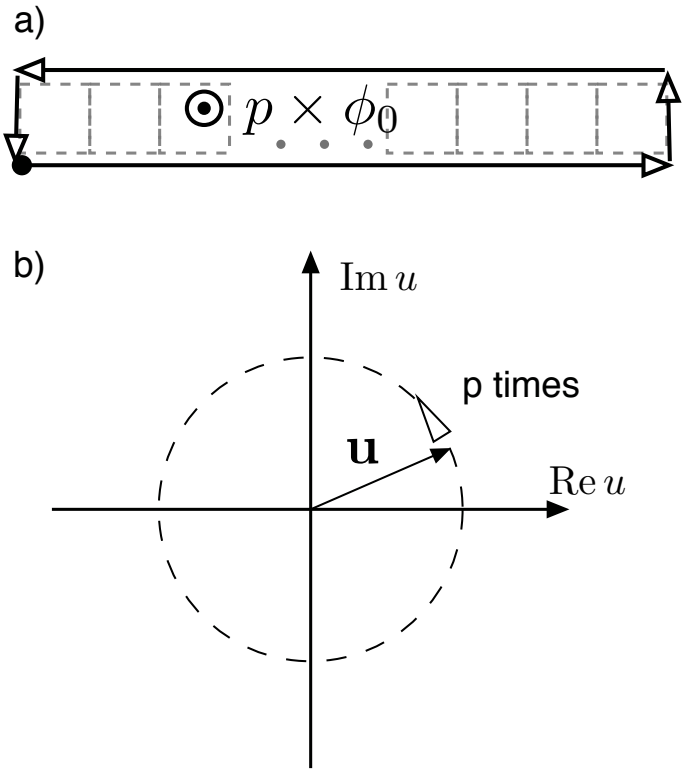

Figure A.4: As one goes around the magnetic unit cell containing q lattice unit cells and p flux quanta (a), the vector $\mathbf{u}$ makes p full revolutions in the complex plane (b).

$u_{k_x,k_y}(x,y) = \langle x,y|u_{k_x,k_y}\rangle$ is indeterminate at the point where u vanishes, the phase of the ket $|u_{k_x,k_y}\rangle$ is well defined at that point.

As one goes across the border ∂H, there is a (possibly abrupt) phase change:

$$|u_{\mathrm{II}}\rangle\Big|_{k_x,k_y\in\partial H} = e^{i\chi(k_x,k_y)}\,|u_{\mathrm{I}}\rangle\Big|_{k_x,k_y\in\partial H}. \tag{A.8}$$

This phase change χ can be (in fact, must be at some points) abrupt across ∂H, but it must be smooth along ∂H considering u must be smooth within each of the regions near the boundaries. As the connection $\mathbf{A}$ can be defined using these state vectors (see Eq. A.6), on the boundary ∂H, we must have

$$\mathbf{A}_{\mathrm{II}} = \mathbf{A}_{\mathrm{I}} + i\nabla_{k_x,k_y}\chi(k_x,k_y). \tag{A.9}$$

The integral in Eq. A.6 for Hall conductance contains an integral over the magnetic Brillouin zone. We separate this integral into two, just as we did in describing the general Chern number, and each part of the surface has a boundary. The Stokes theorem is applied in this boundary, however, the direction of travel along the boundary curve is opposite in each part of the integral:

$$\sigma^{\mathrm{H}}_{xy} = \frac{-ie^2}{\hbar}\left(\int_{H_{\mathrm{I}}} d^2k\,\nabla_k\mathbf{A}_{\mathrm{I}} + \int_{H_{\mathrm{II}}} d^2k\,\nabla_k\mathbf{A}_{\mathrm{II}}\right)$$

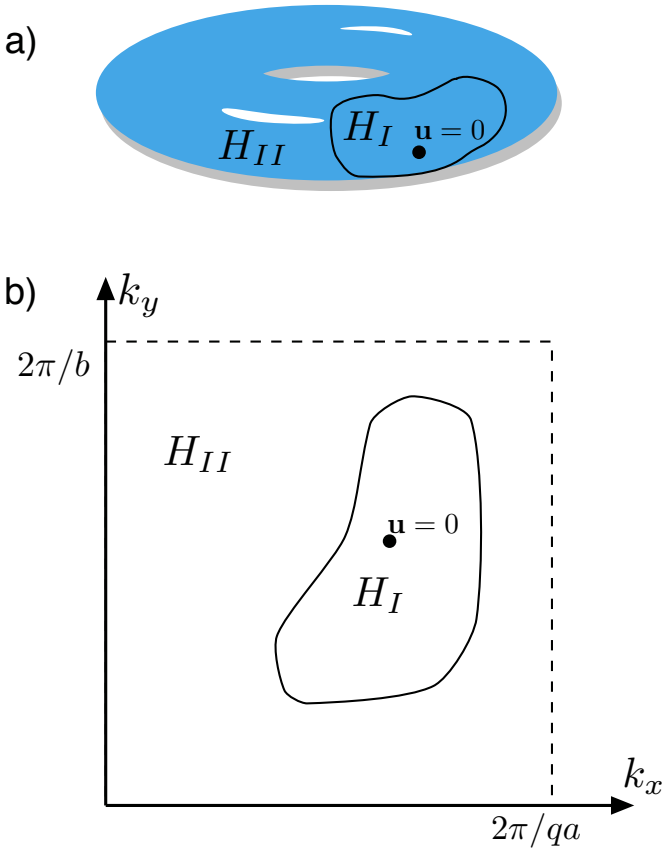

Figure A.5: The T_2 torus (a) of the magnetic unit cell in the corresponding Brillouin zone (b). The Brillouin zone is divided into two parts, H_I and H_{II}, the first of which contains a zero point of $\mathbf{u}$.

$$= \frac{-ie^2}{\hbar} \oint_{\partial H} (\mathbf{A}_{\mathrm{I}} - \mathbf{A}_{\mathrm{II}})$$
$$= \frac{e^2}{h} n \tag{A.10}$$

where $2\pi n = \oint_{\partial H} d\mathbf{k} \nabla_k \chi(k_x, k_y)$. As we discussed, χ must vary continuously (in fact, smoothly) along ∂H. This implies, for the wavefunctions to be single-valued, $n \in \mathbb{Z}$.

Finally, we note that in Eq. B.4 in the Appendix, the sum over energies up to the Fermi level indicates that the Chern number n in Eq. A.10 is the sum of all n's obtained for all the occupied levels. Another point is that the bulk-boundary correspondence can be explained by the Chern number. The difference between the Chern numbers calculated for two physical regions cannot change; as such, the difference between the Chern numbers calculated for the bulk of a quantum Hall insulator and the vacuum beyond its boundaries (which always yields 0) cannot change—unless the properties we assumed for our discussion change. This is the repetition of the *bulk-boundary correspondence* argument presented previously in this chapter. Therefore, at some point near the edge of a quantum Hall insulator, the "insulator" property must disappear and we must have conducting edge states. This is again the *bulk-boundary correspondence* argument presented previously in this chapter.

Appendix B

KUBO FORMULA AND TKNN INVARIANT

In this appendix, we outline the derivation of Eq. A.6 using the Kubo formula [204]. We follow the TKNN paper [6].

We first briefly derive the form of the Kubo formula used in the TKNN paper. We work within the Heisenberg picture and consider a Hamiltonian which is a function of the observables of the system, $H \rightarrow H(\{\mathcal{O}\})$, where $\{\mathcal{O}\} \rightarrow \{\mathcal{O}(t)\}$ is the set of operators representing the i^{th} observable. We then apply a perturbation using a subset of the observables: $H_s = \sum_i \varphi_i(t)\mathcal{O}_i(t)$ with φ_i being the sources. Using the time evolution operator $U(t,t_0) = \mathcal{T}\exp -i\int_{t_0}^{t} H_s(t')dt'$ with $\mathcal{T}$ as the time-ordering operator to switch to the interaction picture, we write the time evolution of the wavefunctions as $|\Psi(t)\rangle_I = U(t,t_0)\,|\Psi(t)\rangle_0$. We evolve the corresponding density matrix from its value ρ_0 at $t_0 \rightarrow -\infty$ when the sources were absent ($\varphi(t \rightarrow -\infty) \rightarrow 0$) to $\rho(t) = U(t)\rho_0 U^{-1}(t)$. To first order in the sources, the change in the expectation value of $\mathcal{O}_i$, $\delta\langle\mathcal{O}_i\rangle$, is given by

$$\begin{aligned}
\delta\langle\mathcal{O}_i\rangle &= \langle\mathcal{O}_i\rangle_\varphi - \langle\mathcal{O}_i\rangle_{\varphi=0} \\
&= \mathrm{Tr}\rho(t)\mathcal{O}_i(t) - \mathrm{Tr}\rho_0(t)\mathcal{O}_i(t) \\
&= i\sum_j \int_{-\infty}^{\infty} dt'\theta(t-t')\,\varphi_j(t)\;\langle[\mathcal{O}_j(t),\mathcal{O}_i(t)]\rangle\,. \qquad \text{(B.1)}
\end{aligned}$$

We then read off the susceptibility from the last line in the above equation as $\chi_{ij} = -i\theta(t-t')\,\varphi_j(t)\;\langle[\mathcal{O}_j(t),\mathcal{O}_i(t)]\rangle$. We then take the Fourier transform to obtain the spectral decomposition, and work within the canonical ensemble for electrons and set $\rho = f(H)$ with $f(E)$ being the Fermi-Dirac distribution:

$$\begin{aligned}
\chi_{ij}(\omega) &= -i\int_0^\infty dt e^{i\omega t}\mathrm{Tr}f(H)\,\langle[\mathcal{O}_j(t),\mathcal{O}_i(t)]\rangle \\
&= -i\sum_{\alpha\beta}\int_0^\infty dt e^{i\omega t} f(\hbar\omega_\alpha)\left(e^{-i(\omega_\alpha-\omega_\beta)t}\,\langle\alpha|\mathcal{O}_i|\beta\rangle\,\langle\beta|\mathcal{O}_j|\alpha\rangle + \text{c.c.}\right) \qquad \text{(B.2)}
\end{aligned}$$

Here, ω_α (ω_β) are the eigenenergies corresponding to eigenkets ($|\alpha\rangle$) ($|\beta\rangle$). To assure

causality, we take $\omega \to \omega + i\epsilon$ and arrive at

$$\chi_{\alpha\beta}(\omega + i\epsilon) = \sum_{\alpha\beta} \frac{(\mathcal{O}_i)_{\alpha\beta}(\mathcal{O}_j)_{\beta\alpha}}{\omega_\alpha - \omega_\beta + \omega + i\epsilon} \left(f(\hbar\omega_\alpha) - f(\hbar\omega_\beta)\right) \tag{B.3}$$

Now, to derive the "susceptibility" of current to voltage, i.e. the Hall conductivity σ^H_{xy}, we take the operators $\mathcal{O}_i$ as the velocity operators $v_{x,y} = \partial H/\partial k_{x,y}$. We expand the denominator in Eq. B.3 up to second order in ω. For the DC response, we take $\omega \to 0$, but the zeroth order term vanishes and the ω^1 term is the first non-vanishing term. Taking the zero temperature limit, the Fermi-Dirac distributions become step functions at the Fermi level. We thus arrive at Eq. 4 of the TKNN paper, in the form later presented by Kohmoto [7]:

$$\sigma^H_{xy} = -ie^2\hbar \sum_{\epsilon_\alpha < \epsilon_F} \sum_{\epsilon_\beta < \epsilon_F} \frac{(v_y)_{\alpha\beta}(v_x)_{\beta\alpha} - (v_x)_{\alpha\beta}(v_y)_{\beta\alpha}}{(\epsilon_\alpha - \epsilon_\beta)^2}. \tag{B.4}$$

Rewriting this in terms of the Bloch wavefunctions, TKNN arrive at the following, which is Eq. 5 in their paper (see Eq. A.6):

$$\begin{aligned} \sigma^H_{xy} &= \frac{ie}{2\pi\phi_0}\sigma \int d^2k \int d^2r \left(\partial_{k_x} u^* \partial_{k_y} u - \partial_{k_y} u^* \partial_{k_x} u\right) \\ &= \frac{ie}{4\pi\phi_0}\sigma \oint dk_\alpha \int d^2r \left(u^*(\partial_{k_\alpha} u) - (\partial_{k_\alpha} u^*)u\right) \end{aligned} \tag{B.5}$$

Appendix C

MEAN FREE PATH

We consider a long wire along the x-axis, having a length of L along the x-direction and a width of W along the y-direction and metallic leads at the end, with a Gaussian disorder of the form $\langle V(\mathbf{r})\, V(\mathbf{r}')\rangle = \gamma\, \delta(\mathbf{r}-\mathbf{r}')$. We obtain the ensemble average of the matrix element between the n^{th} and l^{th} transverse channels as $\boldsymbol{k}(k_x, n) \rightarrow \boldsymbol{k}'(k'_x, l)$ as

$$\left\langle |V_{kk'}|^2 \right\rangle = \frac{\gamma}{LW}\left(1+\frac{\delta_{n,l}}{2}\right). \tag{C.1}$$

We then use Fermi's Golden Rule to calculate the inverse lifetime of a momentum state k, $\tau^{-1}_{k\rightarrow k'}$:

$$\left\langle l^{-1}_{\text{MFP}(k_x, n\rightarrow k'_x, l)} \right\rangle = \left(\frac{1}{\hbar}\frac{\partial\, \varepsilon_k}{\partial k_x}\right)^{-1} \times \frac{2\pi}{\hbar}\,\frac{\gamma}{LW} \times \left(1+\frac{\delta_{n,l}}{2}\right)\, \rho(\varepsilon_{k'}). \tag{C.2}$$

where ε_k gives the dispersion relation and $\rho(\varepsilon_k)$ is the density of states. We then sum over the initial and final states k' in Eq. (C.2) to obtain the total inverse MFP:

$$\left\langle l^{-1}_{\text{MFP}} \right\rangle = \sum_{k_x, k_y; k'_x, k'_y} \left\langle l^{-1}_{\text{MFP}(k_x, n\rightarrow k'_x, l)} \right\rangle \tag{C.3}$$

We first apply Eq. (C.3) to a free electron dispersion of the form $\varepsilon(k) = \hbar^2 k^2/2m = \hbar^2/2m\,(k^2_{n,x} + n^2\pi^2/W^2)$ for $n \in 1, \ldots, \bar{N}$ where $\bar{N}(\mu_{\text{eff}}) = \lfloor W k_F(\varepsilon)/\pi \rfloor$. The resulting total ensemble-averaged inverse MFP is

$$\begin{aligned}\left\langle l^{-1}_{\text{MFP}} \right\rangle &= \sum_{n=1}^{\bar{N}}\sum_{l=1}^{\bar{N}} \int \frac{dk'_{n,x}}{\pi/L}\,\frac{m^2}{\hbar^4}\,\frac{2\gamma W}{L\pi}\,\left(1+\frac{\delta_{nl}}{2}\right)\,\frac{\pi}{W} \times \\ &\qquad \frac{\delta(k'_{l,x} \pm \sqrt{2m\varepsilon/\hbar^2 - l^2\pi^2/W^2})}{\sqrt{2m\varepsilon/\hbar^2 - n^2\pi^2/W^2}\,\sqrt{2m\varepsilon/\hbar^2 - l^2\pi^2/W^2}} \\ &= \frac{4m^2\gamma}{\hbar^4\pi k_F}\,\zeta_N^{-1},\end{aligned} \tag{C.4}$$

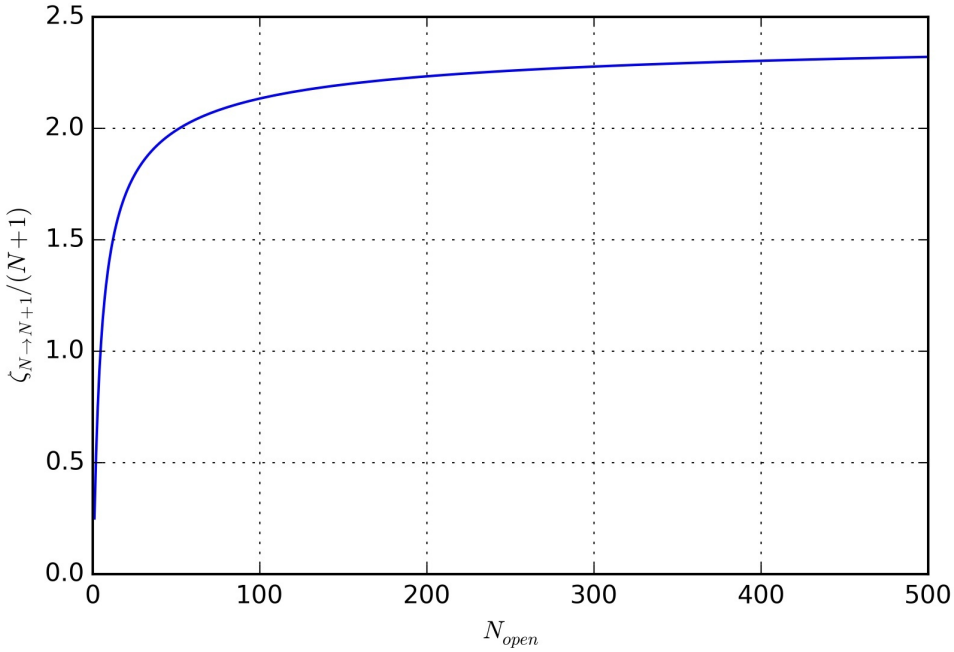

Figure C.1: $\zeta^{-1}_{N\to N+1}/(N+1)$ vs. N.

where $k_F = \sqrt{2m\varepsilon/\hbar^2}$ is the Fermi wavevector,

$$\zeta_N^{-1} = \frac{3\bar{N}}{2}\sum_{n=1}^{\bar{N}}\eta_n^2 + 2\bar{N}\sum_{n=1}^{\bar{N}}\sum_{l>n}^{\bar{N}}\eta_n\,\eta_l, \tag{C.5}$$

and $\eta_n = \left(\frac{W^2k_F^2}{\pi^2} - n^2\right)^{-\frac{1}{2}}$, in agreement with Eq.(8) in the supporting online material of Rieder *et al.* [115]. The value of ζ_N just below the transition $N \to N+1$ (denoted $\zeta_{N\to N+1}$) is plotted in Figure C.1.

We now derive the MFP for a TB dispersion relation given by

$$\varepsilon(k_{x,n}) = 2t\,\left(2 - \cos\left(k_{x,n}a\right) - \cos\left(n\pi a/W\right)\right). \tag{C.6}$$

The number of channels is given by $\bar{N} = \lfloor (W/\pi a)\arccos\left(1-\varepsilon/2t\right)\rfloor$ for $0 < \varepsilon < 4t$ and by $\bar{N} = \lfloor (W/\pi a)\arccos\left(1-(4-\varepsilon/2t)\right)\rfloor$ for $4t < \varepsilon < 8t$. The resulting disorder-averaged inverse MFP reads:

$$\left\langle (l^{\text{TB}}_{\text{MFP}})^{-1}\right\rangle = \frac{\gamma}{\bar{N}Wa^2t^2}\,(\zeta_N^{\text{TB}})^{-1} \tag{C.7}$$

where the dimensionless $(\zeta_N^{\text{TB}})^{-1}$ is given by

$$(\zeta_N^{\text{TB}})^{-1} = \frac{3\bar{N}}{2}\sum_{n=1}^{\bar{N}}(\eta_n^{\text{TB}})^2 +$$

$$2\bar{N}\sum_{n=1}^{\bar{N}}\sum_{l>n}^{\bar{N}}\eta_n^{\text{TB}}\eta_l^{\text{TB}}. \tag{C.8}$$

Here, $\eta_n^{\text{TB}} = |\sin(k_{x,n}\,a)|^{-1}$ and $\sin(k_{x,n})$ is obtained using Eq. (C.6)

Appendix D

NUMERICAL TIGHT-BINDING SIMULATIONS

We start by obtaining the TB form of the RSW BdG Hamiltonian [124] in Eq. (3.1) in the usual way using finite differences (see, for example, Ref.[55],[56],[50],[72]). It reads:

$$\begin{aligned}\mathcal{H}_{\mathrm{BdG}}^{\mathrm{TB}} = & \left[(4t + V(x,y) - \mu(x,y))\ \tau_z + B_{\mathrm{Z}}\,\sigma_z\right. \\ & \left. +\ \Delta(x,y)\,\tau_x\right]\ |x,y\rangle\,\langle x,y| \\ & + \left[-t\,\tau_z - \frac{i}{2}\alpha_{\mathrm{SO}}(x,y)\,\tau_z\,\sigma_y\right]\ |x+a,y\rangle\,\langle x,y| \\ & + \left[-t\,\tau_z + \frac{i}{2}\alpha_{\mathrm{SO}}(x,y)\,\tau_z\,\sigma_x\right]\ |x,y+a\rangle\,\langle x,y| \\ & + \mathrm{h.c.}\end{aligned} \tag{D.1}$$

where $t = \hbar^2/2ma^2$ is the hopping parameter, $V(x,y)$ is the Gaussian random potential, $\mu(x,y)$ is the relevant gate potential, B_{Z} is the Zeeman field, $\Delta(x,y)$ is the *s*-wave superconducting pairing (taken to be real), $\alpha_{\mathrm{SO}}(x,y)$ is the effective Rashba SOC due to proximity effect and a is the lattice constant for the TB lattice. Here, $V(x,y)$, B_{Z}, $\Delta(x,y)$ and $\alpha_{\mathrm{SO}}(x,y)$ are nonzero only within the scattering region. B_{Z}, $\alpha_{\mathrm{SO}}(x,y)$ and $\Delta(x,y)$ are constant within the scattering region except for the values of $\alpha_{\mathrm{SO}}(x,y)$ in the scattering region-lead boundary, where we take it to be half of its value in the bulk.

The experimental values for InSb nanowires quoted in Mourik *et al.* [92] are $\alpha_{\mathrm{SO}} = 0.2\,\mathrm{eV\AA}$, $l_{\mathrm{SO}} \sim 2000\mathrm{\AA}$, $\Delta = 0.25m\mathrm{eV}$, $E_Z/B = 1.5m\mathrm{eV/T}$, $m_* = 0.015m_e$ and $\alpha_{\mathrm{SO}}^2 m_*/2\hbar^2 \sim 0.04m\mathrm{eV}$. We employ these values verbatim, except for l_{SO} (and correspondingly, α_{SO}), for which we use parameters much more accessible experimentally.

We use the Kwant library [130] to obtain the topological phase diagram in our numerical plots. The Kwant library can extract the scattering matrix (*S*-matrix),[72] and therefore the reflection matrix (*r*-matrix) for a given tight-binding system with leads. The topological index Q_{D} can be obtained from the *r*-matrix through $Q_{\mathrm{D}} = \det(r)$ (see Ref. [69]).

The numerical parameters quoted in the caption of Fig. 3.2 correspond to $t = 1.5m\mathrm{eV}$, $a = 40.8\mathrm{nm}$, $l_{\mathrm{SO}} = 4.08\mu\mathrm{m}$ and $\alpha = 6.3 \times 10^{-6}\,c$. Disregarding screening, a Zeeman

Energy of, say, $0.35t$ on the plot would correspond to a magnetic field 0.35T, a value easily accessible by the experiment. In Figures 3.3, E.1, E.3 and E.4 , $l_{\rm SO} = 6.0\mu$m, $t = 0.7m$eV, $a = 60.0n$m and $\alpha = 4.2 \times 10^{-6}\, c$. A Zeeman energy of $0.35t$ corresponds to $B = 0.17\,$T.

The TB form of the effective PW Hamiltonian of Eq. (F.1) used in Appendix F is as follows:

$$\begin{aligned}\mathcal{H}^{\rm TB}_{\rm PW} = & \left[4t + V(x,y) - \mu(x,y)\right]\, \tau_z\, |x,y\rangle\, \langle x,y| \\ & + \left[-t\,\tau_z - \frac{i}{2}\Delta_{\rm eff}(x,y)\,\tau_x\right]\, |x+a,y\rangle\, \langle x,y| \\ & + \left[-t\,\tau_z - \frac{i}{2}\Delta_{\rm eff}(x,y)\,\tau_y\right]\, |x,y+a\rangle\, \langle x,y| \\ & + \text{h.c.}\end{aligned} \tag{D.2}$$

We use numerical values similar to the RSW case in our PW simulations, except to impose $\Delta_{\rm eff} = \Delta\, \alpha_{\rm SO}/\sqrt{B^2 - \Delta^2}$.

Appendix E

TOPOLOGICAL PHASE DIAGRAM OVER THE FULL BANDWIDTH

In this section, we present plots of the topological phase diagram that we obtain analytically from Eq. (3.7) using a TB dispersion relation (see Section 3.2) over the full bandwidth. Although only the low μ regions in our plots correspond to experimentally relevant nanowires, the full bandwidth range would be important for systems that are inherently TB, such as atomic chains [58] or photonic metamaterials [205] simulating topological properties [206]. All analytical plots are produced using Eq. (3.7) (Eq. (F.2) for the PW case), but using a TB dispersion relation for $\epsilon(p)$ in the relevant expressions. All of the numerical results are obtained using a TB simulation utilizing Kwant software, as discussed in the main text.

Figure E.1 depicts the analytically calculated topological phase diagram for an RSW wire as a function of the disorder strength and μ for various magnetic field strengths. The transition between a RSW wire and a pair of oppositely polarized PW wires can be seen as increasing magnetic field polarizes the system. The topological order is less robust against disorder for higher magnetic fields, because the coherence length becomes longer with increasing B. This is the reason why the spin polarized regimes where PW model applies is typically less robust than the lower field regimes where both spin species exist as seen in Fig. E.1(a) and E.1(c) or (d). In order to complete the discussion, we also present an analytical plot (Figure E.2) for an RSW wire for which B is greater than the subband spacing but less than the bandwidth. While this regime is experimentally very hard to achieve, it is useful for comparing the PW and the RSW regimes. The vertical blue line denotes the bottom of the higher energy spin band beyond which both spin species exist. We note that the critical disorder strength increases with the chemical potential, hence spin-polarized regime, which appear at lower chemical potential values, is less robust against disorder.

In Figure E.3, the analytically calculated phase diagram of a wire with $W = 4a$ is plotted with increasing disorder. We see that the phase diagram gets fragmented as number of channels are increased. We also note that for a given amount of disorder, there is a

maximum Zeeman field B_{max} above which no topological order is present. The reason is that in our numerical TB simulations, the localization length is not a monotonous function of energy. It grows (with increasing energy) until the middle of the band, and after that it decreases as the energy comes closer to the band edge. This places an upper magnetic field limit to topological regions since the superconducting coherence length monotonically increases with B. For a pure quadratic dispersion, the upper limit is given by the limitations of the approximations of Fermi's Golden Rule and would increase indefinitely with increasing energy as discussed in the main text. We note that the upper limit discussed here has a different origin than that discussed by Ref.[155] for finite-length wires.

We finally present the full TB bandwidth version of Fig. 3.2, with slightly different material properties, here in Fig. E.4. This figure is the numerical simulation result that matches the last of the analytical plots in Fig. E.3. The relevant numerical values are given in each of the Figures' captions.

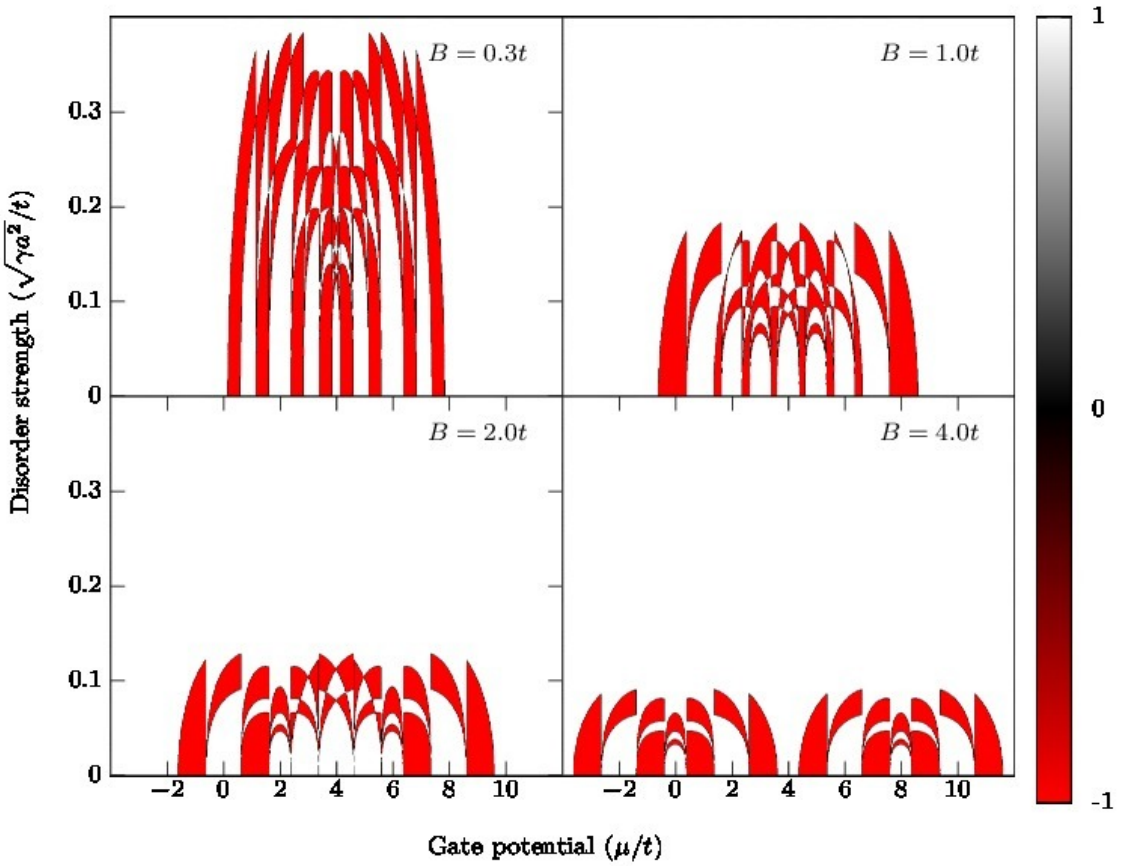

Figure E.1: Q_{D} as a function of $V_0 = \sqrt{\gamma/a^2}$ and μ for a multichanneled RSW wire for different values of B, obtained analytically using Eq. (3.7). (a), (b) Low magnetic field $B \gtrsim \Delta$ limit requires a full RSW model and topological order can survive up to high disorder strengths. (c), (d) The spin-polarized system can be described by a PW model and topological order is completely destroyed with less disorder. Here, $W = 4a$, $\alpha_{\mathrm{SO}} = 0.015\hbar/ma$ and $\Delta = 0.20t$ where $t = \hbar^2/2ma^2$ and a is the tight-binding lattice spacing. See Appendix D for a discussion of corresponding experimental parameters.

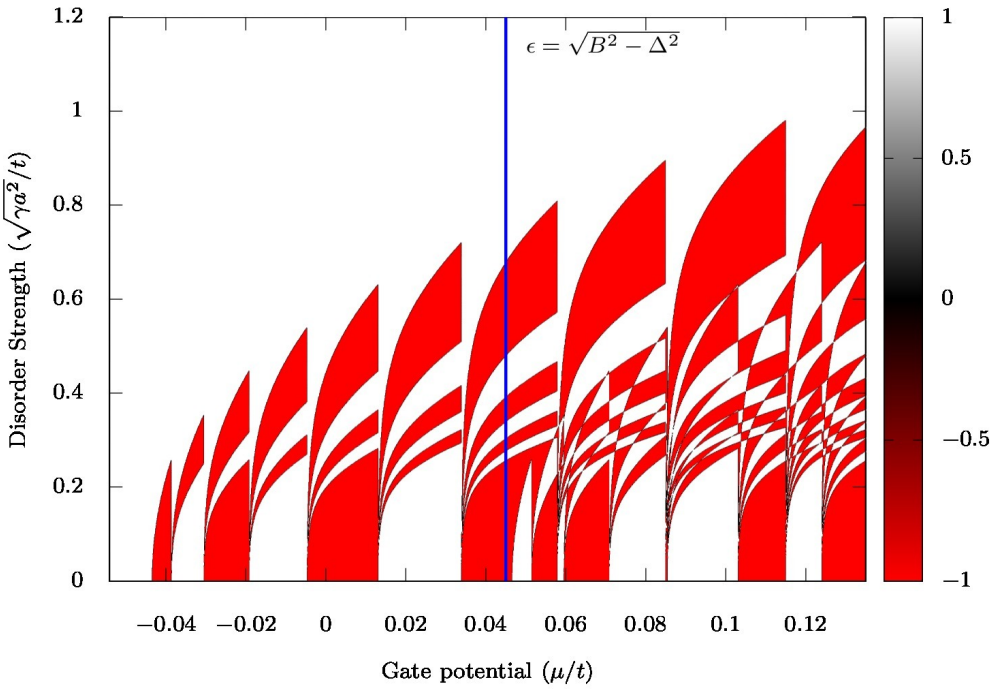

Figure E.2: Q_{D} as a function of $V_0 = \sqrt{\gamma/a^2}$ and μ for a multichanneled wide RSW wire, obtained analytically using Eq. (3.7), with $W = 77a$. Here, $\alpha_{\mathrm{SO}} = 0.015\hbar/ma$ ($l_{\mathrm{SO}} = 100a$), $\Delta = 0.20t$ and $B = 0.205t$ with the hopping parameter $t = \hbar^2/2ma^2 = 0.7$ meV and the lattice spacing $a = 60$ nm. The blue vertical line at $\mu = \epsilon = \sqrt{B^2 - \Delta^2}$ is the bottom of the second spin band.

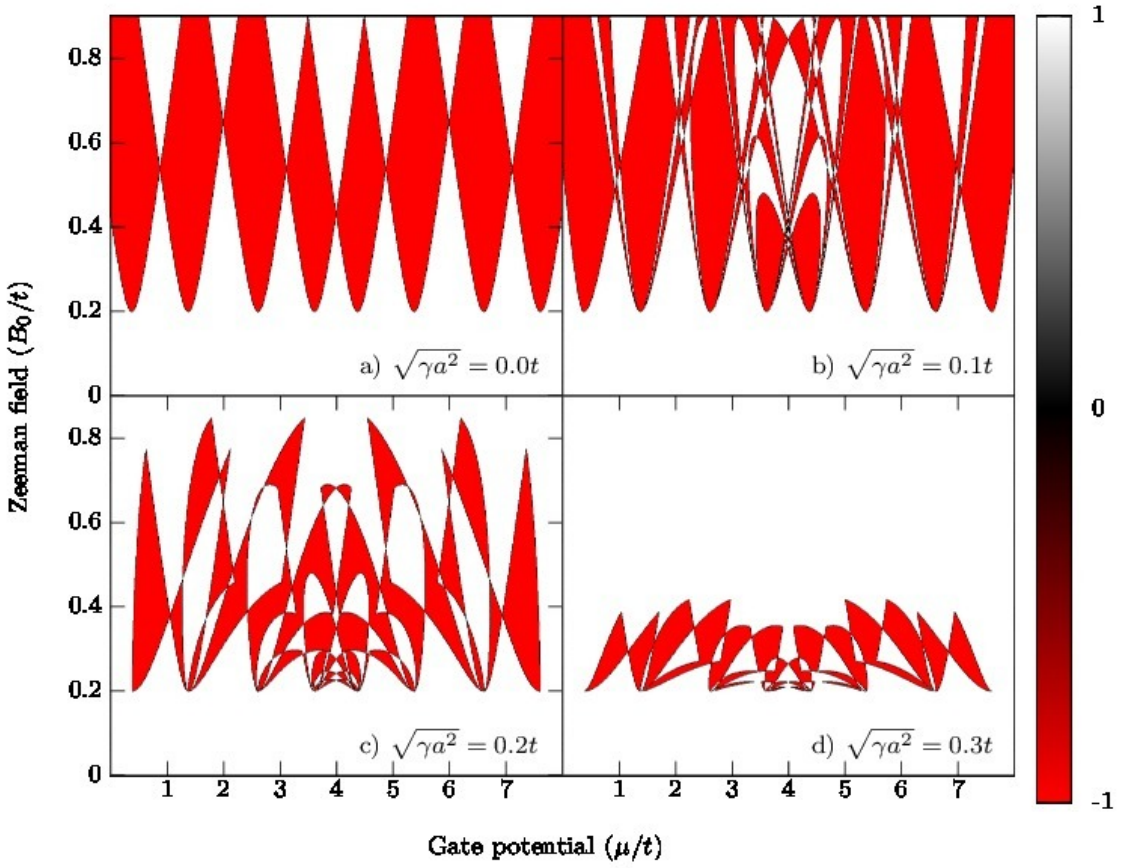

Figure E.3: Q_{D} as a function of B and μ for varying disorder strengths for an RSW TS with Gaussian disorder, analytically calculated using Eq. (3.7) for a four-channel TB system. Subfigure (c) matches the numerical data shown in Fig. E.4. The parameters used are $\alpha_{\mathrm{SO}} = 0.015\hbar/ma$ and $\Delta = 0.2t$, where $t = \hbar^2/2ma^2$ and a is the lattice spacing. See Appendix D for a discussion of corresponding experimental parameters.

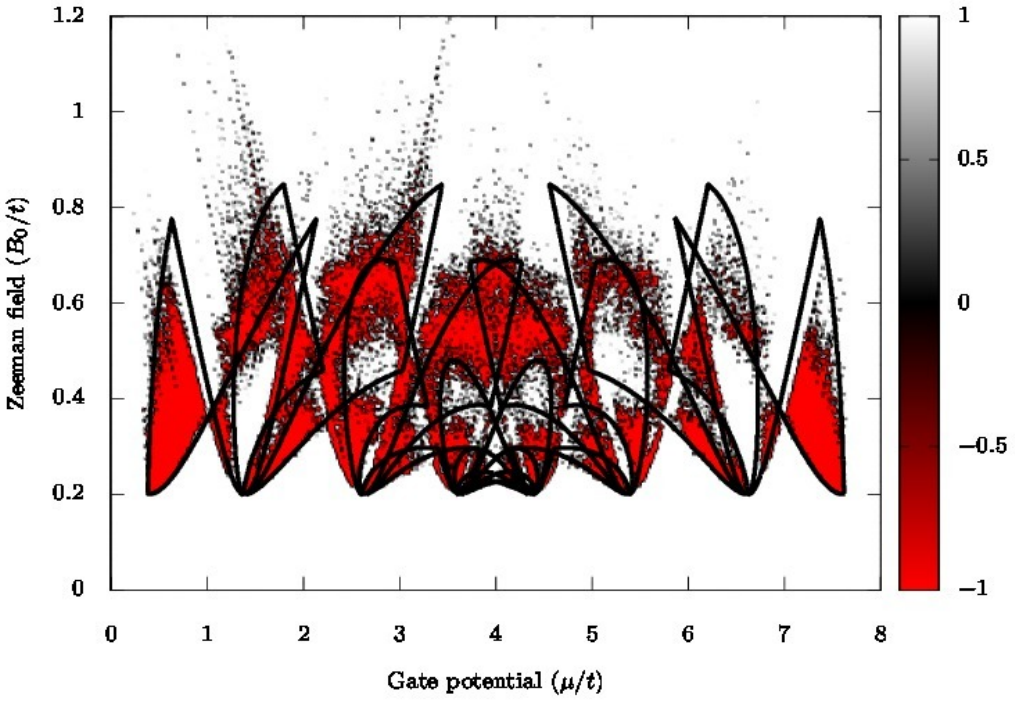

Figure E.4: Q_{D} as a function of B and μ for a four-channel system (compare with Figs. 3.2 and E.3). The black lines, which represent topological boundaries, are obtained analytically using Eq. (3.7). The background red-white colors are obtained using tight-binding numerical simulations. The parameters are $V_0 = 0.2t$, $\Delta = 0.2t$ and $\alpha_{\mathrm{SO}} = 0.015\hbar/ma$. See Appendix D for a discussion of corresponding experimental parameters.

Appendix F

TOPOLOGICAL PHASE DIAGRAM FOR MULTICHANNEL EFFECTIVE *P*-WAVE NANOWIRES WITH DISORDER

In this Appendix section, we present the effects of disorder on PW wires, which is a system previously studied in literature [69, 73, 105–107, 109–111, 113–115, 119, 125], for completeness and for comparison with the results of our paper for disordered multichannel RSW nanowires. We start with the Hamiltonian in Eq. (F.1) and present the topological charge in Eq. (F.2). We plot the topological phase diagram for a PW wire as a function of μ and disorder strength for a fixed B_{Zeeman} (Fig. F.1) and compare this plot with its analogue for RSW wires (Fig. 3.3).

The BdG Hamiltonian for an effective *p*-wave wire with spatially homogeneous effective SOC strength is

$$\mathcal{H}_{\text{BdG}}^{\text{PW}} = \varepsilon(p)\,\tau_z + \Delta_{\text{eff}}\,\mathbf{p}\cdot\tau. \tag{F.1}$$

Note that Δ_{eff} has units of velocity while Δ in Eq. (3.1) has units of energy. This effective SOC strength is related to the corresponding RSW superconducting gap by $\Delta_{\text{eff}} = \Delta\,\alpha_{\text{SO}}/\sqrt{B^2-\Delta^2}$ [55]. We consider a Gaussian disorder of the form $\langle V(\mathbf{r})\,V(\mathbf{r}')\rangle = \gamma\,\delta(\mathbf{r}-\mathbf{r}')$ for $\mathbf{r},\mathbf{r}'$ in the wire, with γ as the disorder strength and $\langle V(\mathbf{r})\rangle = 0$. This Hamiltonian is useful for comparison with the fully polarized limit of the RSW case.

The Hamiltonian in Eq. (F.1) is in Altland-Zirnbauer (AZ) symmetry class D in two dimensions [67] with a $\mathbb{Z}_2$ topological number. This Hamiltonian also possesses a chiral symmetry, broken by the $\Delta_{\text{eff}}\,p_y\tau_y$ term. If this term is set to zero, the Hamiltonian is also in class BDI [115, 125–127] having a $\mathbb{Z}$ topological number. (1D wires trivially satisfy this condition.) In the thin wire limit, i.e. $\Delta_{\text{eff}} \ll \hbar/mW$, the chiral symmetry breaking term is $\mathcal{O}\left((m\Delta_{\text{eff}}W/\hbar)^2\right)$. The wire in class BDI can have an integer number of Majorana fermions at its ends. The chiral symmetry breaking term pairwise hybridizes these solutions. Hence the chiral topological number $Q_{\text{BDI}} \in \mathbb{Z}$ and the class-D topological number $Q_{\text{D}} \in \mathbb{Z}_2$ are related as $Q_{\text{D}} = -1^{Q_{\text{BDI}}}$ [69].

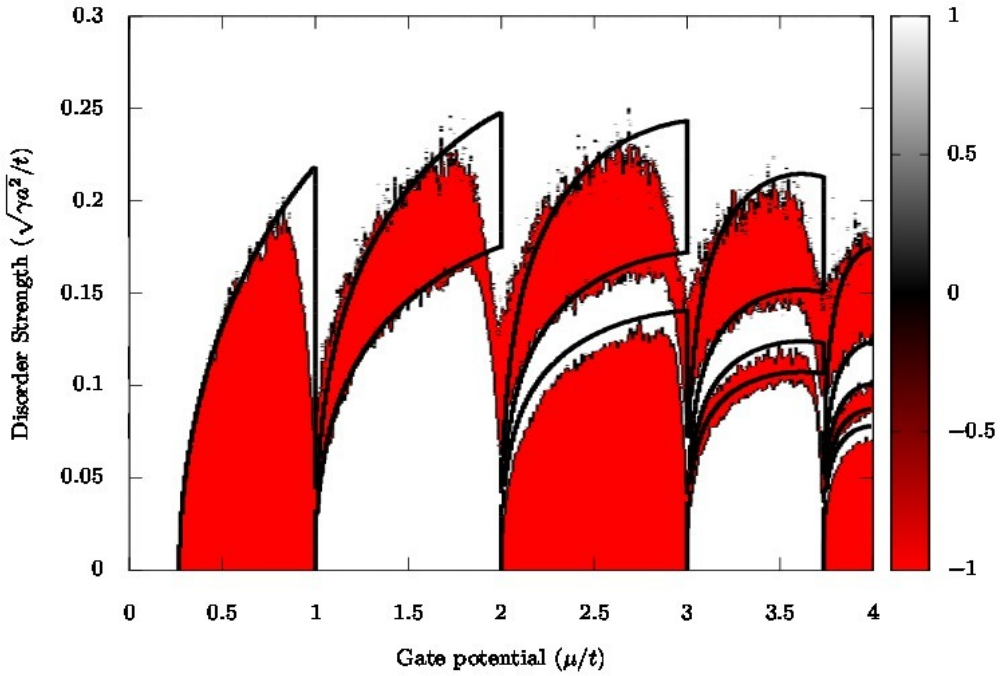

Figure F.1: Q as a function of $\sqrt{\gamma/a^2}$ and μ for a multichanneled PW wire with dimensions $W = 4a$ and $L = 60000a$ (L used only in the numerical tight-binding code) and with $\alpha_{\rm SO} = 0.01\hbar/ma$, where a is the tight-binding lattice spacing. The red-white colors in the background are obtained numerically with a tight-binding method whereas the black solid lines are obtained using Eq. (F.2) with Eq. (3.10).

In order to solve the Schrödinger equation $H\,\Psi = E\,\Psi$ at $E = 0$ to obtain the Lyapunov exponents, we follow Adagideli *et al.* [73] to off-diagonalize the Hamiltonian and apply an imaginary gauge transformation. This allows us to re-express Q_{BDI} in terms of Λ_n: [115]

$$Q_{\text{BDI}} = \sum_{n=1}^{\bar{N}} \Theta\left(\xi - \frac{1}{\Lambda_n}\right), \tag{F.2}$$

where $\bar{N} = \lfloor W/\pi\sqrt{2m\mu/\hbar^2} \rfloor$ and $\lfloor x \rfloor$ is the usual floor function. We obtain Λ_n again using Eq. (3.8). We obtain l_{MFP}^{-1} using Fermi's Golden Rule (see Appendix C) first for a quadratic dispersion relation and then for a TB dispersion relation.

We compare the results found using Eq. F.2 with those obtained by numerical simulations in Figure F.1 and find an excellent fit over the whole TB bandwidth. In a clean PW wire ($\sqrt{\gamma/a^2} = 0$), Majorana modes appear if $\bar{N}$ is odd and Majorana states fuse to form ordinary Dirac fermions if $\bar{N}$ is even. This behavior survives up to a finite disorder strength (see Fig. F.1). As in the case of RSW wires, further increase of the disorder strength gives a series of transitions between non-trivial and trivial topological phases as each Λ_n increases and crosses ξ^{-1}. While both multichanneled RSW and PW wires feature reentrant behavior, we see that there are additional transitions for the RSW wires leading to a richer phase diagram (compare Figures F.1 and 3.3), in agreement with our analytical results presented in Eq. (3.11).

Appendix G

WORK AND POWER EXTRACTED FROM THE INFORMATION ENGINE

In this appendix, we calculate the power and work extracted from the system in the short edge limit. The power extracted under bias is given by

$$\begin{aligned} P(t) &= \frac{eV}{h}\Big[eV(1-\frac{\zeta}{2}) + \zeta m(t)\hbar\Gamma_T\Big], \\ &= \frac{eV}{h}\Big[eV(1-\frac{\zeta}{2}) + \zeta(m_0-\bar{m})\mathrm{e}^{-t/\tau_m}\hbar\Gamma_T + \zeta\bar{m}\hbar\Gamma_T\Big]. \end{aligned} \tag{G.1}$$

Rearranging the above equation and substituting $\bar{m}\hbar\Gamma_T = \frac{eV}{2}$, we obtain

$$P(t) = \frac{eV}{h}\Big[eV + \zeta(m_0-\bar{m})\mathrm{e}^{-t/\tau_m}\hbar\Gamma_T\Big]. \tag{G.2}$$

Charging cycle: We would like to find the heat dissipated while we charge the device. Starting from totally unpolarized nuclear spins ($m_0 = 0$) and using Eqn. (G.2), we get:

$$\begin{aligned} P(t) &= \frac{eV_C}{h}\Big[eV_C - \zeta\bar{m}\mathrm{e}^{-t/\tau_m}\hbar\Gamma_T\Big], \\ &= \frac{eV_C}{h}\Big[eV_C - eV_C\frac{\zeta}{2}\mathrm{e}^{-t/\tau_m}\Big]. \end{aligned} \tag{G.3}$$

As seen in Eq. (5.7), one has to wait infinitely long amount of time to reach the target mean polarization. Instead, we charge the device up to a fraction of full polarization $m = \frac{\kappa}{2}$ where κ is a value we later choose to maximize power or efficiency depending on the application. We then calculate the amount of time, $\bar{t}$, to reach the specified target mean polarization using $\frac{\kappa}{2} = \bar{m}(1-e^{-\bar{t}/\tau_m})$ and obtain:

$$\bar{t} = -\tau_m \ln\Big(1 - \frac{\kappa}{2\bar{m}}\Big). \tag{G.4}$$

We then get the heat dissipated by integrating the power up to $\bar{t}$:

$$W_C(V_C) = \int_0^{\bar{t}} \frac{eV_C}{h}\Big[eV_C - \frac{\zeta}{2}\mathrm{e}^{-t/\tau_m}eV\Big],$$

$$= \frac{e^2V_C^2}{h}\tau_m\Big[-\ln(1-\frac{\kappa}{2\bar{m}}) - \frac{\zeta}{2}\frac{\kappa}{2\bar{m}}\Big],$$
$$= \frac{eV_C}{2\pi\gamma_0}\tanh\big(\frac{eV_C}{2k_BT}\big)\Big[\ln\Big(\frac{2\bar{m}}{2\bar{m}-\kappa}\Big) - \frac{\zeta}{2}\frac{\kappa}{2\bar{m}}\Big]. \tag{G.5}$$

Note that $0 \leq 1-\kappa/2\bar{m} < 1$, and this condition gives us an lower bound on the voltage applied as:

$$V_C \geq \frac{k_BT}{e}\ln\left(\frac{1+\kappa}{1-\kappa}\right). \tag{G.6}$$

Discharging cycle: As a next step in the cycle, we apply a reverse bias, $V_D < 0$, and we would like to find the time t^* at which $P(t)$ changes sign, i.e. $P(t^*) = 0$. Using Eqn. (G.2), we obtain:

$$-|eV_D| = \zeta\hbar\Gamma_T(\bar{m}-m_0)\mathrm{e}^{-t^*/\tau_m},$$
$$|eV_D| = \zeta\mathrm{e}^{-t^*/\tau_m}\big(\frac{|eV_D|}{2} + m_0|eV|\coth\big(\frac{eV_D}{2k_BT}\big)\big),$$
$$t^* = \tau_m\ln\Big[\zeta\Big(\frac{1}{2}+m_0\coth\big(\frac{eV_D}{2k_BT}\big)\Big)\Big] \tag{G.7}$$

We then integrate the power up to $t = t^*$ to obtain the work done at fixed voltage:

$$W_D(V_D) = \int_0^{t^*}\frac{|eV_D|}{h}\Big[|eV_D| - \zeta(m_0-\bar{m})\mathrm{e}^{-t/\tau_m}\hbar\Gamma_T\Big],$$
$$= \frac{e^2V_D^2}{h}t + \frac{|eV_D|}{h}\tau_m\zeta(m_0-\bar{m})\hbar\Gamma_T\mathrm{e}^{-t/\tau_m}\Big|_0^{t^*},$$
$$= \frac{e^2V_D^2}{h}t^* + \frac{|eV_D|}{h}\tau_m\zeta(m_0-\bar{m})\hbar\Gamma_T(\mathrm{e}^{-t^*/\tau_m}-1). \tag{G.8}$$

Inserting t^* into the equation above and and using the relation $\bar{m}\hbar\Gamma_T = -\frac{|eV_D|}{2}$, we get:

$$W_D(V_D) = \frac{e^2V_D^2}{h}\tau_m\Big[\ln\Big(\zeta\Big(\frac{1}{2}+m_0\coth\big(\frac{|eV_D|}{2k_BT}\big)\Big)\Big)$$
$$+1-\zeta\Big(\frac{1}{2}+m_0\coth\big(\frac{|eV_D|}{2k_BT}\big)\Big)\Big]. \tag{G.9}$$

We finally take the polarization reached at the end of the charging cycle, $m_0 = \frac{\kappa}{2}$, as the initial polarization for discharging to finally obtain

$$W_D(V_D) = \frac{|eV_D|}{2\pi\gamma_0}\tanh\big(\frac{|eV_D|}{2k_BT}\big)\Big[\ln\Big(\frac{\zeta}{2}\Big(1+\kappa\coth\big(\frac{|eV_D|}{2k_BT}\big)\Big)\Big)$$
$$+1-\frac{\zeta}{2}\Big(1+\kappa\coth\big(\frac{|eV_D|}{2k_BT}\big)\Big)\Big]. \tag{G.10}$$

In order to extract work from the nuclear spin polarization, one has to make sure that $t^* > 0$, which gives us an upper bound on the applied voltage as:

$$|V_D| \leq \frac{k_B T}{e} \ln\left(\frac{2-\zeta(1-\kappa)}{2-\zeta(1+\kappa)}\right). \tag{G.11}$$

Appendix H

BULK AND STRUCTURAL INVERSION ASYMMETRY TERMS IN THE BERNEVIG-HUGHES-ZHANG HAMILTONIAN

In this Appendix, we present the bulk inversion asymmetry (BIA) and the structural inversion asymmetry (SIA) terms in the BHZ Hamiltonian for completeness. The BIA term, due to having two different atoms forming the zinc blende structure, is of the form [189]

$$H_{\text{BIA}} = \begin{pmatrix} 0 & 0 & \Delta_e k_+ & -\Delta_z \\ 0 & 0 & \Delta_z & \Delta_h k_- \\ \Delta_e k_- & \Delta_z & 0 & 0 \\ -\Delta_z & \Delta_h k_+ & 0 & 0 \end{pmatrix}. \tag{H.1}$$

The SIA term, arising from an applied electric field, creates Rashba-like SOI terms. These terms must be linear for the electron states and cubic for the hole states to lowest order and we ignore the cubic states. The resulting addition to the Hamiltonian is [207]

$$H_{\text{SIA}} = \begin{pmatrix} 0 & 0 & i\xi_e k_- & 0 \\ 0 & 0 & 0 & 0 \\ -i\xi_e^* k_+ & 0 & 0 & 0 \\ 0 & 0 & 0 & 0 \end{pmatrix}. \tag{H.2}$$